High Pressure Synthesis and Characterisation of Layered Carbon Nitride Materials

A thesis presented to the University College London in partial fulfilment of the requirements for the degree of Doctor of Philosophy

Victoria Jane Lees

University College London

July 2009

I, Victoria Lees, confirm that the work presented in this thesis is my own. Where information has been derived from other sources, I confirm that this has been indicated in the thesis.

Abstract

The research undertaken in this project has involved the synthesis of the carbon nitride material $C_6N_9H_3$.HCl under high pressures and temperatures in the piston cylinder apparatus. The synthesis conditions of the material have been perfected and the relatively well crystallised products have been characterised in several ways to try to gain a better understanding of the structure of the material. Characterisation techniques used include; elemental analysis, X-ray diffraction, infrared spectroscopy, scanning and transmission electron microscopy, X-ray photoelectron spectroscopy, visible, ultraviolet and Fourier Transform Raman spectroscopy.

The behaviour of the $C_6N_9H_3$.HCl material has also been studied further under very high pressures. Diamond anvil cell techniques and synchrotron X-ray radiation have been used to investigate the materials structural behaviour up to pressures in excess of 60 GPa. The decompression of the material has also been investigated. Investigation of the behaviour at high pressures using FTIR was also attempted.

The ambient pressure characterisation, high pressure behaviour and decompression of the material have been compared in detail to computational calculations performed on the model structure proposed for the material. Interesting advances in the understanding of the ambient pressure structure and of the high pressure behaviour of the material have been made and the significant structural changes in the material at very high pressures have been explained by the comparison of the experimental and computational results.

Due to the highly fluorescent nature of the material under visible Raman lasers it was not possible to obtain Raman spectra of the material in the laboratory at UCL. Therefore the material has been studied using UV and FT Raman techniques using equipment in laboratories in Lyon and Grenoble in France and in Nottingham, UK, in an attempt to obtain vibrational spectra without exciting electronic transitions and to gain more information about the structure.

Table of Contents

Table of Figures

Table of Tables

Table of Abbreviations

µm – micrometers.

Å – Angstroms.

ADXRD – Angle dispersive X-ray diffraction.

BN – boron nitride.

˚C – Degrees centigrade.

CRMHT - Conditions Extrêmes et Matériaux : Haute Température et Irradiation.

cm – centimetres.

cm^{-1} – Relative centimetres.

CNRS - Centre national de la recherche scientifique.

C/N – carbon nitride.

CVD – Chemical vapour deposition.

DAC – Diamond anvil cell.

DFT – Density functional theory.

EDX – Energy dispersive X-ray spectroscopy.

EDXRD – Energy dispersive X-ray diffraction.

EELS – Electron energy loss spectroscopy.

EMP – Electron microprobe

ENS – Ecole Normale Superieure

ESRF – European synchrotron radiation facility.

eV – Electron volt.

FT – Fourier transform.

FTIR – Fourier transform infra red.

g – gram.

GPa – Gigapascal.

HCl – Hydrogen Chloride.

HOMO – Highest occupied molecular orbital.

HP – High pressure.

HR-TEM – High resolution - tunnelling electron microscopy.

HT – High temperature.

kb – Kilobars

keV – Kiloelectron volt.

LDA – Local density approximation.

LEMPI - Laboratoire d'Electrochimie et de Physicochimie des Matériaux et des Interfaces.

LUMO – Lowest unoccupied molecular orbital.

MA – Multi anvil.

MeV – Megaelectron volt.

Mg – Milligrams.

mm – Millimetres.

mol - Moles

MPa – Megapascal.

NBS – National bureau of standards.

Nd:YAG – Neodymium doped yttrium aluminium garnet

nm – Nanometres.

NMR – Nuclear magnetic resonance.

P – Pressure.

PC – Piston cylinder.

PEELS – Parallel energy loss spectroscopy.

ppm – Parts per million.

PVD – Physical vapour deposition.

RF – Radio frequency.

SEM – Scanning electron microscopy.

SRS – Synchrotron radiation source.

TEM – Tunnelling electron microscopy.

UCL – University College London.

UK – United Kingdom.

USA – United States of America.

UV – Ultra violet.

XPS – X-ray photoelectron spectroscopy.

XRD – X-ray diffraction.

Acknowledgements

The work that went into this thesis would not have been possible without the opportunity presented to me in the very beginning by Professor Paul F. McMillan, so therefore first of all I want to thank him for this and all the help and support he has provided over the course of my PhD. I would also like to thank the University College London Department of Chemistry their studentship which funded this work.

I am also very grateful for the help I have received from many other people during the course of this work. Dr. Andrea Sella for being my secondary supervisor and the help with so many things, too many to mention.

I would like to express my enormous appreciation to Dr. Edward Bailey at UCL for teaching me everything I know about Piston Cylinder and Multi Anvil apparatus, plus a whole lot more besides. A pleasure to work (and live!) with I couldn't have wished for a more helpful colleague, teacher and friend.

Dr Eric Qurico of the Université Joseph Fourier Laboratoire de Planétologie at the CNRS in Grenoble, France, who helped extensively with the UV Raman work enabling me to use equipment in several labs across France and gain the results presented here. Also to Gilles Montagnac of the Laboritore de Sciences de la Terre, ENS, Lyon, France, for the use of the UV Raman spectrometers in his lab.

I am also grateful to Partick Simon from the Centre de Recherche sur les Matériaux á Haute Température at the CNRS in Orléans, France for the repeated access he provided me to the FT-Raman spectrometer in their lab.

The members of Paul McMillan's research group at UCL have been an invaluable source of knowledge, help and support and I want to thank them all for being wonderful colleagues and friends. Especially Dr. Raúl Quesada and Dr. Dominik Daisenberger, who taught me everything I know about diamond anvil cells and the inner workings of the lab. My thanks also go out to Ashkan Salamat, Rachael Hazael, Katherine Woodhead and all the guys in room 320 for making such a great working environment. My special thanks go to Dr. Sobia

Ashraf, because without the regular visits from ‘my friend in the lab next door’, I certainly would have gone slightly more insane during this PhD.

Without the support of my family and friends none of this would have been possible. My eternal love and gratitude go out to my parents and sister for their never ending support and endurance. They say you can’t choose your family, and I’m glad I never had to as I couldn’t have gotten it so right on my own.

Fortunately you can choose your friends, and I’ve had the good luck to be graced with some of the best ones in the world, most notably all the many and varied members of the University of London Sub-Aqua Club who have provided me with more than enough help, hindrance and distraction to see that the time I’ve been working on this thesis has truly flown by. A few I must mention by name; Nathan Long, Mairead Conneely, Jeremy Davey and Steve Salvatore who were always there for me, even when I didn’t know I needed it.

And last, but by no means least, Mr. Lea Room, thank you for giving me the proverbial kick that was necessary.... you turned up just in time or this may never have been over with.

Chapter One - Introduction

1.1 Background

Solid state carbon nitride materials were first described almost two centuries ago. An amorphous, hydrogen containing material was reported by Berzelius, and then given the name 'melon' by Liebig in 1834[1]. It was assigned the empirical formula $C_6N_9H_3$ although it was not possible to ascertain the exact composition at the time and several models for the structure have since been postulated.

These kinds of molecular carbon nitride compounds and solid state materials related to them have some important applications within materials science. They are used in the synthesis of high strength refractory plastics including the well known melamine formaldehyde series that have been known since the early days of carbon nitride chemistry. These materials are commonly incorporated into polymers that provide flame and heat retardation[2] due to the tendency to only release nitrogen gas when burned or charred. They are also useful materials in the sense that they have high energy density and are used in the production of advanced fuels and explosives[3,4].

Nanomaterials have been synthesised from these types of condensed carbon nitride heterocyclic systems and some have been seen to exhibit potentially useful fluorescence and optoelectronic properties[5]. Recently graphitic carbon nitride materials have been proposed as a basis for a new family of water splitting photo catalysts that can produce hydrogen from water upon visible light irradiation[6]. Carbon nitride is a particularly useful material for this

process since it is very chemically and thermodynamically stable and does not rely on a complicated process for its manufacture.

It was shown first by the high pressure group in Bordeaux[7] and then in Arizona[8] that relatively well-crystallised graphitic carbon nitride materials could be obtained by treating heterocyclic aromatic precursors such as melamine and cyanuric chloride under conditions of high pressure (P = 1-5 GPa) and temperatures between 400-500 ^{o}C[8]. In this thesis high pressure-high temperature methods were used to synthesise layered graphitic carbon nitride materials from the reaction between melamine and cyanuric chloride at P = ~1.5 GPa and T = 550 ^{o}C. These synthesis experiments were carried out using the piston cylinder apparatus in the high pressure laboratory at UCL. The materials were characterised using X-ray powder diffraction and FTIR spectroscopy. Successful experiments to obtain the first Raman spectroscopy data for these highly luminescent materials using a combination of UV Raman (resonance Raman) and Fourier transform (FT-) Raman using near-IR (1064 nm) laser excitation were also performed. Results of *ab initio* theoretical calculations carried out in a parallel study by PhD student Malek Deifallah working with Dr. Furio Cora permitted a new interpretation of the structure and analysis of the X-ray diffraction data.

The layered carbon nitride materials are also of interest for planetary geology in that they are thought to constitute the "tholins" produced by reactions between CH_4 and NH_3 in the upper atmosphere of Titan and are responsible for the characteristic reddish haze of that satellite. Titan is thought to be one of the planetary bodies in the solar system that could possibly support life forms and so its atmospheric chemistry has received considerable attention especially since

the Cassini-Huygens missions that returned valuable new data on the spectroscopic characteristics of atmospheric species. During the thesis work our group entered into contact with Dr. Eric Quirico from the Laboratory of Planetology within the Institute of Physics at University Joseph Fourier, Grenoble, who was leading a programme to study and test laboratory-produced carbon nitride species as models for Titan's tholins. The materials synthesised in our study provided important constraints on the spectroscopic interpretation of the tholin samples[9].

The development of solid state carbon nitride materials has also been subject to considerable interest in recent years due to predictions by Cohen et. al. in the early 1980s of the possible existence of an sp^3 bonded form of carbon nitride material that could provide a new class of super-hard materials competitive in hardness with diamond. Intensive research including various attempts to synthesise the new materials by high pressure-high temperature methods have been carried out during the past twenty years, but no definitive reports of their successful synthesis and characterisation have been recorded. In our work we investigated the high pressure treatment of graphitic carbon nitride to study the densification of the layered structure. Here the theoretical calculations combined with *in situ* synchrotron X-ray diffraction data obtained at high pressure in the diamond anvil cell gave new insights into the unusual structural changes and densification mechanisms that could occur within the layered structures to lead to sp^3-bonded structures.

1.2 Melon, Melem and Graphitic Carbon Nitride

The characterisation of a nanocrystalline form of Liebig's 'melon'[1] has only recently been achieved.[10] Electron diffraction, solid state NMR spectroscopy and theoretical calculations were employed by a German group to characterise the material and show that it has the formula $[C_6N_7(NH_2)(NH)]_n$ (Figure 1).

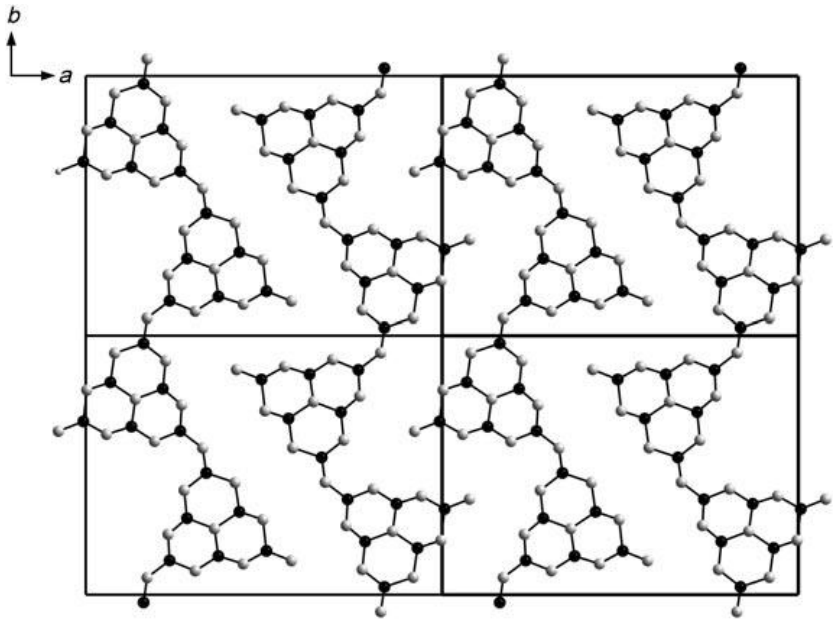

Figure 1. Projection of the structure of melon. H atoms are omitted for clarity. C = black and N = gray[10], note the similarity of the material to that of the proposed structure for graphitic carbon nitride as outlined above.

The melon material is made up of infinite 1D chains of NH-bridged 'melem'[11], monomers ($C_3N_{10}H_6$ or $C_6N_7(NH_2)_3$) which comes from a family of related carbon nitride materials now known to exist. These materials have structures based on oligomeric planar units formed by the condensation of triazine, C_3N_3, rings which is the core component of well known heterocyclic materials such as

melamine, (2,4,6-triamine-1,3,5-triazine: $C_3N_6H_6$ or $C_3N_3(NH_2)_3$) or triazine itself ($C_3N_3H_3$) [10-15] (Figure 2).

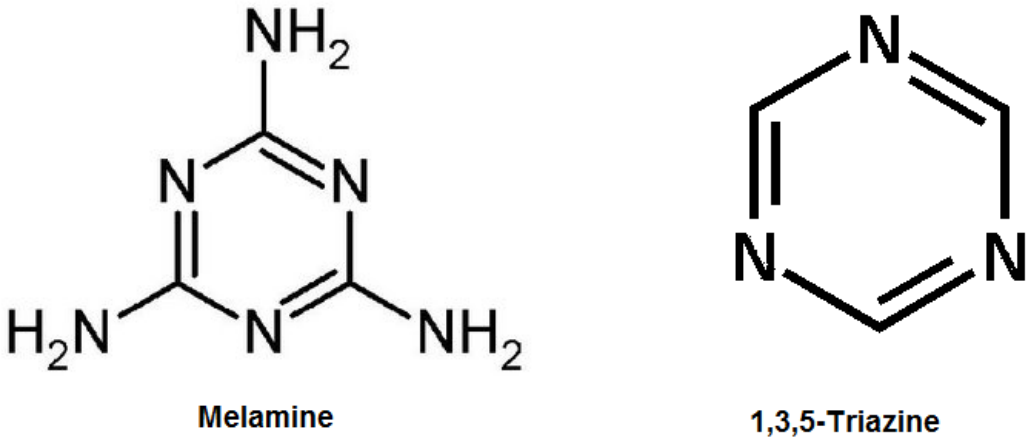

Figure 2. Structural representations of melamine and 1,3,5-triazine.

1.3 Super-hard sp^3-bonded Carbon Nitrides: Predictions vs. Synthesis Attempts

For many years now there has been great interest in developing solid state carbon nitride materials, this stems from predictions that have been made about the possible interesting mechanical and electronic properties that certain carbon nitride based materials could posses. The initial interest in carbon nitride systems took off in the mid 1980s, when it was first suggested by Cohen et. al. that according to an empirical scaling law[16], if a tetrahedral compound made up of carbon and nitrogen could be found with an analogous structure to β-silicon nitride, i.e. β-C_3N_4 it could be less compressible and possibly harder than diamond. This suggestion was later supported by further theoretical calculations[17].

The strength and compressibility of bonds determines the ability of a solid to resist deformation and covalent materials tend to have the highest bulk moduli. Diamond has the highest bulk moduli at 4.43 Mbar and it is also the hardest solid known. The extremely high hardness of diamond is due to the sp^3 carbon network with short, strong C-C bonds. The requirements for a large bulk modulus are a low ionicity and short bond length.

It was suggested that, according to this model, a covalent solid composed of carbon and nitrogen may have a larger bulk modulus than diamond[16]. A proposed possible structure for this material was a solid based on the structure of β-Si_3N_4 i.e. β-C_3N_4. It is now thought unlikely that β-C_3N_4 is the lowest energy structure for the C-N system. However theoretical calculations that were performed[17] by Liu and Cohen showed that there is a good chance that β-C_3N_4 could be at least a meta-stable structure. The same work also put forward the suggestion that it may be possible to synthesise such a material using some kind of amorphous carbon nitride system and that under high pressure and high temperature conditions a phase transition may be induced similar to the one observed for pure carbon when graphite is converted to diamond.

Subsequently additional hard forms and also a graphitic form of carbon nitride were predicted by Teter and Hemley[18] on the basis of first principles calculations. By considering chemical systems that contained carbon in a four coordinated environment with nitrogen and nitrogen three coordinated with carbon several other prototype carbon nitride structures were identified. These forms were; g-C_3N_4, a two dimensional structure derived from graphite with carbon vacancies. The α and β forms are analogous to the corresponding Si_3N_4 structures. The 'pseudo-cubic' form, bl-C_3N_4 derives from the zinc blende

structure and also contains carbon vacancies. Also predicted was the cubic structure, c-C_3N_4. These possible forms are illustrated below (Figure 3).

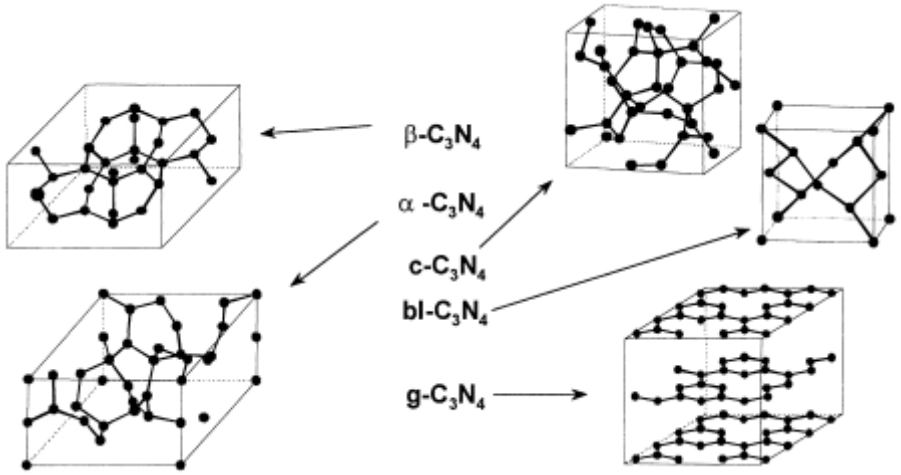

Figure 3. The different possible structures proposed for C_3N_4 predicted by Teter and Hemley[18].

The hard forms, α, β, cubic and pseudo cubic are all based on a continuous 3/4-connected network of alternating four-fold tetraherally coordinated carbon and three fold trigonally coordinated nitrogen. Since these forms of carbon nitride were postulated there have been many and varied attempts to prepare these types of materials. However, to date a reliable characterisation of a bulk C_3N_4 phase with the super hard qualities predicted still remains elusive[19-21].

The graphitic form is composed of stacked layers made up of a planar network of alternating carbon and nitrogen atoms in triazine like rings connected by bridging imido groups. The calculations reveal that the graphitic form is likely to be more stable than any of the hard forms of C_3N_4. Other work has been documented that investigates the synthesis of layered graphitic carbon nitride materials which could prove to be potential precursors to a high-density sp^3-bonded form of carbon nitride. These graphitic materials may have potential useful properties themselves and they are being studied extensively both

experimentally and theoretically[5,7,8.12,13,18,22-26] . This study is concerned with the synthesis and characterisation of graphitic carbon nitride and investigation of its high pressure structural behaviour.

1.4 Synthesis of Carbon Nitride Materials

Two main routes of synthesis have been investigated to achieve nanocrystalline or bulk carbon nitride materials ; the deposition of thin layers of material in the form of films using chemical or physical vapour deposition (CVD/PVD) techniques and the use of high-pressure/high-temperature methods.

1.4.1 Chemical and Physical Vapour Deposition Methods

Many attempts have been made to prepare predicted super-hard carbon nitride materials metastably using CVD or PVD techniques[23,27,28]. However, although several successful syntheses have been reported, and high hardness properties have been claimed in some studies, the materials have not been fully characterised in terms of their structure or chemical composition. This is mainly due to the fact that the products tend to be very heterogeneous and the nano or micro crystalline component of the materials often constitutes only a very small proportion of the sample and the tiny crystallites are embedded within an amorphous phase.

Early attempts to synthesise carbon nitride coatings were reported in the early 1990s, these used plasma CVD with $NH_3/CH_4/H_2$[29], CH_4/N_2 or NH_3/CH_4[30] gas mixtures as precursors. These all resulted in amorphous C/N

coatings. Niu et al.[31] and Yu et al.[32] were first to claim the synthesis of a crystalline C_3N_4 phase. The former group used intense pulsed laser ablation of a graphite target combined with irradiation by an atomic nitrogen beam to prepare thin films of carbon nitride materials. The latter team used radio frequency (RF) sputtering of a pure graphite target in a nitrogen atmosphere. Both groups claimed their the products contained or consisted of β-C_3N_4 There have since been many similar CVD and PVD experiments that claimed to give products containing α- or β- C_3N_4 or a mixture of various C_3N_4 polymorphs according to different interpretations of the X-ray or electron diffraction analysis.

However, in 1999 Matsumoto et al.[33] speculated that all of these claims may be wrong. They produced simulated X-ray powder diffraction patterns for the proposed hard structures of C_3N_4. In a detailed and systematic analysis these were then compared to experimental X-ray and electron diffraction patterns of many materials claimed to be or to contain these forms of carbon nitride. In all cases studied it seemed that the most likely candidates for the fraction of the products claimed to be C_3N_4 were disordered polytypic diamond, lonsdaleite, or the silicon commonly used as a substrate in the experiments. Also the determination of the elemental compositions of the materials *via* techniques including XPS or energy dispersive X-ray analysis (EDX) and electron energy loss spectroscopy (EELS) in a TEM experiment were generally not considered sufficiently accurate for providing an accurate quantification for such light elements including carbon, nitrogen and perhaps also hydrogen and oxygen present in the sample. Even when it was possible to accurately quantify the carbon and nitrogen content in these materials, and detect or eliminate the presence of oxygen or other impurity atoms, it was not possible to gain any

information on the hydrogen content. This hydrogen content was generally ignored by most of the authors even though its presence was clearly indicated by FTIR spectroscopy. From this exhaustive analysis Matsumoto et. al.[33] concluded that no definite evidence had been provided for the existence of a successful synthesis of C_3N_4 with any of the predicted dense structures. There is still no unambiguous evidence of hard crystalline phases containing only carbon and nitrogen produced using CVD/PVD methods. However some amorphous and partly crystalline carbon nitride coatings have been shown to be very hard and often have other interesting functional properties[34].

1.4.2 Bulk Synthesis Methods for Carbon Nitride Materials

It was thought that HP/HT techniques, similar to those used to form diamond and cubic-boron nitride could be employed in the synthesis of hard C_3N_4 materials. Such syntheses require starting materials with high nitrogen contents and low hydrogen contents.

Because of the very high stability of the N_2 molecule the preparation of C_3N_4 materials should not really involve the use of overly high temperatures as there is a tendency for the materials to convert to thermodynamically stable nitrogen and graphite (or diamond) even at moderately elevated temperatures. So high pressures are necessary but temperatures should not be too high. It is also known that the application of high pressure often aids the crystallisation of 'reluctant' substances (e.g. B_2O_3) in which strong covalent bond formation impedes nucleation and growth [35].

In 1990 Wixom attempted to synthesise C_3N_4 using shock wave compression of pyrolysed melamine-formaldehyde resin and a tetrazol

derivative[36]. However diamond was the only detectable crystalline phase produced. Sekine et al. conducted high pressure pyrolyses of tetracyanoethylene or TCNE (C_6N_4) and 1,3,5-triazine ($C_3H_3N_3$) which produced graphitic like materials with very low nitrogen contents, typically below 20%[37]. Pyrolysis of *N*,*N*-diethyl-1,4-phenylendiammoniumsulphate ($C_{10}H_{18}N_2O_4S$) in a nitrogen atmosphere with an SeO_2 catalyst performed by Martin-Gil et al gave a heterogeneous product containing crystalline carbon nitride grains with a structure identified as related to zincblende from high resolution TEM and electron diffraction analysis of the sample[27]. This material was proposed to be C_3N_4 generated by the incorporation of molecular nitrogen at 800˚C in the following reaction.

$$C_{10}H_{18}N_2O_4S + 8N_2 \rightarrow 3C_3N_4 + CO_2 + 6NH_3 + SO_2$$

The small (5-50 nm) crystallites were embedded in an amorphous matrix and it was not possible to fully characterise the material or estimate its chemical composition reliably, however.

The first report of nitrogen rich carbon nitride formation in a diamond anvil cell experiment came from Nesting et al. in 1998[28]. TCNE (C_6N_4) was taken to 42 GPa and 2500˚C to form a carbon nitride material that did not contain any cyano groups identified by FTIR spectroscopy. However, on decompression the material decomposed into molecular nitrogen, diamond and carbon nitride phases with very low nitrogen contents. High pressure pyrolysis at 115 GPa and 2500 ˚C of TCNE and cyanuric triazide (C_3N_{12}) was also attempted but a detailed analysis of the diffractogram was not possible as it contained strong signals originating from the metal used as the gasket in the diamond anvil cell.

Lu et al. performed a solvothermal synthesis of carbon nitride using cyanuric chloride and lithium amide in benzene at 350 ˚C and 5-6 MPa to form a material reported as α and β-C_3N_4[38-40] however the reliability of these studies has not been verified.

High energy ball milling is another technique that has been used to generate carbon nitride materials. This technique can be used to reach pressures of up to 5 GPa with high temperatures; the high pressure and temperature occur at very localised spots in the reaction mixture. Fahmy et al. used this technique to react pure graphite with liquid ammonia in a high energy ball mill[41]. The products showed a nano-crystalline phase which, according to various analyses including XRD, EELS, FTIR, XPS and HR-TEM, could be β-C_3N_4. In another ball milling synthesis graphite nano powder was reacted with ammonia and the products were reported to contain nano crystals of β-C_3N_4 as indicated by diffraction data, but again there was no clear information on the composition of the crystallites[42].

Many other reports of synthesis of hard crystalline forms of carbon nitride using various techniques have been described in the literature but a detailed analysis of the bulk synthetic approaches show that although many nitrogen rich materials have been generated there has been no unambiguous characterisation of a C_3N_4 network to date. However, it remains possible to use organic precursor routes to design and create graphitic layered materials that could be transformed into one of the hard, tetrahedral forms of C_3N_4 under the action of heat and pressure.

Apart from the work done on the direct synthesis of hard forms of C_3N_4 there have also been many attempts at making a graphitic derivative of C_3N_4. It

is well known that pure carbon graphite and boron nitride both convert to dense tetrahedrally bonded phases under high pressure and temperature treatment to give the hardest known materials diamond and cubic boron nitride respectively. As with the pure carbon system it is likely that the graphitic form of C_3N_4 is more stable under ambient conditions than any of the theoretical tetrahedrally bonded low compressibility phases. It therefore follows that the graphitic form of carbon nitride may be a possible precursor to the β form (or one of the other forms). Hence there is a great deal of interest in the solid state chemistry of such materials. Apart from the potential applications of graphitic C_3N_4 as a precursor to the other, hard forms it also displays an interesting chemistry of its own. The high pressure/high temperature syntheses and chemistry of this graphitic phase of carbon nitride is what we are predominately interested in for this work. Below follows a brief discussion of the various attempts to produce the graphitic form of the material that have so far been reported in the literature.

1.4.3 Syntheses of Graphitic Carbon Nitride

High-pressure, high-temperature synthesis approaches have been used to prepare relatively well crystallised graphitic carbon nitride materials by reaction between precursors such as the heterocyclic aromatic compounds melamine and cyanuric chloride, forming layered solid state compounds via a lateral condensation or elimination type reaction between the planar aromatic rings. The pressures used are on the order of around 0.5-4 GPa and temperatures of between 400-600 °C[7,8,22,24], much lower than those used in attempts to achieve the synthesis of the high-density sp^3-bonded carbon nitride materials previously discussed.

Kouvetakis et al. first developed a single source precursor CVD route to a nanocrystalline graphitic carbon nitride structure in the form of thin films using the reaction below[23]. (Figure 4).

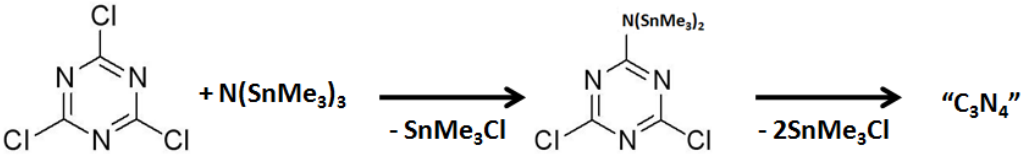

Figure 4. Reaction scheme to produce graphitic C_3N_4.

The pyrolysis involved the thermal decomposition of the precursors *via* the elimination of $SiMe_3Cl$ to form thin films. The products were analysed using Rutherford backscattering (RBS) to establish the chemical composition and a near ideal composition ($C_3N_{3.9}Sn_{0.07}$) was found. No hydrogen was detected. A combination of EELS and NMR spectroscopy showed that the C and N atoms were sp^2 hybridised and FTIR spectroscopy indicated the absence of C≡N bonds. The authors concluded that the material had the theoretically proposed structure of graphitic carbon nitride (Figure 5).

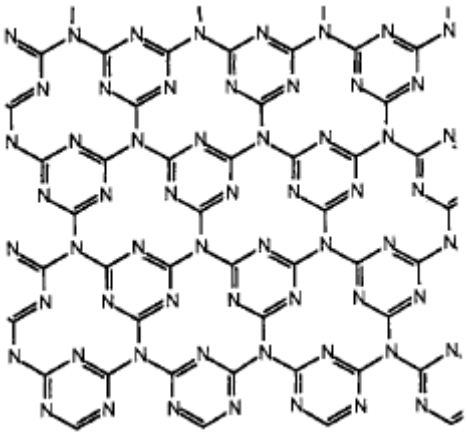

Figure 5. Proposed structure of graphitic C_3N_4

However, this material remained nanocrystalline and its structure could only be characterised using electron diffraction methods.

Preparation of a similar graphitic carbon nitride material based on a network of linked triazine rings was attempted by Montigaud et al[24]. using solvothermal techniques. The starting materials were cyanuric chloride and melamine in the presence of ethyl-diisopropylamine at 130 MPa and 250˚C. Interestingly, the recovered solid material exhibited a few broad X-ray diffraction bands indicating a graphitic structure that was slightly more crystalline than the CVD product reported by Kouvetakis et al. The authors reported their material as being a 'novel graphitic C_3N_4'. However no information on the hydrogen content or the carbon to nitrogen ratio was provided and it is likely that the product was actually more similar to the C/N/H polymer melon[1,10-11] with formula $C_6N_9H_3$, or a related material containing chlorine (see below). This group then reported the pyrolysis of melamine in the presence of the nitriding solvent hydrazine (NH_2NH_2) under high pressure conditions (3 GPa and 800-850 ˚C) and formed an even better crystallised form of graphitic carbon nitride (Figure 6)[24]. However it was still not possible to fully index the broad X-ray patterns.

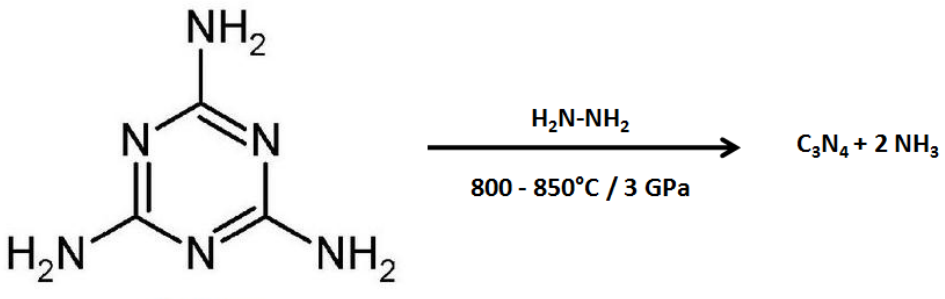

Figure 6. Reaction scheme proposed for the high-P,T synthesis of graphitic C_3N_4 from melamine.

This product was determined to contain significant amounts of hydrogen.

Demazeau et al[22] then investigated mixtures of melamine and cyanuric chloride reacted at a pressure of 0.13 GPa and 250°C and obtained a carbon nitride material that exhibits a broad X-ray diffraction peak at ~3.27 Å that is clearly due to the (002) reflection related to the interlayer spacing in the graphitic solid. Bulk chemical analysis of the product revealed the presence of hydrogen and chlorine within the material. Alves et al[22] took melamine and hydrazine (NH_2NH_2) and pressurised them to 3 GPa at 800-840 °C to give a much better crystallised graphitic carbon nitride material that could be indexed with an orthorhombic cell. This material also appeared to contain a relatively large amount of hydrogen. The high-P,T syntheses described in this thesis are based on these synthesis approaches.

Another method for preparing graphitic carbon nitride is based on the reaction of cyanuric chloride with metal nitrides or amides; the main problem in these syntheses is the removal of the metal chloride side product from the polymer. Khabashesku et al. made carbon nitride powders and spherical carbon nitride nano-structures using solid state or solution techniques[43,44].

$$C_3N_3Cl_3 + Li_3N \rightarrow \text{“}C_3N_4\text{”} + 3LiCl$$

Interestingly it seemed that the presence of materials such as glass wool during the reaction had a catalytic effect resulting in the formation of hollow spheres. There have been reports of the formation of graphitic carbon nitride nanostructures, i.e. spheres and tubes. Guo et al. demonstrated synthesis of tubular luminescent polymeric networks of graphitic carbon nitride using a one

pot solvothermal route[5]. The product was characterised as $[(C_3N_3)_2(NH)_3]_n$ and it is suggested to be structurally related to the proposed graphitic C_3N_4 polymorph. The reaction involved the polymerisation of cyanuric chloride and ammonium chloride in benzene in a sealed autoclave and heated to 300˚C.

Within the group at Arizona State University, Zhang et al[8] built on the work reported by Demazeau et al. in Bordeaux[7] and carried out systematic synthesis and characterisation studies of carbon nitride materials produced by high-pressure, high-temperature reactions between cyanuric chloride and melamine at 1-1.5 GPa and 500-600 °C. These led to well crystallised graphitic carbon nitride materials that were determined to contain a stoichiometric amount of HCl derived from the synthesis resulting in a formula of $C_6N_9H_3$.HCl [8]. The materials obtained were better crystallised than the previous graphitic carbon nitride phases obtained previously, and the X-ray diffraction patterns showed a large number of well-resolved reflections that could be analysed using Le Bail refinement methods. The chemical composition was determined using a combination of bulk analysis and EELS techniques. It was proposed that the synthesis and crystal growth were optimised by the onset of the reaction and thermal decomposition which is aided by liquid phase transport within the cyanuric chloride which occurs between a pressure of ~1.3-2.2 GPa and a temperature of 500-550 °C which the reaction conditions were controlled to stay within[45].

The yellow substance obtained is a derivative of the previously predicted graphitic C_3N_4 structure. Analysis of the powder XRD data indicated a hexagonal space group and a structure consisting of layers of a two-dimensional $C_6N_9H_3$ (triazine) network, which is structurally related to the theoretical

graphitic form of C_3N_4. The structure contains large voids or holes in which reside the chloride ions that remain part of the structure after synthesis. An equivalent number of nitrogen atoms in the framework are protonated for charge balance. The structure of one layer of this material is shown in Figure 7.

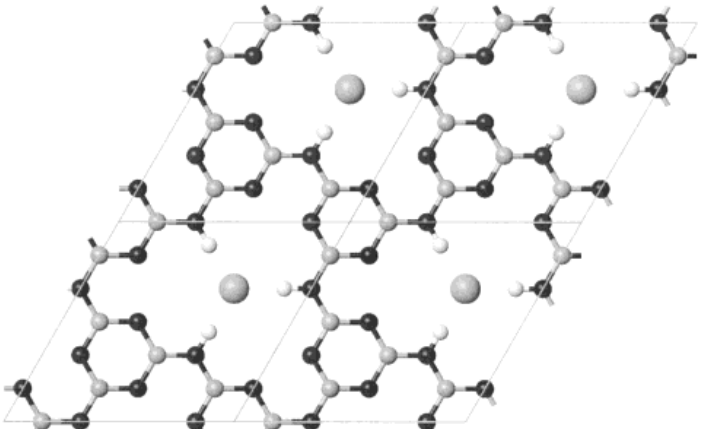

Figure 7. Proposed structure of $C_6N_9H_3.HCl$.

The structural model is related to that proposed by Kouvetakis et al.[23]. However, this material has one third of the C_3N_3 triazine rings missing. The resulting voids in the graphene planes are occupied by chloride ions with an equal number of protonated nitrogen sites in the framework. The IR and ^{13}C NMR data were consistent with this model and stoichiometry. No Raman data could be obtained however because of intense fluorescence in the visible range.

The work presented in this thesis was designed to reproduce and refine the synthesis of the $C_6N_9H_3.HCl$ material and extend the characterisation of its graphitic ring structure using UV and FT near-IR Raman spectroscopy. We also refined the structural model by combining new X-ray diffraction data with results of the density functional calculations carried out in a parallel theoretical PhD project by M. Deifallah at UCL. The first principles theoretical calculations gave new information on the attachment of hydrogen atoms to nitrogen sites

within the graphitic layers and this information was used to construct a new structural model that was in better agreement with the X-ray diffraction results.

We used our well crystallised graphitic material to investigate the compression behaviour at high pressure that could lead to new dense carbon nitride phases. Previously the high pressure behaviour of $C_6N_9H_3$.HCl was investigated by Wolf et. al.[45] Indications of an onset of structural disorder/amorphisation were observed when the material was subject to pressures above 30 GPa. Here we extended the structural study to above 60 GPa into a regime where the crystalline diffraction features were lost. Comparison with the theoretically predicted compression behaviour allowed an interpretation of the results in terms of a likely new mechanism for interlayer bonding within the graphitic carbon nitride material at high pressure, leading to a new family of high density materials.

Chapter Two – Experimental Methods

2.1 Introduction

During the work reported here two different types of high pressure experiments were carried out. First organic solid state synthesis techniques were used to produce graphitic carbon nitride layered phases from mixtures of heterocyclic organic precursor molecules at pressures of 0.5-1.5 GPa and T~500^{o}C in a piston cylinder device. We also attempted to observe the synthesis reaction by *in situ* synchrotron energy dispersive X-ray diffraction using the multi-anvil device mounted at station 16.4 at Daresbury SRS.

Various techniques were used to study the structure and properties of the samples recovered to ambient pressure, including powder X-ray diffraction, FTIR spectroscopy and Raman scattering. During the Raman studies, it was found that the samples were strongly fluorescent to all wavelengths of light used for visible excitation, so the application of the specialised techniques of UV and near-IR Fourier transform Raman spectroscopy were explored to study their structural nature. During this part of the study it was discovered that the samples provided useful models for the "tholins" that were being prepared and studied as models for materials produced in the upper atmosphere of Titan. As an extension of the original study, collaborations were entered into with the research group led by Dr. E. Quirico from the Planetology Laboratory within the Institute of Physics at the University Joseph Fourier in Grenoble, France. That collaboration led to new insights concerning the interpretation of the spectra and the structures of graphitic carbon nitride materials in general. In turn, the well-crystallised

samples produced by high-pressure, high-temperature synthesis from heterocyclic aromatic precursors permitted a new interpretation of the data for the tholin materials. The results were of planetary and astrophysical significance and results including our preliminary data have been published[46]. During the studies X-ray diffraction, Raman and FTIR spectroscopy investigations were also carried out on the various tholin samples prepared by and for the Grenoble group as part of the Titan planetology investigations.

Experiments were also carried out *in situ* to explore the compressional behaviour of the layered graphitic C,N compounds in the diamond anvil cell (DAC) to pressures as high as 60 GPa, to explore the onset of amorphisation and the possibility of synthesising novel sp^3-bonded materials using laboratory spectroscopy (Raman, fluorescence, FTIR) and synchrotron X-ray diffraction (Daresbury SRS, station 9.5) to study the structural changes. These changes were later investigated in a parallel theoretical study using ab initio density functional techniques by Malek Deifallah and Dr. Furio Cora at UCL as part of the PhD thesis of Malek Deifallah, working in collaboration with our group. Some of the theoretical results are reported here to aid in the interpretation of our experimental results.

The experimental methods and techniques used in these studies are described in the sections below.

2.2 High Pressure – High Temperature Synthesis Experiments

2.2.1 Piston Cylinder Apparatus

The high pressure/high temperature synthesis experiments were carried out using a 'Depths of the Earth Company'[47] 'Quickpress' device which is a non-end loaded piston cylinder apparatus[48,49] installed in the high pressure laboratory at UCL. The apparatus is a compact, hand pump operated device that can be used to simultaneously generate high pressures and temperatures within a sample. It is particularly useful for synthesis experiments carried out in a pressure range between 0.2-4 GPa, at temperatures ranging up to ~1800 ^{o}C. In the present studies it was used to synthesise solid graphitic C-N-H samples reproducibly from mixtures of heterocyclic aromatic precursors at pressures between 0.5-2 GPa and temperatures of ~500 ^{o}C. Sample amounts between 50-100 mg could be obtained in a single synthesis run.

The basic principle of such an instrument is to generate a high pressure in and around a sample by compressing a sample assembly, which usually includes a resistance heater, held inside a pressure vessel.[48]

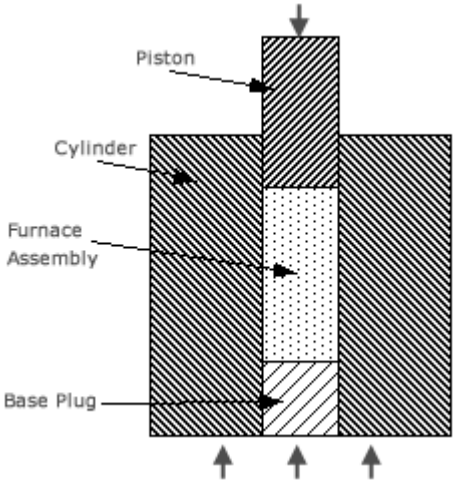

Figure 8. Cross section of furnace assembly inside pressure cylinder.

The apparatus consists of a small tungsten carbide piston that is forced into a cylindrical area inside a carbide core that contains the sample surrounded by the pressure transmitting medium and heating assembly, pressure is generated by the compression of this furnace assembly. The piston sits on top of the sample assembly within a cylindrical sample chamber which sits between two high pressure plates. The pressure is increased by raising the lower plate using a ram controlled by a hydraulic hand pump. The area of the piston that is in contact with the sample assembly is a lot smaller than the area of the plate so it is possible to produce very high pressures. This is because pressure is proportional to force per unit area, so the smaller the area to which the force is applied, the higher the pressure:

$$P = \frac{F}{A} \tag{1}$$

Where F is the force applied and A is the cross-sectional area.

High pressures are generated by applying a relatively small load to a large piston; this then supports and drives the smaller tungsten carbide piston which is the part that applies the force to the sample assembly. This arrangement results in a pressure amplification of;

$$(r_1/r_2)^2 \qquad (2)$$

where r_1 and r_2 are the radii of the large and small pistons respectively. Therefore applying a pressure of 10 MPa to a primary piston with a diameter of 15cm will give a pressure of 1 GPa for a secondary piston with a 1.5 cm diameter.

The pressure is dependent on the surface area of the end of the piston used to apply the force and a smaller size of cylindrical sample chamber. The pressure plate used with this apparatus gives a maximum pressure of 25 kb and has piston and cylinder diameter of 1.25 cm. In practice non-end-loaded piston cylinder systems are limited to about 5 GPa due to the strength of the materials used to construct the pressure vessel. In this case the cylinder, plate and piston are made from tungsten carbide. The high hardness and compressive strength of the material make it able to withstand the very high pressures involved.

The temperature of the sample in a piston cylinder device is controlled by passing a regulated low voltage and high current through a cylindrical graphite furnace which surrounds the sample capsule (figure 10). The temperature of the capsule is measured by a tungsten-rhenium $W_{26}Re_{74}$-W_5Re_{95} alloy thermocouple which is situated at the base of the sample capsule.

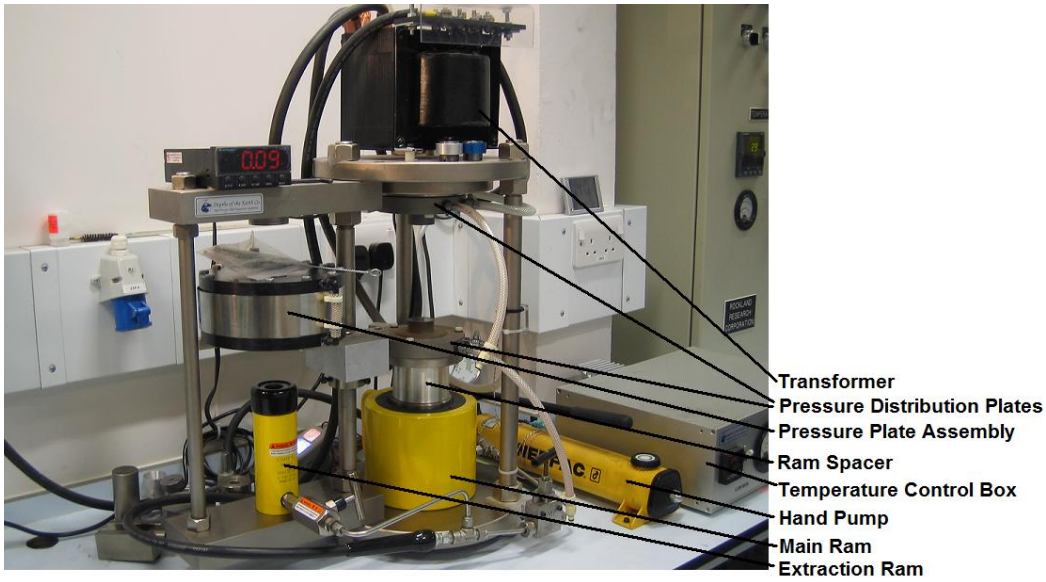

Figure 9. Piston Cylinder Apparatus.

2.2.2 Preparation of a Piston Cylinder Experiment

i. Loading the Sample Capsule

During the synthesis the starting materials are contained within a noble metal capsule, for the syntheses performed in this project this was usually platinum. The capsule is constructed using a short length of platinum tubing, approximately 15 mm, outer diameter 5 mm and inner diameter 4.5 mm. One end of the length of tube is sealed shut by crimping with pliers and/or may be welded. The starting materials are then loaded into the capsule in the form of a pressed pellet for powdered solid samples and the other end of the tube is also crimped shut. This end was not welded to prevent reaction/decomposition of the starting materials before the experiment commences. In the experiments described here, the starting materials were often air or moisture sensitive. For that reason, the capsules were loaded and sealed in a dry-box under an argon atmosphere.

ii. Preparation of Thermocouple

The thermocouple wires are made of the tungsten-rhenium alloys $W_{26}Re$ and W_5Re encased in Teflon. The stripped end of each wire is pushed through a bore in a 4.5 cm length of 4-hole alumina tube to form a crossed contact at one end that is flush with the end of the alumina tube. The last few centimetres of the wires that are furthest from the functioning alumina end of the thermocouple are left exposed from the Teflon casing to enable connection to the thermocouple terminals to allow temperature control in the system

iii. The Sample Assembly

The sample assembly is constructed as shown below (figure 10). The assembly consists of a tungsten carbide support block and base plug on top of which sits a circle of gasket paper which acts as an insulating medium between the support block and the pressure cylinder. The thermocouple is pushed through the hole in the middle of the support block. On top of this is then placed a base plug surrounded by a Pyrex glass insulating sheath. A crushable magnesia tube is then placed over the rest of the exposed length of the thermocouple and rests on the base plug. An alumina disk is then placed on the very end of the thermocouple. A cylindrical graphite furnace is then slotted over the magnesia tube on top of which the sample capsule sits. The thermocouple measures/controls the temperature at the base of the sample capsule. Silica powder is packed on top of and around the sample capsule and a small magnesia bushing plug is placed on top of this to fill the remaining space inside the furnace. The whole furnace is then surrounded by a sleeve made of compressed sodium chloride which is used as a pressure transmission medium. Lead foil is

then placed around the pressure transmission sheath to aid with lubrication when the assembly is inserted into the pressure plate.

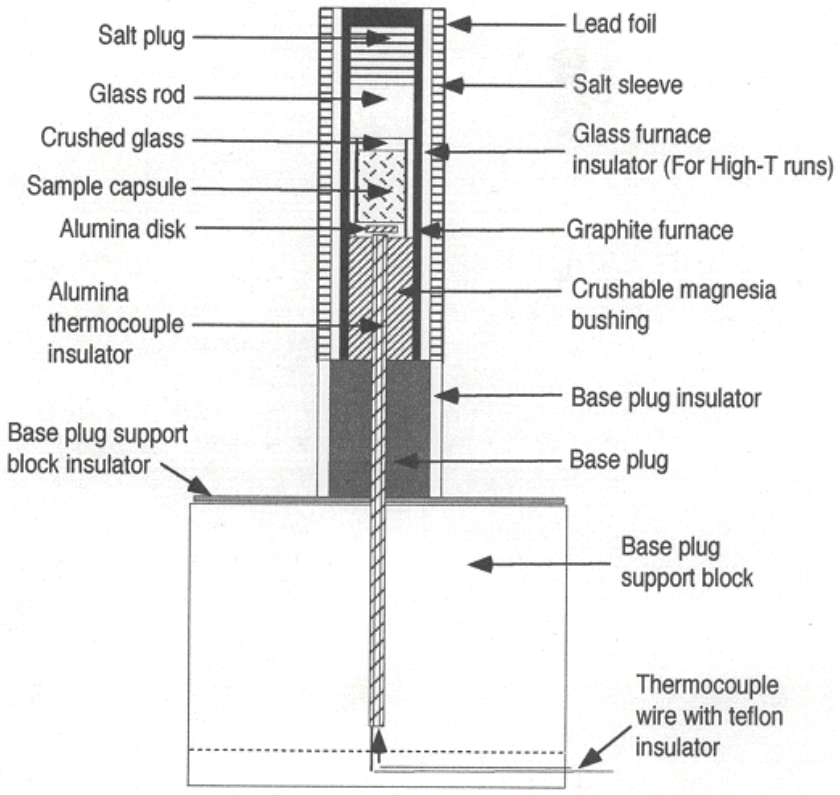

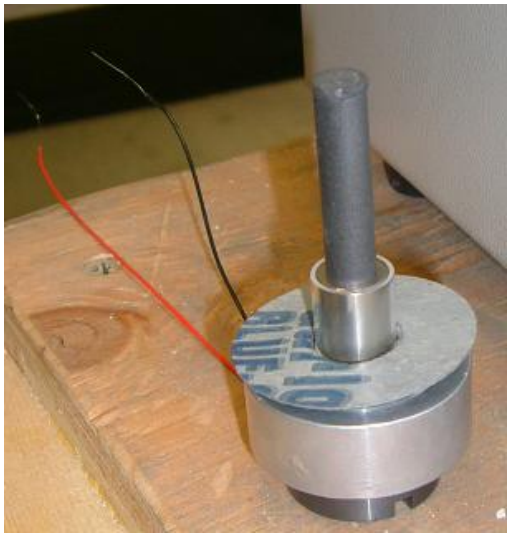

Figure 10. Piston cylinder furnace Assembly for High-Temperature Experiments.

iv. Conducting an Experiment

The furnace assembly is inserted into the cylindrical chamber in the tungsten carbide pressure plate as shown in the diagram below (figure 11), the inside of which has been lubricated with "Molycote", an MoS_2 lubricant to allow friction free compression. The greased piston is then placed on top of the assembly with the piston support block on top. The pressure plate is rotated into the run position and aligned with the pressure distribution plates. The thermocouple wires are then connected to the correct terminals to allow temperature control during the experiment. The lower pressure distribution plate is brought up by raising the ram using a hydraulic hand pump. The ram is raised until the required pressure, plus 10%, is attained. This technique is known as “hot piston out” procedure. The pressure initially attained is more than that required for the experiment to allow for the friction that is present at low temperatures. The cooling water is then allowed to flow around the system and the temperature is then increased. During heating operating conditions, including pressure, are monitored and adjusted accordingly to maintain the correct conditions until the required temperature is reached. The extra pressure is released to attain the required run conditions and the conditions are monitored during the experiment.

For the experiments conducted during this project the pressures used were in the region of 1-1.5 GPa with a temperature of 500-600 ˚C with run times of up to 20 hours.

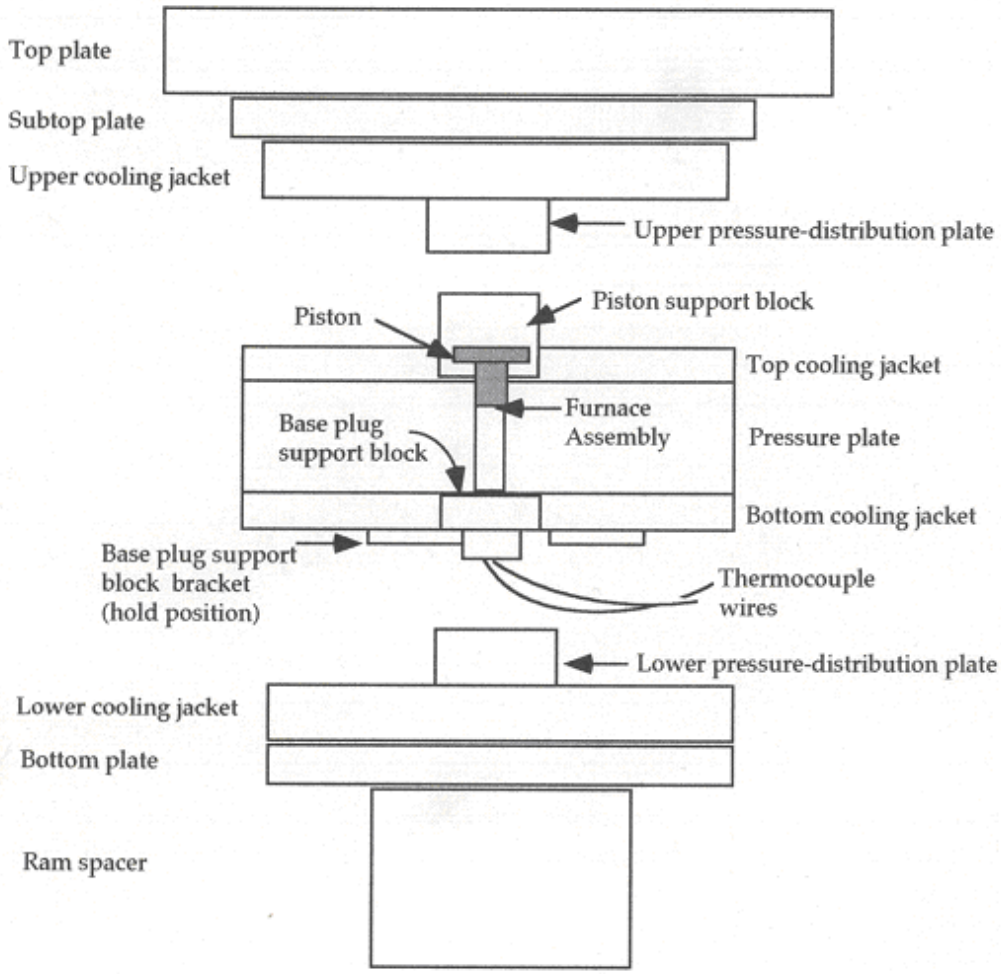

Figure 11. Schematic Diagram of Run Position (top). Pressure plate in run position (bottom) in the piston cylinder apparatus.

v. Terminating an Experiment

For the experiments conducted during this project the ‘isobaric quench’ method was used for termination of experiments. The temperature controller is turned off and the pressure is maintained during the quench by manually pumping as necessary as the system cools. Below 100 °C the pressure can slowly be released from the system and the flow of cooling water can be stopped below 60 °C.

vi. Recovering Samples after an Experiment

When the pressure is fully released the base plug is removed and the protruding end of the thermocouple cut off (figure 12). The pressure plate with the sample assembly still inside the cylinder is then rotated over to the extraction ram (figure 13) with the extraction piston and safety sleeve in place. The plate is aligned with the extraction piston and the pressure in then increased using the hand pump. The piston then pushes out the sample assembly until it is completely removed from the cylinder.

The sample assembly is removed from the apparatus and the sample capsule is recovered by sifting through the remains of the assembly (figure 14). The capsule is then opened and the final material carefully removed (figure 15). It can be seen that the material varies slightly in colour at opposite ends of the capsule. This is a demonstration that a temperature gradient can be present when such experiments are conducted in the piston cylinder. It is therefore important that the apparatus is assembled very carefully and that the sample capsule is not allowed to be too long to minimise the effect of this gradient.

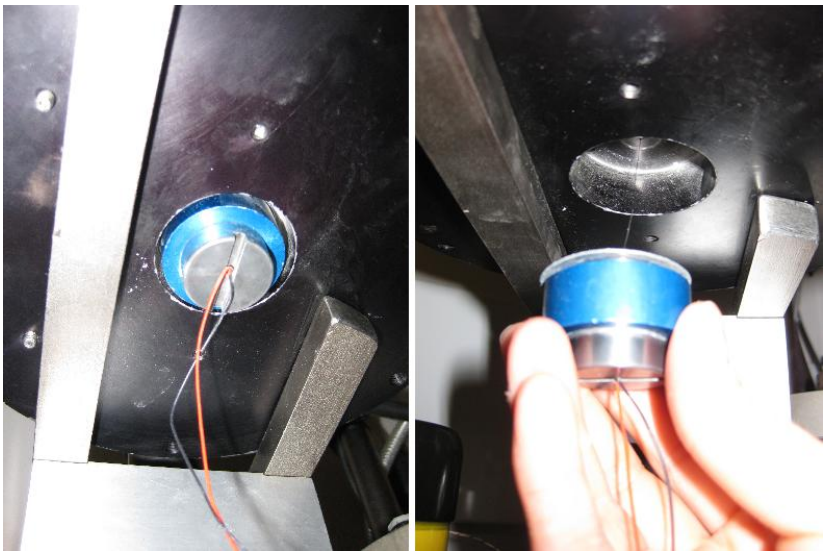

Figure 12. Removal of the base plug after piston cylinder experiment.

Figure 13. Extraction of the sample assembly from piston cylinder.

Figure 14. Removing the sample capsule from the piston cylinder assembly after compression.

Figure 15. Extracting the sample from the capsule after a piston cylinder experiment.

2.3 Multi Anvil Press used at Daresbury SRS for *in-situ* Synchrotron Experiments

This section is included for completeness due to the volume of work involved even though the use of the technique failed to provide useful results.

The multi-anvil apparatus is a high-pressure synthesis device that can be used to take materials up to much higher pressures than the piston cylinder apparatus and is the intermediate, in terms of the pressure and sample volume achievable, apparatus between the piston cylinder and the diamond anvil cell (which will be discussed in more detail later in this chapter). The multi anvil device that was available for use during this project is capable of taking samples up to pressures of approximately 25 GPa and temperatures of up to about 2000 °C.

The principle of the multi anvil apparatus is to compress a sample volume in the shape of a regular polyhedron from all sides at once using a number of identical pistons that are pushed towards each other[50]. In the apparatus described here an octahedral geometry was used for the sample environment.

The press used was installed for *in situ* high pressure-high temperature experiments on beamline 16.4 at the Daresbury SRS. The press consists of a ram of 18 inches in diameter which is capable of producing a force of 300 tonnes. Upon this ram sits a 'Walker module' which has a split cylinder geometry with 6 wedges that surround the sample assembly[51,52] (figure 16). The sample sits in a boron nitride capsule which is held inside a cast ceramic octahedron[53], which is in turn surrounded by eight tungsten carbide cubes with a truncation on one corner which sits on the faces of the octahedron holding it in place (see figure 17).

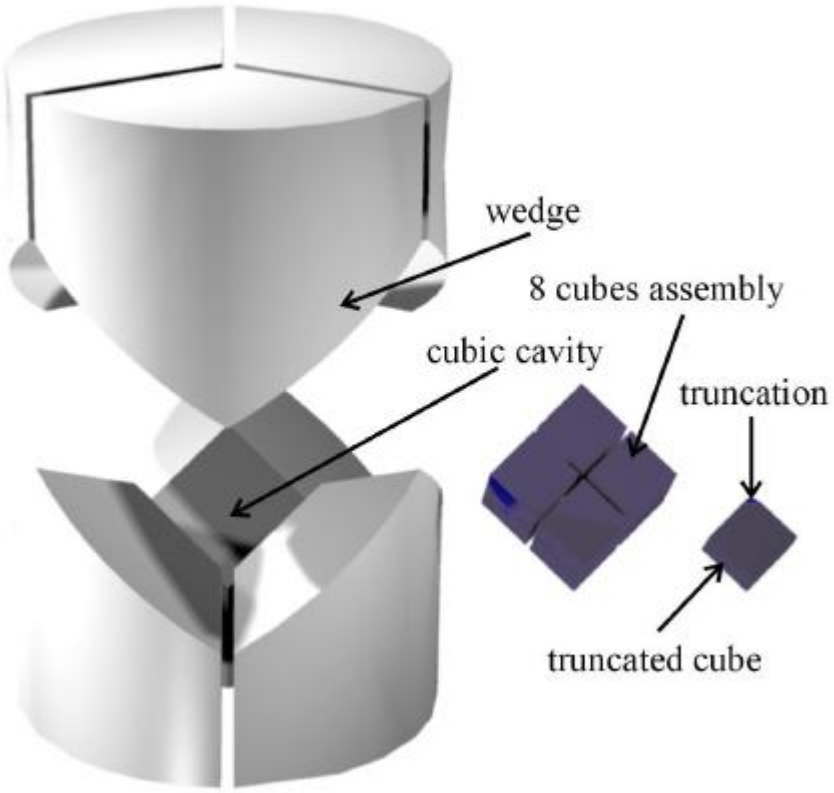

Figure 16. Schematic representation of the Walker module at the centre of the multi anvil press apparatus.

The area of the cube truncation determines the pressure achievable for the experiment. So the smaller the truncation on the cubes the higher the pressure

available, the experiments conducted in this work used cubes with truncations of 8 mm and octahedra with edges of 14 mm allowing pressures of up to 12 GPa with the press used here.

The sample assembly consists of the outer octahedron cast from a refractory ceramic material called 'Ceramcast'^{TM} (mainly a mixture of powdered MgO and Al_2O_3 with other additives) the sample is enclosed in a thin boron nitride (BN) sample capsule which was not found to react with the sample material. This sample capsule sits within a graphite cylinder which acts as a resistance furnace in a similar manner to that in the sample assembly used for piston cylinder experiments. The temperature is controlled by the thermocouple which sits next to the sample capsule within the octahedron. The ends of the hole in the octahedron are then capped with magnesium oxide (MgO) discs with metal electrodes embedded in them so a current can be passed to the resistance heater inside.

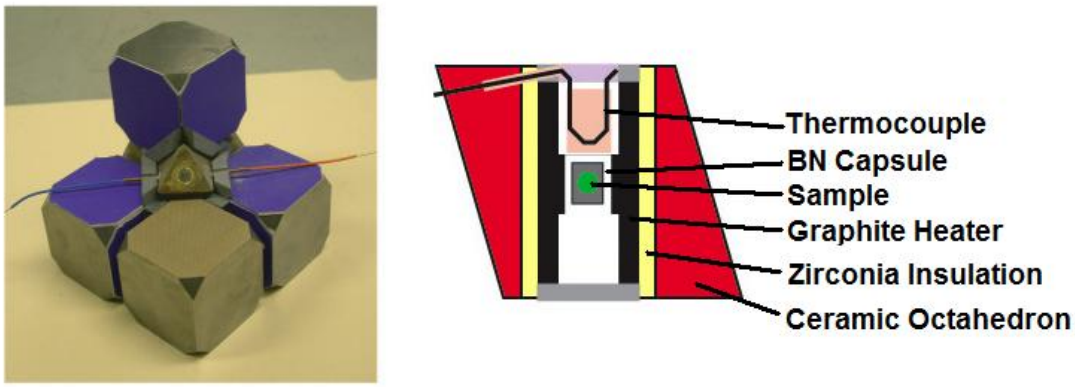

Figure 17. Truncated cube assembly (5 out of 8 shown) that compresses the octahedral sample assembly (left). This would be situated at the centre of a multi anvil module. Cross section of octahedron showing sample assembly inside (right).

The press installed at beamline 16.4 at the SRS was used in several attempts to study the processes occurring during the formation reactions leading

to the synthesis of the graphitic carbon nitride material at high P,T conditions. However, the press setup at this facility was found to be particularly unreliable and this led to considerable frustration during repeated multianvil runs. The main failures occurred due to the thermocouple breaking during the runs: also the carbide cubes cracked on several occasions. We concluded that these failures were because of an inherent design flaw in the apparatus. Because the multianvil device was mounted with its pressurisation axis horizontal (to allow passage of the X-rays between the anvil cubes), added tangential strain was placed on the pressurising components. This instrument is no longer in use and the Daresbury synchrotron has been closed since August 2008. In addition the materials involved in the synthesis are composed from light elements that are poor at scattering X-rays compared with contributions from the sample assembly and furnace parts. It was not possible to obtain any useful data sets from the experiments performed at SRS 16.4. Because the pressure range at which the experiments in this work were carried out at the lower end of the range for the apparatus it was difficult to be sure of the actual pressure the samples were being subjected to. Because precise control of the P,T conditions is necessary for successful synthesis the attempts at *in situ* characterisation of the reaction process were also subject to further uncertainties. We generally observed a tendency for the product materials obtained following SRS runs to be 'overcooked' with a high proportion of graphite found in the product. Another factor that may have contributed to the lack of success during the Daresbury multi anvil experiments is that it is a lot harder to keep the precursor materials in an inert atmosphere when loading and setting up the experiment compared to the

piston cylinder syntheses carried out at UCL, due to the nature of the apparatus and the limited loading facilities available.

2.4 Diamond Anvil Cell

During this work the diamond anvil cell was used to investigate the high pressure structural behaviour of the C_xN_y material synthesised in the piston cylinder runs. These experiments were carried out to observe any tendency of the material to adopt sp^3 bonding or polymerisation reactions between the graphitic layers.

Diamond anvil cells (DACs) as high pressure apparatus have been known since the 1950s when they were first described by a team of researchers at the National Bureau of Standards (now the National Institute of Standards and Technology) in the USA[54], as well as by an independent team working at the University of Chicago[55]. The DAC has now been used routinely in a variety of related forms in various applications to high pressure solid state physics and geoscience since the early 1970s[50] when gasketting techniques and the ruby fluorescence method for pressure measurement[56] became available. This advent revolutionised the field of high pressure experimentation and such apparatus is now one of the most important techniques employed for the high pressure structural characterisation of materials and the study of their behaviour *in situ*.

The diamond anvil cell deals with very small sample volumes, typically several orders of magnitude smaller than the capacity of the piston cylinder apparatus previously discussed. The basic principle of the diamond anvil cell (and in fact of any high pressure device) is to generate very high pressures by

using the principle of transferring a set force from one surface to another with a much smaller area, thus multiplying the force transmitted (as equation (1) above); the typical gemstone tapered diamond shape is perfect for this purpose. The diamond anvil cell combines this principle with using the hardest known naturally occurring material, diamond, to transmit the force making it possible to attain very high pressures within the sample without the failure of the anvil (figure 18). Diamond cells use gem quality single crystalline stones for the anvils and the selection criteria for the stones will be discussed in more detail later.

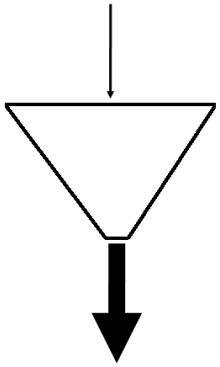

Figure 18. Schematic representation of the pressure multiplication principle employed by the diamond anvil cell. A force is applied to the large diamond table and transmitted to the sample through the small culet facet.

The use of diamond as the anvil material also helps facilitate the use of the apparatus with a multitude of spectroscopic techniques for analysis of the structure and vibrational and electronic properties due to its natural transparency to many types of electro-magnetic radiation. It is possible to do experiments *in situ* with X-ray diffraction, infra-red and Raman spectroscopy and optical microscopy with changes in behaviour being directly observable through the diamond anvil cell.

2.4.1 The Diamonds

The choice of the diamonds used in a DAC device determines the nature of the experiment that can be carried out. During these studies experiments were carried out using mainly synchrotron X-ray diffraction and FTIR spectroscopy. The qualities of the diamonds chosen or dictated by practical considerations for use in the experiments are described below. Studies were also attempted using Raman spectroscopy excited by visible light radiation but the samples showed strong fluorescence throughout the visible range and these experiments were not successful. Raman spectra were obtained for samples under ambient conditions using UV and near-IR excitation but those experiments were not possible at high pressure in the DAC. The single crystal diamond anvils are subjected to extremely high strain and must be able to withstand this force sufficiently to avoid excessive deformation and anvil failure. They must also be transparent to radiation in the range of interest. The four criteria that are applied in the jewellery industry when selecting, grading and marketing diamonds are the 'four C's' of colour, clarity, cut and carat. These are also used to determine the quality and suitability of each stone for a DAC experiment, with an additional C (cost) being taken into account.

2.4.2 Colour

The colour reflects the degree and type of impurities or defects in a stone that can be critical when choosing a diamond for a specific experiment. This is important particularly for spectroscopy experiments as any background fluorescence present in the stone would overpower the sample signal, and impurity or defect absorptions can mask the IR or visible light transmission

signal. Diamonds are tested and selected in the laboratory before purchase to determine their level of absorbance or florescence signal in the region necessary for the experiment. Diamonds are classified into ‘types’ that refer to the amount and degree of aggregation of nitrogen impurities within the crystal that relate to the effect on the optical properties;

- Type Ia – the majority of naturally found stones are of this type, they contain up to 0.3% nitrogen
- Type Ib – these are very rare in nature, only about 0.1% of natural stones fall into this category. However, almost all synthetic stones are of this variety. They contain up to 500 ppm nitrogen.
- Type IIa – also very rare in nature, they contain so little nitrogen that it cannot be easily detected by usual IR or UV absorption methods.
- Type IIb – extremely rare in natural stones. They have very low nitrogen contents (even lower than type IIa).

For a stone to be a good candidate for use in Raman spectroscopy using visible or near IR radiation it should be of type Ia with low fluorescence. This means that the diamond exhibits low fluorescence under visible laser irradiation. The fluorescence that affects Raman spectroscopy occurs in the visible range. If the sample is to be subjected to blue or green laser light then the diamond must not exhibit fluorescence in these regions. A convenient test to establish the suitability of a stone for Raman spectroscopy involves measuring its second order Raman spectrum at about 2600 cm^{-1} which should be intense when compared to the background. Stones with a ratio of the second order signal to

the background below ~4:1 are usually unsuitable for Raman studies. Figure 19 below shows the Raman spectrum of two type Ia diamond specimens. Specimen a) shows an intense, steep background that makes it difficult to ascertain the intensity of the second order peak. Specimen b) on the other hand has a perfectly flat background and a second order to background ratio of 10:1 making it suitable for Raman spectroscopy. The criteria for the selection of diamonds for infra red transmission experiments is discussed later.

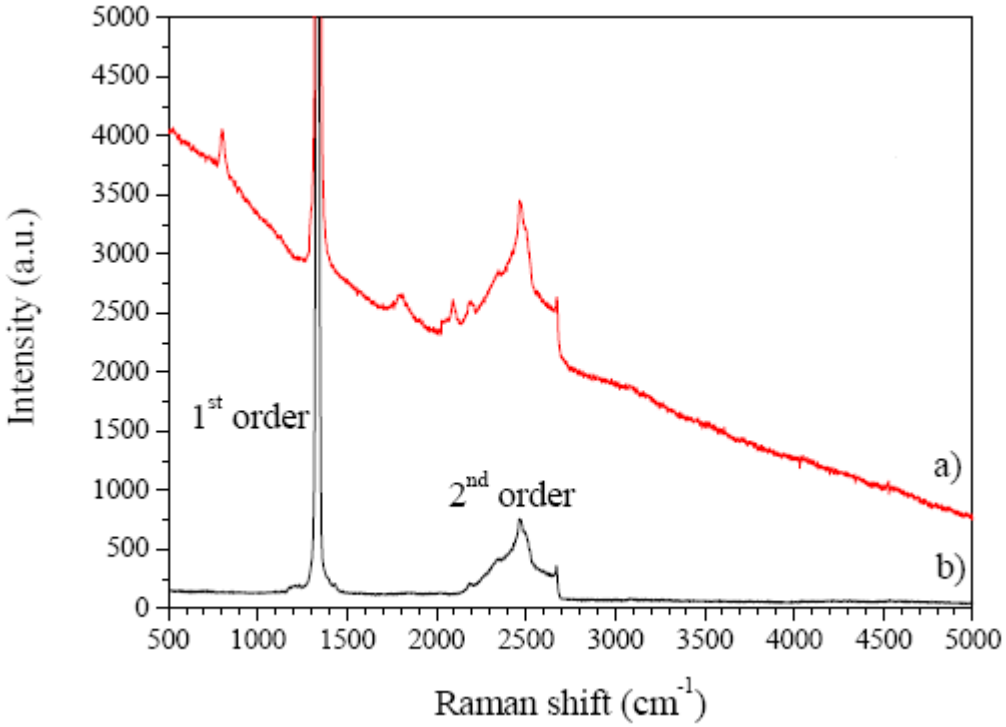

Figure 19. Raman spectrum of two specimens of typical type Ia diamond. a) a slightly yellow stone with a strongly sloping fluorescence background and is unsuitable for Raman spectroscopy. Specimen b) is a colourless diamond with little fluorescence background and a second order to background ratio of 10:1.

For X-ray diffraction experiments the colour of the diamond is not particularly important: however, the X-ray energy must be high enough that the diamond is transparent to the radiation being used. Diamond is transparent to x-rays of energy above around 10 keV for typical anvil window thicknesses of a few mm.

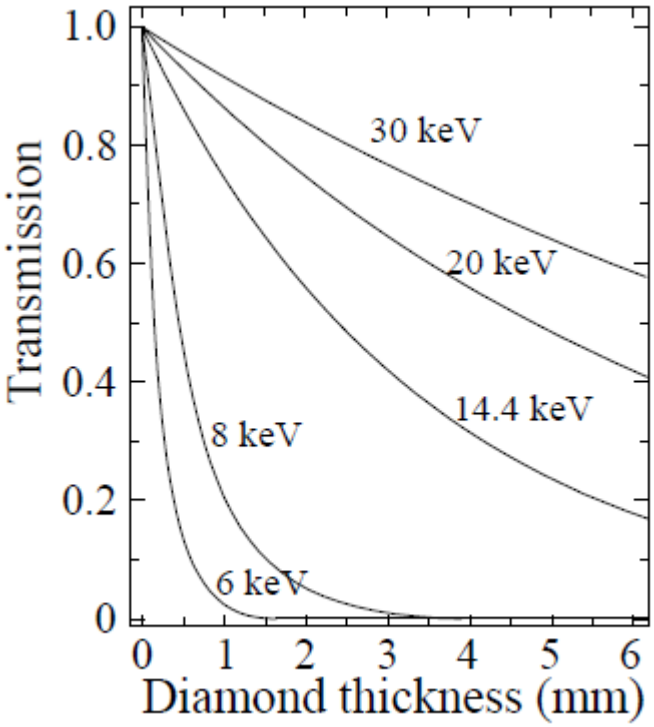

Figure 20. X-ray transmission curves through diamond for different X-ray energies as a function of diamond thickness[56].

2.4.3 Clarity

Diamonds are graded on a scale of "flawless" to "imperfect" based on the density of inclusions or defects visible under 10x magnification Flawless stones (FL) have no visible defects or inclusions, internally flawless (IF) have no observable internal defects, very very slightly (VVS), very slightly (VS), small inclusions (SI-1 and SI-2) and finally included (I-1, I-2 and I-3) containing increasing numbers and size of defects or inclusions. For diamond cell experiments it is usually necessary to use only diamonds with VVS or VS grade: VS stones are typically 15-20% cheaper than VVS[57].

2.4.4 Carat

The carat is a measure of the diamond weight; one carat is equal to 200 mg. The size of the stone limits the size of the faces available to be cut and therefore

affects the maximum pressure that can be attained. The larger the diamond the larger the sample size and pressure available for an experiment. However, as the cost increases approximately exponentially with size for a diamond of given colour and clarity and research funds are limited especially since failure can occur, high pressure experiments are typically limited to working with diamonds on the order of about 1/3 of a carat (about 67 mg) in size. Typical type Ia. The typical cost of such a stone would be around 1000 pounds.

2.4.5 Cut

Diamonds are cut in many shapes and patterns to enhance the form and play of light inside the stone for jewellery purposes. One traditional cut is the 'round brilliant' demonstrated in figure 21. Brilliant cut diamonds are the most generally available and adapted for diamond cell experiments. The large top facet is known as the table and this is usually presented as the main external surface in jewellery. At the opposite end of the diamond is the culet face, which is usually hidden inside the mounting of a stone. This facet is not always present in stones destined for jewellery purposes but it forms an important feature of diamonds used for high pressure experiments. In a typical diamond anvil cell two diamonds are mounted with their culet faces in opposition (but not touching: that would cause the diamonds to break). The sample is placed between the two culets that form a microscopic sample chamber along with the metal gasket that surrounds the sample area. The diamonds are mounted inside a mechanical device that is used to exert an external force on the diamond tables. This force is transmitted through the diamonds to the sample chamber *via* the culet face.

Because of the very large area reduction between the table and culet face this causes a large pressure to be generated within the sample chamber.

For high pressure studies in the diamond anvil cell it is essential that the surfaces of the table and the culet are highly parallel to one another. Any deviation in parallelism will put undue strain on part of the stone which will make it likely to fail at low pressures during experiment. Because of this it is also very important that the culet face axis is directly in line with the centre of the table of the anvil to again ensure that no asymmetric strain is applied to any area of the stone.

For a brilliant cut diamond of about 0.3 carats (typical for most stones used in such experiments) the diameter of the girdle is about 4.5 mm and the table is around 4 mm. For a culet face diameter of 300 μm (again typical to such experiments) pressures of up to 40-50 GPa can routinely be obtained. For experiments requiring higher pressures smaller culet faces are necessary. For example a pair of diamonds with flat 200 μm culets can be used to reach pressures of up to 80 GPa, and perhaps higher.

An approximate guide for the maximum safe working pressure of an anvil with a culet diameter of d is as follows:

$$P_{max} = 10/d \text{ GPa mm-}^{1} \quad (3)$$

This works for the kinds of stones typically used in diamond anvil experiments with a mass of up to about 60mg (0.3 carats) with a table of about 3 mm in diameter[50].

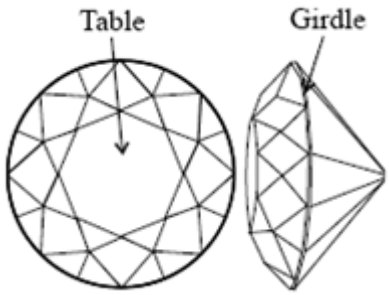

Figure 21. Schematic diagram of the diamond faces important in high pressure experimentation. The scale is on the order of a 300 μm culet and a 4.5 mm girdle diameter.

2.5 Preparation of a Diamond Anvil Cell experiment

During this work diamond anvil cells were used to undertake several types of high pressure experiment including synchrotron X-ray diffraction, infra-red spectroscopy, Raman spectroscopy, optical microscopy, resistive heating and synthesis attempts. There are many cell designs available for use and depending on the specific experiment to be undertaken; several options are open to the high pressure experimentalist. For the work undertaken here two main types of cell were used. The first was the screw driven Diacell® Diaclamp cell now marketed and produced by the company easyLab Technologies[58] (figure 22). This compact cell is based on a design developed by H-K. Mao (Geophysical Laboratory, Carnegie Institution of Washington D.C., USA). It has four screws that have opposite threads which can be tightened to apply the force to the anvils, this design also makes it possible to work easily with cryogenically loaded pressure transmitting media such as liquid nitrogen or argon. The cell has a 50° aperture making it suitable for spectroscopic and X-ray diffraction experiments even using tungsten carbide backing plates.

Figure 22. The Diacell® Diaclamp, 'Mao' type diamond anvil cell used for some of this work.

The other type of cell that was used was a pneumatically driven membrane cell, the Diacell® Bragg (G), again obtained from EasyLab Technologies[58] shown in figure 23. The gas membrane drive mechanism[59] makes it possible to apply very small incremental loads to the cell facilitating a very smooth uninterrupted increase in pressure at the sample. The cell has a lid containing a thin metal membrane that can be expanded by the introduction of a gas or other fluid that in turn pushes on the piston driving it forward and compressing the sample. One advantage of this type of cell is that it can be used at very low temperatures if helium is used as the pressurising medium. This cell was fitted with beryllium backing plates meaning that the cell body itself determines the available aperture of the cell for X-ray studies (as beryllium is essentially transparent to X-ray radiation over the range of wavelengths used) the specifications are 90° for both the top and bottom angle of this cell. However, is does mean that the anvil seats are weaker due to the softer material they are made from. This may affect the maximum pressure attainable without anvil failure for a given culet diameter.

Figure 23. The Diacell® Bragg (G) type diamond anvil cell used for some of this work.

When using tungsten carbide backing plates the diameter of the conical aperture of the diamond seat defines the maximum 4θ angle of the diffraction cone that is possible for an angular dispersive diffraction experiment using the cell. If the hole is made too big this will reduce the mechanical strength of the backing plate and reduce the amount of force it is able to withstand, this decreases the diamond support and could lead to anvil failure. If the height of the diamond anvil is too tall it will also reduce the 4θ angle, as demonstrated in figure 24. The use of the X-ray transparent material beryllium for anvil backing plates means that it is the body of the cell itself that determines the maximum available aperture.

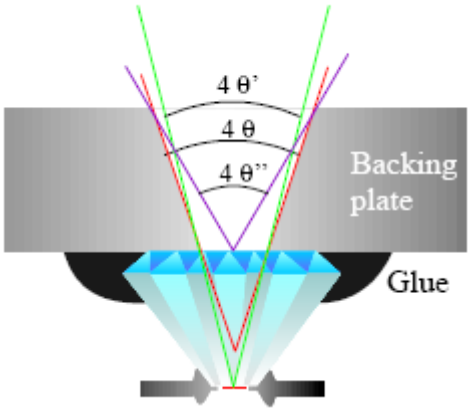

Figure 24. Picture showing the possible diffraction angles through the backing plate. The 4θ angle is the opening angle of the conical aperture of the backing plate, the angle 4 θ' is the maximum diffraction angle that can be measured and 4 θ'' is the theoretical maximum diffraction angle.

2.5.1 Seating and Mounting the Diamond Anvils

The anvil backing plates transmit the compressing force to the diamond tables, for table diameters in the region of 3 mm the seats may be subjected to pressures on the order of 2 GPa and for very high pressure experiments this may be much higher. It is therefore important that the backing plates are able to withstand the forces involved to prevent anvil failure. Most backing plates are made from tungsten carbide because of its high hardness, incompressibility and durability at high pressures. As mentioned previously in some cases for X-ray diffraction applications the backing plates can be made of beryllium so that the aperture for the diffracted radiation is minimally affected.

The tables of the diamonds must be carefully aligned over the hole in the backing plate to ensure that the culet is as central as possible so that the path of any radiation used for experimentation is not interfered with. The backing plates and diamond tables are cleaned thoroughly with abrasive paper and isopropanol to ensure no contaminants are observed during experiment and also to aid the

adherence of the glue used to stick the diamonds to the seats. The diamond is then placed on the backing plate and both are transferred to a specially designed anvil mounting jig (figure 25). This is used along with an optical microscope to align the diamond on the seat so that the culet is in the centre of the aperture hole. Screws hold the backing plate in place laterally as the diamond is clamped in place from above, the screws are then adjusted while looking down the barrel of the jig until the culet is centered. Once the anvil is aligned on the backing plate it is glued in place using the epoxy Stycast®, which is a specially designed adhesive that works down to very low temperatures without weakening or becoming brittle. When applying the glue the diamond must be clamped tightly enough to prevent the adhesive flowing between the diamond and the seat. Both anvils to be used in the cell are mounted in the same way.

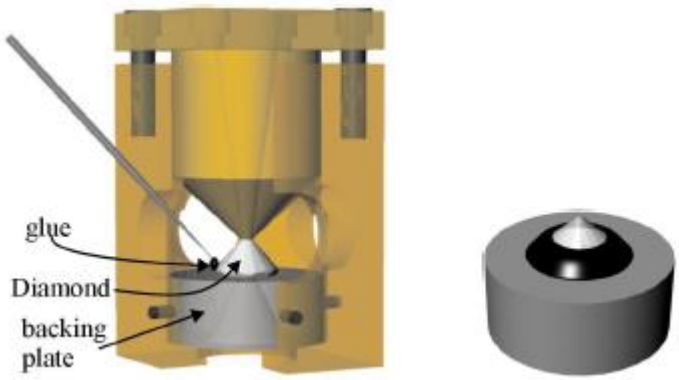

Figure 25. Diagram of a jig used for mounting diamonds (left). A backing plate with diamond attached, note the Stycast® glue sets black (right).

2.5.2 Alignment of the anvils

After the diamond anvils have been attached to the backing plates the plates are then fixed in the cell so that the culets can be aligned with one another. The alignment process for diamond anvils has been discussed in detail previously[60-

[62]. First the anvils are aligned in the *x-y* plane so that they face each other perfectly. This alignment is again performed by adjusting the position of lateral screws holding one of the backing plates in place. It is very important that the culets are completely parallel to each other, otherwise when a force is applied to the cell there will be a danger of anvil failure. The tilt alignment is checked by viewing the anvils from the side under the microscope and bringing them very close together. The tilt angle of one of the anvils may be adjusted as its backing plate is affixed to a hemispherical stage, the position of which can be changed by moving one of three screws at a time to change the tilt angle of one culet relative to the other.

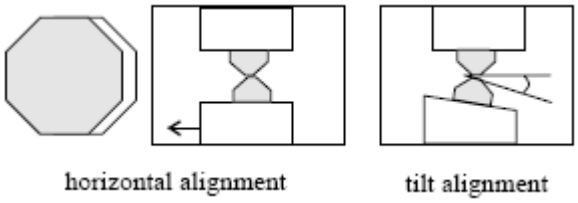

Figure 26. Schematic diagram demonstrating anvil alignment.

The parallelism of the culets is finally checked by using silver iodide (AgI). A small amount of bright yellow (under ambient conditions) AgI powder is placed between the culets of the diamonds, the cell is closed and a slight pressure applied. A phase change which causes a black spot in the sample to emanate from the centre of the pressure generation and can be observed at a modest pressure of about 3 kilobars at ambient temperature; further pressurisation leads to a very bright yellow phase which can be seen in the centre of the black ring (figure 27)[63-64]. This shows that there is a pressure gradient across the anvil face between the culets under these low pressure conditions. These changes can be accessed simply by pressing gently on the piston with fingers, if the black

circle is not directly in the centre of the culet then the tilt alignment needs to be adjusted. This process is repeated until the culets are completely parallel. Inadequate lateral or tilt alignment in a diamond cell may be a cause of catastrophic anvil failure which is demonstrated in figure 28.

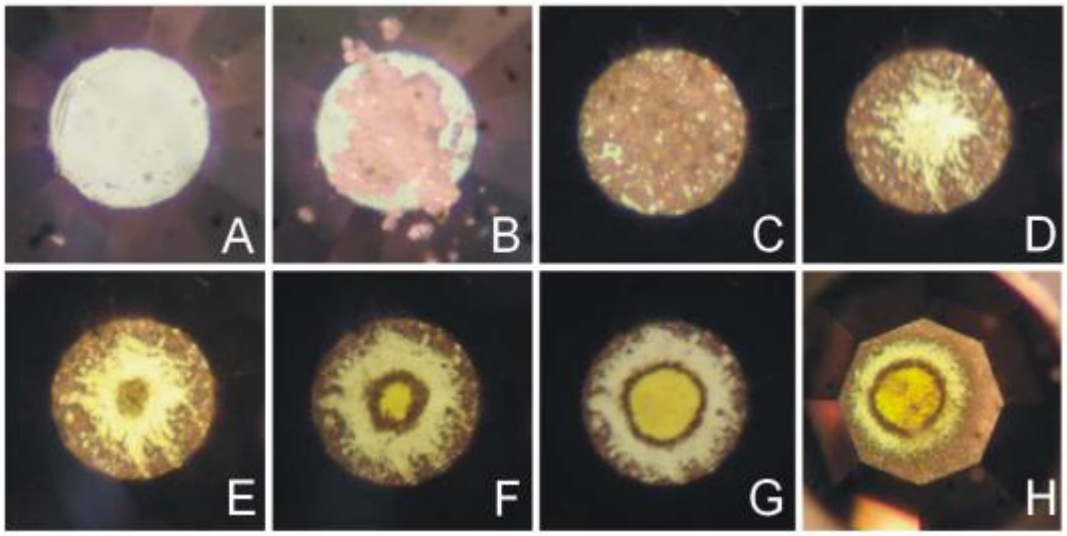

Figure 27. Steps in the anvil alignment process using AgI. A; bottom culet pre-alignment. B; place a small amount of AgI on the surface. C; close cell with upper diamond on top, no pressure applied. D, E, F,G; apply slight increasing pressure and the evolution of the phase change shows the position of the pressure in the culets. H; example of a cell where the culets are not parallel to one another, the black ring does not reside in the centre of the culet.

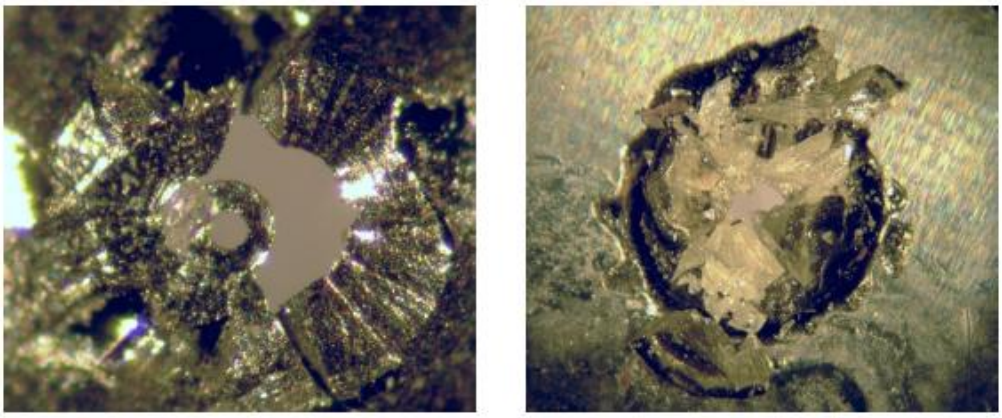

Figure 28. Damage caused to the gasket (left) and the diamond anvil (right) when anvil failure occurs.

2.5.3 Preparation of the Gasket

Diamond is the hardest known natural material. If the anvils were allowed to come together and touch with any force applied the diamonds would be damaged beyond repair. To prevent this happening a gasket made from a thin metal foil with a small hole made in the centre as a sample chamber is placed between the two anvils to stop them from coming into direct contact. It also has the advantage of containing the sample while the cell is under pressure to stop sample material squeezing out the sides. The gaskets prepared in this work were made from either stainless steel or rhenium, the latter being employed in experiments where the target pressure is above 40 GPa.

A small piece of the metal foil of about 200 μm thickness is cut to size and pre-indented so that the area under the culets ends up about 30-50 μm thick. This is done by putting the gasket in place, closing the cell and applying a pressure of about 20 GPa (this general rule of thumb works to get a 30-50 μm thick gasket). The gasket is marked beforehand so that it can be lined up with the cell and always replaced back in the correct orientation as the experiment is being prepared. The pre-indentation is important as this prevents the gasket material 'flowing' away from the pressurised area during experiment, making the gasket thin and more likely that the culet edge may pierce the gasket and cause anvil failure. This is also the reason why the gasket material must be strong enough to withstand the target pressure of the experiment.

After pre-indentation a hole is made in the centre of the indent with a spark erosion drill[65-68], this hole serves as the sample chamber and to contain the sample under pressure. The size of the hole is generally between 1/3 and 2/3 of the diameter of the culet. The drill is aligned in the centre of the indent under

a microscope to ensure that the hole is perfectly central to prevent any deformation or movement of the hole size and shape under load.

2.5.4 Loading the Sample and Pressure Medium

After the anvils have been selected, glued, aligned and the gasket prepared and put in place the sample must be loaded into the cell. Under a microscope solid samples are carefully located in the gasket hole with a needle or thin wire.

The DAC provides the force to the sample chamber in a uniaxial direction, therefore if the sample environment is to be truly hydrostatic the sample must be completely surrounded by a fluid medium. For samples (and pressure transmitting media) that are of a liquid or gas form under ambient conditions direct loading or cryogenic condensation methods can be used to load them. Where samples are solid a fluid pressure transmitting medium can be used to create a hydrostatic environment for the sample. Liquefied inert gasses such as nitrogen or argon are commonly used as pressure media in diamond anvil cell experiments, these can be loaded relatively easily in the lab. Cryogenic loading of nitrogen can be effected by closing the cell but leaving a slight gap of a few microns. The cell is then placed in a polystyrene container containing a small depth of liquid nitrogen. Once the cell has been allowed to cool down sufficiently the liquid level is topped up and the medium is allowed to condense into the sample chamber. The cell is closed *in situ* using long handled allen keys and the cell removed and allowed to warm up. The medium is now trapped under pressure and the nitrogen remains fluid only up to 2.4 GPa at ambient temperature, but may still provide a relatively hydrostatic environment up to ~30 GPa[69].

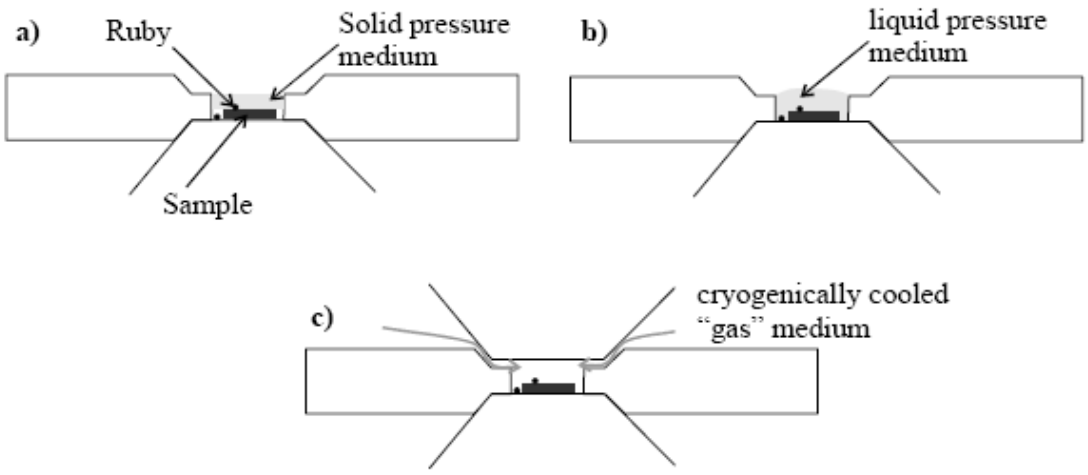

Figure 29. Pressure media loading for diamond anvil cell experiments; a) a solid medium, b) liquid medium, c) cryogenically loaded gas medium.

All samples used in the diamond anvil cell in this work were in the form of loose powders which can cause problems when it comes to deciding on the kind of medium to be used for the experiment[50]. Using a fluid pressure transmitting medium is one possibility however liquid nitrogen and argon tend to crystallise at relatively low pressures and they can cause a diffraction pattern that masks and overpowers the more weakly scattering carbon nitride materials when the samples are studied using synchrotron radiation. Several experiments using liquid nitrogen as a pressure transmitting medium were attempted but it was found that this method reduced the sample density so much that it was not possible to see the sample in the synchrotron X-ray diffraction pattern.

Other fluids such as a 4:1 ratio of methanol: ethanol can be useful for some experiments but this medium solidifies and becomes non-hydrostatic above 10 GPa. Also the alcohol mixture could react with the graphitic carbon nitride materials studied here. Therefore most experiments performed in this work were carried out without any pressure medium. The powders were instead compacted as much as possible prior to and during loading to fill the entire

space of the sample chamber. This also ensures a good sample thickness and density in the cell which is especially important for X-ray diffraction studies of such weakly scattering materials.

2.5.5 Pressure Determination

The main techniques for measuring the pressure in a diamond anvil cell are spectroscopically or by using X-ray diffraction. In this work the ruby fluorescence scale was used to determine all pressures and this will be discussed in more detail. The ruby fluorescence method was pioneered by workers at the NBS in the early 1970s[56,70] and has since become the standard method of pressure determination for diamond anvil experiments. It measures the movement of the R_1 and R_2 fluorescence lines of the Cr^{3+} ion in ruby (Al_2O_3:Cr^{3+}) on pressurisation. The scale was subsequently calibrated several times and is now a very accurate tool for the determination of pressure during experiment[71-72]. At high temperatures the ruby lines become very broad therefore the method is not suitable for use at elevated temperatures. Equation (4) below shows the relationship between pressure and the shift in wavelength of the R_1 ruby fluorescence line at room temperature;

$$P = \frac{1904}{B}\left[\left(1 + \frac{\delta\lambda}{694.24}\right)^{B} - 1\right] \quad (4)$$

where P is in GPa and $\delta\lambda$ is the ruby R_1 wavelength shift in nm. Parameter *B* is equal to 7.665 for quasi-hydrostatic conditions and equal to 5 for non-hydrostatic conditions[73]. The width of the ruby fluorescence lines does not change as pressure is increased. However, the energy difference between the R_1

and R_2 ruby lines may change on pressurisation, this is an indication that the environment of the ruby is non-hydrostatic (see figure 30). In a very non-hydrostatic environment it may not be possible to resolve between the R_1 and R_2 lines and just one broad peak will be observed.

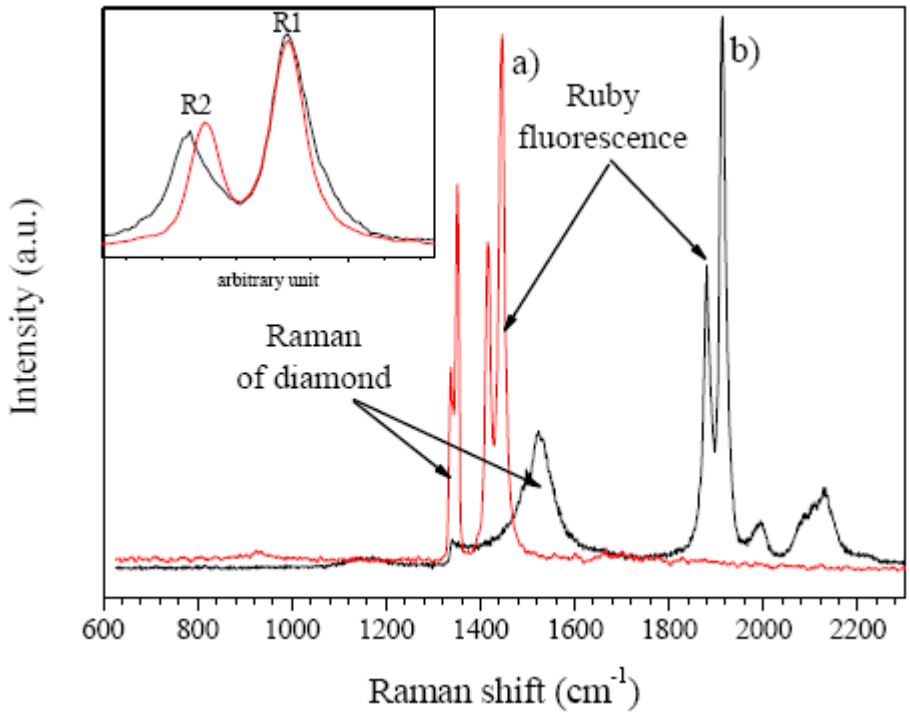

Figure 30. Ruby fluorescence spectra using a λ = 633 nm HeNe laser. a) is at 6 GPa and b) at 80 GPa. The insert shows the R_1 and R_2 lines of both spectra overlaid to demonstrate the change in difference in energy between them.

2.6 Analytical Techniques

2.6.1 X-ray Diffraction

Laboratory X-rays were used to some extent in this work to help characterise and compare experimental samples synthesised. These laboratory based techniques work well for sample sizes of several milligrams, which is the typical yield of material produced from the kinds of piston-cylinder synthesis experiments already discussed. However, when it comes to working with diamond anvil cells the intensity of the X-rays available from the laboratory diffractometer equipment is too low to be able to cope with both the very small sample volume (typically less than 8 x 10^{-5} cm^3) and penetrate the diamond windows in the cell. It is therefore important to be able to use a much brighter source of X-rays for diffraction using the diamond anvil cell; this is available in the form of synchrotron radiation but it requires the use of a specialised facility; this will be explained in more detail later. Synchrotron X-ray sources have a much higher flux of X-rays than those used in lab-based experiments and it can significantly cut the exposure time required from upwards of 24 hours down to as little as a few minutes depending on the material being studied.

2.6.2 Principles of X-ray diffraction

X-rays are short wavelength, high energy electromagnetic radiation; they have wavelengths ranging from about 10 to 0.1 nm, close to the inter-planar spacing of most crystalline materials. X-rays range from an energy of 200eV to 1MeV on the electromagnetic spectrum. Diffraction occurs as the wavelength of X-rays is on the order of the inter-atomic spacing in crystalline materials, materials then act as a diffraction grating for X-rays and the detection of the diffracted radiation can be used to gain information about the spacing between atoms in the

crystal[74]. When a monochromatic beam of X-rays is incident on a crystal with a set inter-atomic distance then the beam is diffracted in a specific direction according to Bragg's equation (5), which can then be used to determine these distances and crystal symmetry.

$$n\lambda = 2d \sin\theta \tag{5}$$

Here λ is the wavelength of the incident beam, *d* is the inter-planar distance and θ is the angle between the incident beam and the atomic planes.

Below in figure 31 this relation is shown schematically. The incident beam, on the left is diffracted by the material and the diffracted radiation is shown exiting on the right.

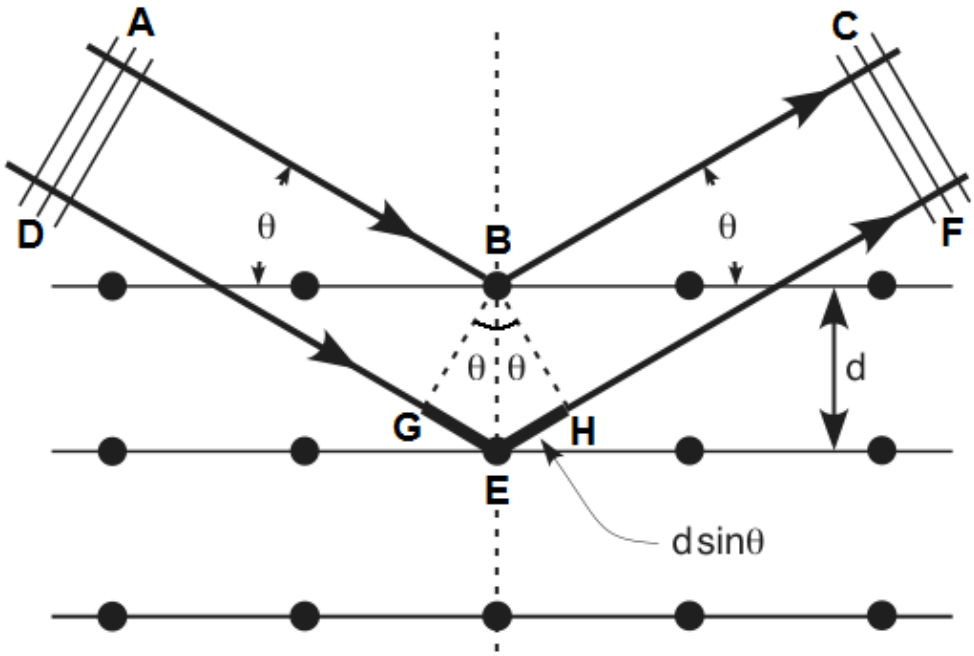

Figure 31. Schematic demonstration of the Bragg equation.

BG and BH are perpendicular to AB and BC respectively, therefore AB = DG and BC = HF. To ensure that the waves are in phase (i.e produce constructive

interference) GE and EH must be equal to $n\lambda$. A Bragg reflection will only be observed if the diffracted beams interfere constructively. Using trigonometry it can be found that GE is equal to $d \sin \theta$ (as is EH), so GH + EH = $2d \sin \theta = n\lambda$.

2.6.3 Generation of X-rays

For the generation of X-rays in the laboratory a vacuum tube is used containing an anode and cathode, as shown in figure 32. Electrons are emitted from the tungsten filament cathode by heating it to a high temperature using typically 20-40 milliamps of current. The electrons are accelerated through the vacuum tube towards the anode which is made of a pure metal (copper in the case of the experiments carried out here) which is usually at ground potential. The anode is cooled by water flowing past it to keep the operating temperature stable and stop overheating. The very high velocity electrons collide with the metal anode target and the electrons lose energy when they impact on the target. As energy must be conserved the energy loss is manifested with the production of X-rays. The end of the X-ray tube will contain a window that is transparent to X-rays (usually beryllium) so the radiation can leave the tube and be directed onto the sample.

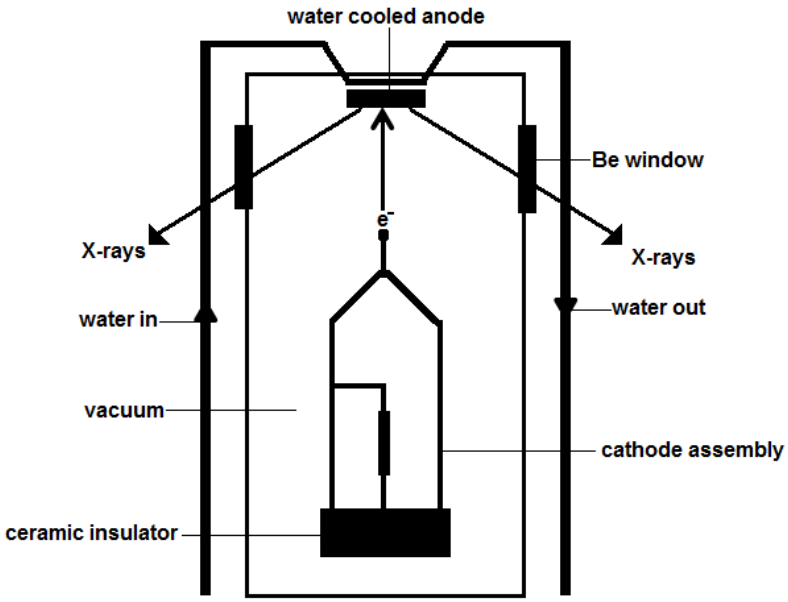

Figure 32. Schematic diagram of an X-ray tube.

2.6.4 Angular Dispersive X-ray diffraction (ADXRD)

All samples that were studied in this work were in the form of polycrystalline powders. Therefore rather than a distinct spot for each *d* spacing appearing in the diffraction pattern there is a circular array of spots, that appear in the form of a ring at each 2θ angle corresponding to the spacings in the material under study. This is represented in figure 33. This kind of experiment is called angle dispersive X-ray diffraction (ADXRD). A monochromatic X-ray beam is incident on a sample and the scattered diffraction rings are collected on a detector. The image can be integrated across the rings and a diffraction pattern of peaks at specific 2θ values is generated. The *d*-spacing of these peaks can then be found using the Bragg equation (5).

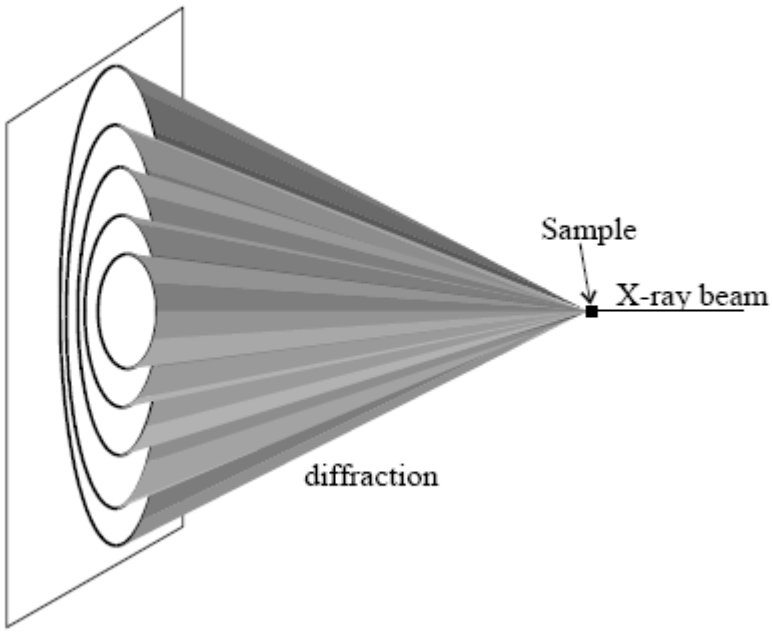

Figure 33. Representation of the diffraction that occurs with angular dispersive X-ray diffraction experiments.

Angular dispersive X-ray diffraction requires a source of monochromatic radiation (with wavelengths confined to an extremely narrow range). For 'ideal' polycrystalline samples where all the possible orientations of the crystallites are equally present in the sample then the diffracted radiation is scattered symmetrically out from the sample in the form of a cone that will be seen on the detector as the concentric circles of Debye-Scherrer rings as represented in figure 33. X-rays produced in a synchrotron are not monochromatic, therefore it is necessary to 'filter' the X-ray beam in some way to remove the unwanted portion of the radiation prior to its incidence on the sample using a monochromator. For example a single crystal cleaved at a particular plane, the incoming white beam hits the crystal at such an angle and displaces the beam such that the energy of the exiting beam is tuned. The angle between the crystal and the incoming beam determines energy of the exiting radiation and therefore

the properties of the outgoing beam can be tuned by changing the angle of the crystal.

ADXRD was used primarily in this project for the high-pressure study of materials in the diamond anvil cell. However, it is also possible to use energy dispersive X-ray diffraction in such experiments and some of the work here is compared with similar experiments undertaken with EDXRD, so it will be briefly explained below. Experiments that were attempted in the multi anvil on station 16.4 at the SRS were conducted using EDXRD.

2.6.5 Energy Dispersive X-ray Diffraction (EDXRD)

In energy dispersive diffraction a white beam (polychromatic, a range of different wavelengths are present) of radiation is used. The 2θ diffraction angle is fixed and a solid state detector records the number of photons as a function of energy that hit it. Such detectors will produce a diffraction pattern as an energy spectrum. So the *d*-spacing is a function of energy for a given angle. By combining Bragg's equation (5) with Planck's equation (6) a relation of *d*-spacing to energy can be given.

$$E = \frac{hc}{\lambda} \tag{6}$$

Planck's equation; E is the energy, c the speed of light, λ the wavelength of the radiation and h is Planck's proportionality constant which is equal to 6.63×10^{-34} $J.s$.

So,

$$d = \frac{hc}{2E \sin\theta} \tag{7}$$

The size of the fixed 2θ angle used for EDXRD depends on the size of the lattice being studied. Smaller angles are better for studying systems with larger *d*-spacings.

2.6.6 Synchrotron Radiation

For the diffraction experiments performed at high pressure in the diamond anvil cell it was necessary to use a very high energy source of X-rays to overcome the attenuation of the radiation through the diamond windows. Synchrotron radiation is the X-ray radiation generated when a beam of charged particles travelling at velocities close to the speed of light, electrons, in the case of the facility used for this work, are accelerated through a magnetic field along a curved trajectory, i.e. the path of the particles is curved by the magnet and this causes electromagnetic radiation to be emitted. A large component of the radiation produced consists of high energy X-rays, along with radio waves, infra-red light, visible light and ultraviolet light. The source of the synchrotron radiation is the storage ring, which is essentially a circular loop under ultra high vacuum conditions surrounded with large magnets to constantly bend the path of the electrons passing through them. A cathode ray gun is used to produce electrons and the electrons are accelerated to very high speeds using a linear accelerator and booster ring to finally reach an energy which is in the range of several GeV. The high speed electrons are stored in a closed ring under ultrahigh vacuum, the electrons are guided in their (approximately) circular path by large

magnetic fields applied by ‘bending magnets’. The particles would naturally only travel in straight lines, however, the bending magnets are used to curve the trajectory of the electrons into a ring. The change in direction caused by the magnets is a form of acceleration and this causes the electrons to emit synchrotron radiation. The synchrotron radiation produced propagates in the same direction as the incoming beam of electrons, which is at a tangent to the ring. This radiation can then be harnessed for experimental use by beamlines situated around the perimeter of the ring. (Figure 34).

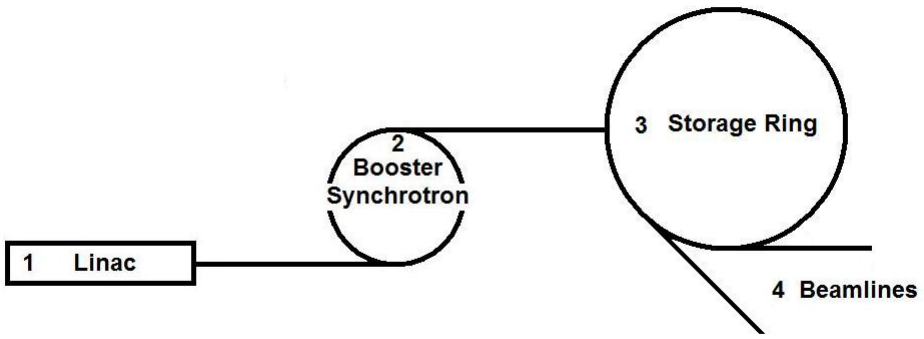

Figure 34. Schematic illustration of a synchrotron showing the 1. the linear accelerator (linac) where the electrons are produced and accelerated, 2. the booster ring where the electrons are finally accelerated to 2 GeV, 3. the storage ring and 4. the beamlines around the outside where the experimental use of the X-rays is undertaken .

Modern synchrotron sources often also use other magnetic devices to enhance the energy and/or wavelength of the radiation produced, these are known as insertion devices. The insertion devices consist of an array of magnets arranged with opposing N and S poles. These alternating magnetic fields cause the electron beam to undulate as it travels past and on each oscillation synchrotron radiation is emitted, all of these emissions add up to give an X-ray beam with its

brilliance multiplied by several orders of magnitude. Wigglers also have the capability of shifting the X-ray range produced to higher energies.

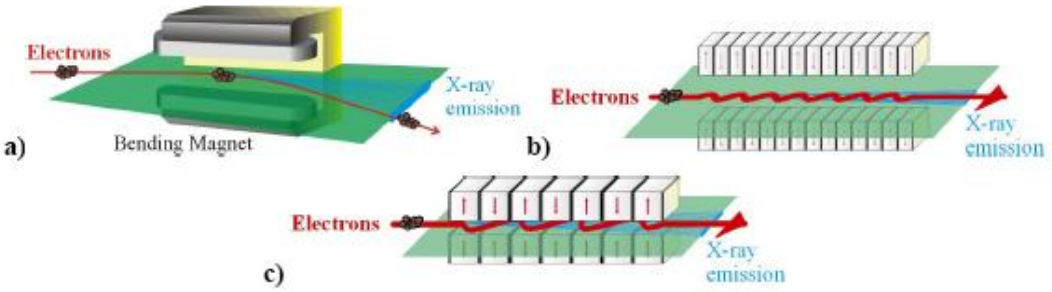

Figure 35. Schematic illustration of a) a bending magnet b) an undulator and c) a wiggler.

2.6.7 Daresbury Synchrotron Radiation Source and Station 9.5 HPT

The Synchrotron Radiation Source (SRS) at Daresbury, UK, is a 2 GeV second generation facility and is where all the experiments discussed in this thesis were performed. This facility was one of the world's first sources used for scientific applications of synchrotron radiation and one of the premier facilities with users coming from all over the world to make use of the various stations and techniques available. However Daresbury SRS is now closed (as of late 2008) and has been superseded by more powerful third generation synchrotrons such as the UKs new Diamond facility in Oxfordshire[75]. All of the work carried out in this thesis used the Daresbury SRS facility: the Diamond synchrotron was not opened in time to contribute to the work reported here.

2.6.8 Specifics of High Pressure Diffraction in the DAC at 9.5HPT

All the high pressure X-ray diffraction experiments using the diamond anvil cell in this project were performed at the Synchrotron Radiation Source (SRS) in Daresbury, UK on station 9.5HPT (HPT standing for high pressure, temperature). SRS station 9.5HPT is a beamline specially adapted for high-

pressure diffraction using diamond anvil cells. The station provides a focussed monochromatic x-ray beam with a wavelength of about 0.5Å. It has a Laue monochromator which collimates an X-ray beam of approximately 30 keV and focuses it down to about 30 μm^2 when it hits the surface of the anvil window in the DAC. White beam X-rays are taken in to the station and a silicon crystal cleaved on the 110 plane is used as a monochromator. Two types of detectors have been used for data collection for the experiments on this project. The first is an image plate which is exposed to the diffracted X-rays thoughout the experiment and then scanned using a Molecular Dynamics 'Storm' scanner to produce .gel image files. For later experiments an on-line mar345 image plate detector was used which automatically scans, records and saves the images electronically during the experiments. Image plate data collection techniques are good for weakly scattering samples such as those studied in this work as they cope well with the long exposure times required. Images plates with online scanners have excellent spatial distortion correction and reproducibility. Those that use separate offline scanners can show non-reproducibility in the reading of the image. However, with modern scanners this problem is less apparent and the equipment available at the Daresbury SRS is particularly accurate for this kind of work and gives a very good correction when coupled with good data processing software[76].

Due to the very weakly scattering nature of the samples under study the exposure time of the high pressure diamond anvil experiments were typically 4-6 hours in duration. This made data collection very difficult at times as the experimental time available at the synchrotron facility was limited. This coupled with the fact that visits to the facility were usually limited to 2-3 times a year for

about 3-4 days each for the entire experimental programme within our research group, combined with the sometimes unreliable nature of the beam during many of these visits (especially towards the end of the synchrotron lifetime), and the tendency for diamond anvil cell loadings to fail on occasion, means that the data presented here were gathered and collated from runs carried out during several visits spanning three years. Due to these factors it was therefore not always possible to obtain the full range of data desired or to take and subtract full background readings for every run.

2.6.9 Data Processing

The data collected from angle dispersive X-ray diffraction experiments in the DAC take the form of a 2D image of the Laue diffraction rings on the image plate detector, an example of which can be seen in figure 36. An electronic image of this data is generated either by scanning the image plate or by using an online scanning image plate detector. To be able to use and manipulate data to gain useful information about the structure of the material under study it is necessary to process this raw data in some way.

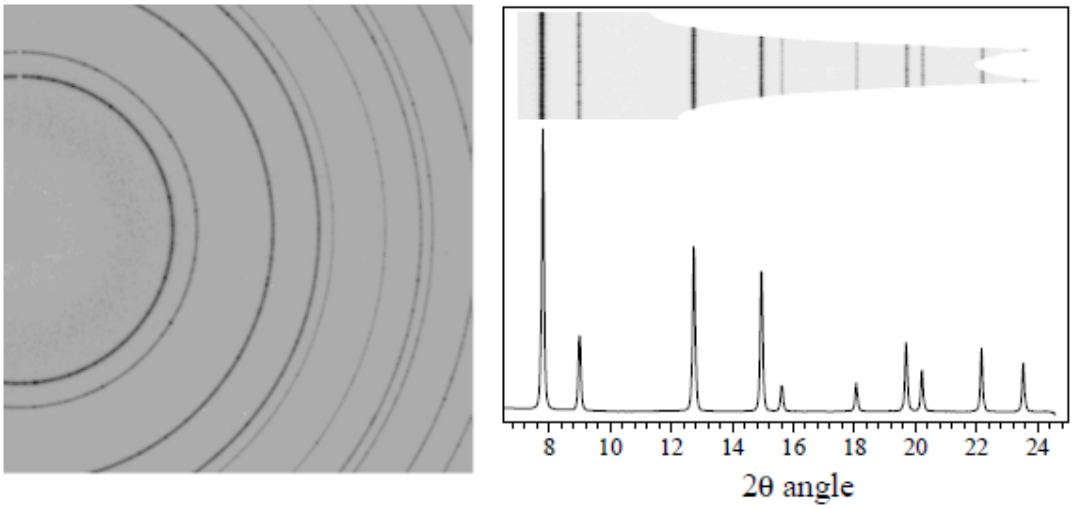

Figure 36. 2D diffraction image of silicon is shown on the left. On the right the 2D to 1D integration process is demonstrated.

High pressure diffraction data obtained in this work was processed using the program Fit2D[77]. The calibrations for the data were performed using a silicon standard.

The diffraction pattern of the calibrant is used to accurately determine the sample detector distance which is essential for the calculation of accurate 2θ and *d*-spacing values when the pattern is integrated. It is also necessary to correct for any distortion in the geometry of the detector. The software can then be used to integrate across the 2-dimensional image to give a 1-dimensional diffraction spectrum.

2.7 Infrared Spectroscopy

Infrared spectroscopy utilises the infrared region of the electromagnetic spectrum which comprises of radiation with frequencies between roughly 750 nm and 1 mm. This can then further sub-divided to the far-, mid- and near-infrared. The mid-infrared is the region that was used to investigate the materials studied in this work which covers the 2.5-10 μm wavelength range i.e. 400-4000

cm^{-1} (wavenumbers). IR spectroscopy provides information about the bonding in molecules by probing the vibrations between its constituent atoms. During IR absorption a photon of IR radiation is absorbed by a molecule and it is then promoted to a higher vibrational state, for the absorption to be able to happen the energy of the photon must match the separation between vibrational states in the molecule being studied. An infrared spectrum displays these absorptions so that information about the vibrations, and consequently the atoms involved in these vibrations can be deduced, in turn revealing structural information about the material under study.

2.7.1 Specifics of High Pressure Infrared Spectroscopy in the DAC

The study of materials under high pressure using IR spectroscopy provides several challenges to overcome. The extremely small sample volumes involved and the fact that the diamonds absorb IR radiation[60] need to be considered.

When preparing an infrared DAC experiment it is important to select diamonds that have maximum transparency in the infrared region. For mid-IR studies it is necessary to choose a pair of type IIa anvils that have a very low absorption in the 1200 cm^{-1} region. All diamonds show strong absorption in the 1800-2500 cm^{-1} region due to overtones of the fundamental vibrational modes rendered infrared active by anharmonicity. However, depending on the diamond purity and mainly the level of nitrogen impurities and their state of aggregation inside the diamond lattice the rest of the IR spectrum can be available for study. In order to undertake successful infra-red spectroscopy through the diamond anvil cell it is necessary to use nitrogen ‘free’ diamonds of the type IIa variety. Good IR diamonds must have a very low nitrogen content and the only way to check

this is to test a candidate stone using IR spectroscopy. Diamond can display IR bands in the 1000-1500 cm^{-1} region which are characteristic for nitrogen. Figure 37 shows two IR spectra that correspond to a) 'nitrogen free' diamond and b) a more nitrogen rich diamond. Strong peaks can be seen at ca. 1100 and 1300cm^{-1} in the nitrogen rich specimen that are not present in the nitrogen free material. Therefore specimen a) is suitable for IR spectroscopy in the diamond anvil cell and specimen b) is not, the bands between 1000-1500cm^{-1} would interfere with the sample signal too much.

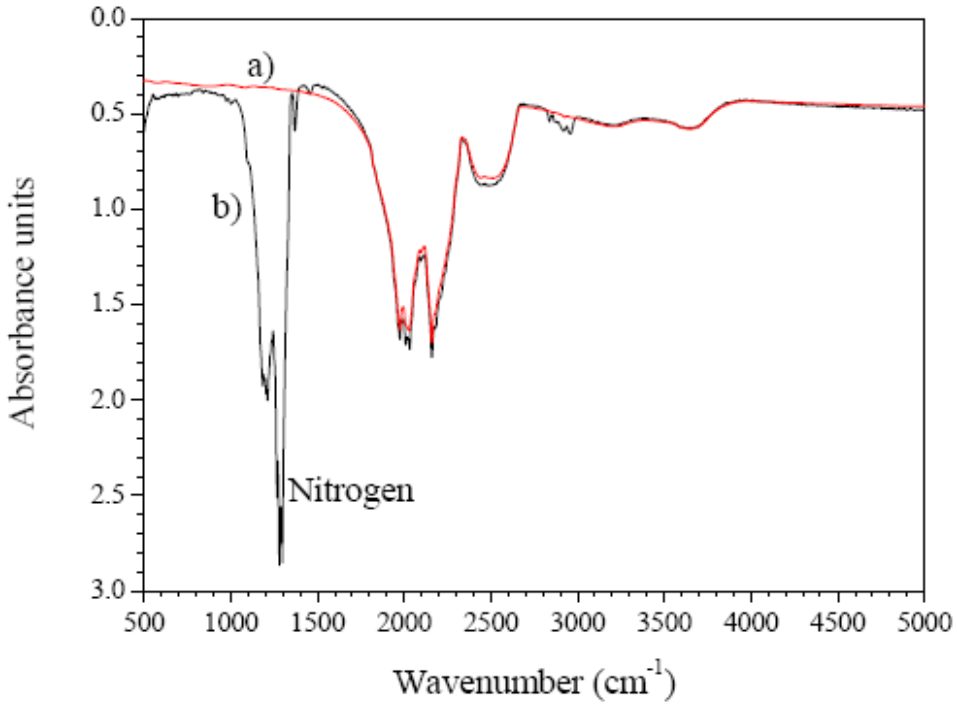

Figure 37. IR absorption spectrum of 2 diamond specimens, a) is a 'nitrogen free' stone and b) a 'nitrogen rich' one showing strong absorbance features in the 100-1400cm^{-1} region.

Another consideration is the high refractive index (n = 2.4) of diamond which can affect the optical path length and cause the IR beam to become unfocused through the sample, affecting both the resolution and intensity of the resulting spectra.

Anvils with larger culets are the best choice for IR spectroscopy in the DAC. This is because it allows for a larger gasket hole and therefore helps reduce interference effects that can occur because of the long wavelength of IR radiation, these interference effects can be observed in the high pressure IR spectra presented later. However, the size of the culet used will have an impact on the maximum pressure available for the experiment. The anvils available for the experiments in this work were pairs of type IIa diamonds with 800 μm culets.

When loading cells for IR experiments it is usually (more so than in the case of X-ray diffraction) necessary to use a pressure transmitting medium. This acts not only to help give a hydrostatic sample environment but also to dilute the sample and aid transmission of the radiation as IR is much less penetrating than X-rays. When choosing a medium for such an experiment soft materials that are transparent to IR are usually considered. For this work KBr was used as the medium. The pressure measurement used for the IR experiments in this work was obtained by the ruby fluorescence method, as for the X-ray diffraction experiments.

The measurements taken during this work were taken using a Bruker IFS 66v/S FTIR spectrometer, the spectra taken from within the diamond anvil cell were measured using an IR microscope attachment; IRscope II also made by Bruker optics, Germany. The microscope allows IR transmission and reflectance measurements through the DAC. The detector in this IRscope is a liquid nitrogen cooled mercury cadmium telluride (MCT) solid state detector and the IR source is a water cooled silicon carbide glow bar. Dry air is continuously

purged through the system to remove water vapour and where possible all experiments are conducted in a vacuum to remove all background species.

Figure 38. The Bruker IFS 66v/S FTIR spectrometer with IRscope II infrared microscope used to take the IR spectra.

2.8 Raman Spectroscopy

The Raman effect was first observed by C.V Raman[78], G. Landsberg and L. Mandelstam[79]. The effect arises when light incident on a molecule interacts with the electron cloud of that molecule in such a way to cause vibrational excitations. Any visible light passing through a sample will be elastically scattered in all directions due to Rayleigh scattering, and this gives rise to the intense central Rayleigh line in the Raman spectrum. However, a very small portion of the scattered light will have gained or lost energy compared to the incident beam[80-81]. When a beam of monochromatic light is passed though a sample a small amount of the light is inelastically scattered. The electron cloud

of a molecule is disturbed by the incoming photon, this causes the nuclei within the cloud to move also. If this movement corresponds to an allowed vibrational mode for the molecule then this will cause the energy of the incident photon to be changed and the transition will be observed in the Raman spectrum. The incoming photon will momentarily deform the electron cloud of the molecule during the collision, the nuclei will then be displaced about their equilibrium positions as they move to follow the new, deformed electron distribution. In the majority of collisions the photon leaves, the nuclei return to their equilibrium positions, resulting in an elastic collision. If the motions induced in the nuclei correspond to their displacements during a normal vibrational mode then that vibration is stimulated and the energy of the vibration will be removed from the photon to give Stokes Raman scattering. The reverse process gives rise to anti-Stokes scattering, if the molecule is initially in an excited state and the interaction with the photon results in transition to a lower vibrational state then the photon will have gained energy on re-emission.

The energy of the incident radiation, E_o, is related to its frequency as follows, $E_o = h\nu_o$, where h is Planck's constant. When photons collide with molecules elastically their energy is usually unchanged. In some collisions it may be that there is an energy exchange between the photon and the molecule, these are termed inelastic collisions and during these collisions the molecule can gain or lose energy in the process. The change in energy, ΔE, of the in-elastically scattered photons is termed the Raman shift and is measured in wavenumbers (cm^{-1}) relative to the incident beam energy and corresponds to the energy difference between allowed vibrational states. If a molecule gains energy during a collision the photon will be scattered with a decrease in energy compared to

the incident beam, $h\nu_O - \Delta E$, and is called a Stokes shift. Photons scattered with an increase in energy, meaning the molecule has lost energy because it was already in a level higher than the ground state at the time of collision, the scattered frequency will be $\nu_O + \Delta E/h$ and this is an anti-Stokes shift. Therefore Raman shifts are equivalent to the energy changes involved in transitions of the sample and are characteristic of it. Also at normal temperatures the higher energy levels are less likely to be populated than lower ones. So Raman shifts with positive frequency (anti-Stokes) are less intense than those with a negative frequency (Stokes).

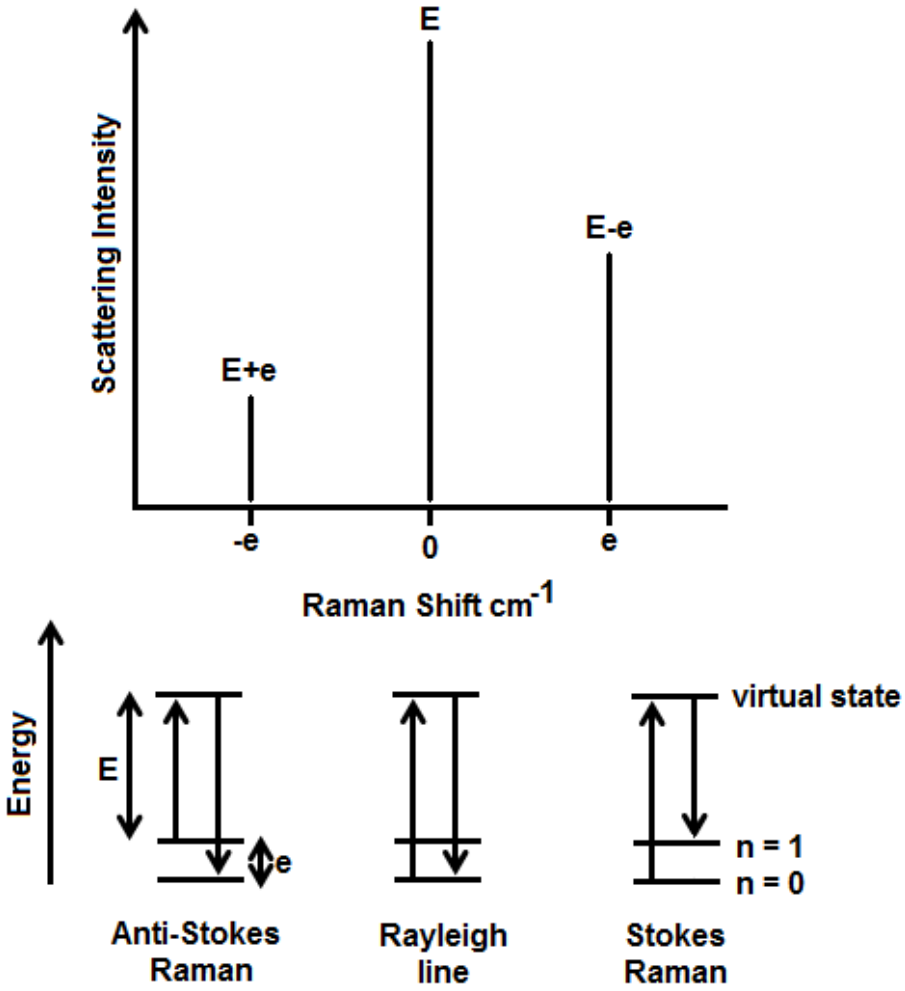

Figure 39. Schematic diagram of the Raman scattering process.

Figure 39 shows a schematic diagram of the Raman scattering process. The incident beam has energy E. The Rayleigh line is caused by the inelastic scattering of the incident beam resulting in the strong central peak at the incident frequency (zero Raman shift). Raman scattering is accompanied by a change in vibrational energy level to give peaks at E-e and E+e (Stokes and Anti-Stokes shift respectively) where e is the vibrational level separation. At ambient temperatures the ground state is more populated than higher vibrational levels hence the Stokes shift spectrum is more intense than the Anti-Stokes.

The observed Raman shifts correspond to vibrational or rotational transitions of the scattering molecule[80]. Not all vibrational transitions will be observable by Raman spectroscopy. For a transition to be observable in Raman spectroscopy it must cause a change in the polarisability in the electron cloud of the molecule. Therefore it may provide information that is complementary to, yet not provided by, other techniques such as infrared spectroscopy, in which the transition must involve a change in dipole moment of the species under study in order to be observed. This is due to the difference in the way that IR and Raman spectroscopy access the vibrational transitions. In Raman spectroscopy the incoming photon causes a momentary change in the electron distribution over a bond, quickly followed by a re-emission as the bond returns to its ground state. This causes a temporary polarisation of the bond, inducing a dipole in the bond that disappears upon emission. In centrosymmetric molecules a change in dipole occurs when the centre of symmetry is lost, a change in polarisability is compatible with the preservation of the centre of symmetry. Therefore in centrosymmetric molecules asymmetrical stretching and bending will be IR active and Raman inactive and symmetrical stretches will be Raman active and

IR inactive. So for centrosymmetric molecules IR and Raman activity of vibrational transitions are mutually exclusive. For non-centrosymmetric molecules vibrational modes may be Raman active, IR active, both or neither and there are other selection rules to determine this. Symmetric stretches and bends tend to be Raman active.

2.8.1 Fluorescence and Resonance

It is well known that molecular, oligomeric and solid-state aromatic systems including those based on C,N heterocycles exhibit strong fluorescence when excited by visible radiation due to π-π^* and other electronic transitions.

During the studies of the graphitic C_xN_y materials attempts were made to obtain Raman spectra with laser excitation throughout the visible and into the UV range (787-325 nm) using home-built and Renishaw micro-Raman systems at UCL. All of these experiments resulted in intense photoluminescence that obscured the Raman spectra (see figure 40). Previous studies of similar layered and nanocrystalline C_xN_y compounds have also reported intense photoluminescence when excited by visible radiation[5].

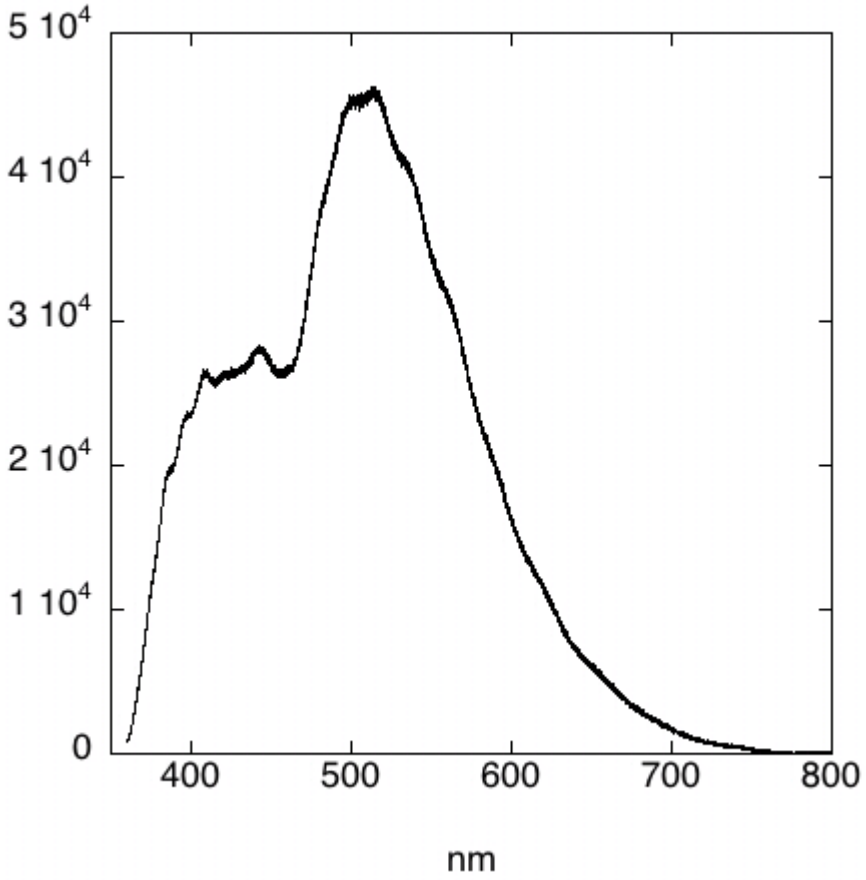

Figure 40. Typical room temperature photoluminescence spectrum of graphitic $C_6N_9H_3$.HCl produced *via* high-P,T synthesis from heterocyclic aromatic precursors excited using 325 nm laser excitation. Raman peaks appear as weak features on the high energy side of the main fluorescence peak, shifted by ~1000-1800 cm^{-1} from the exciting line.

Fluorescence and Raman scattering are related but quite different phenomena. Raman is a scattering process and fluorescence is a radiative process. Usually in Raman spectroscopy only a virtual state is achieved, and this has zero life time. So the process basically involves scattering the exciting beam, it goes in and then comes straight out. A shift in the wavelength of the radiation is observed if it has been affected by the molecule it was incident upon. In fluorescence the absorbed photon puts the molecule into an excited state, the incident exciting beam has actually induced an electronic transition in the species and this has a non-zero lifetime, which can vary from a few milliseconds

to perhaps minutes depending on the type of fluorescence. Therefore fluorescence is a radiative process following the absorption of a photon. The excited electronic state can either re-emit the photon at the same frequency as it was absorbed, or it can de-excite by making one or more transitions to electronic states that are of lower energy than the originally excited state but higher than the energy of the ground state. As the electron moves through the intermediate electronic states the molecule emits a photon of lower frequency corresponding to the difference in energy between the excited state and the intermediate state. This energy may be emitted as light if the frequency is in the visible region.

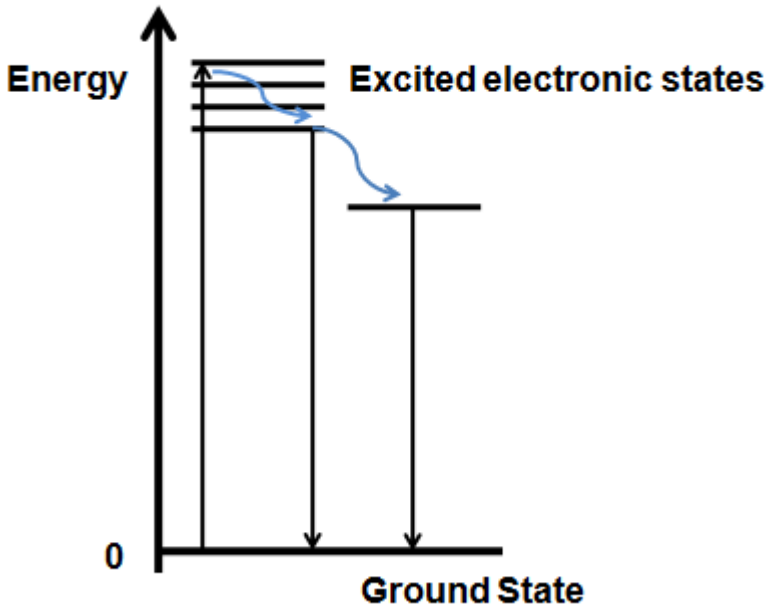

Figure 41. Diagram showing the process of fluorescence.

However, excitation with UV radiation above the range of most of the electronic transitions can result in useful Raman spectra. Here UV excitation was used to obtain Raman spectra for the $C_6N_9H_3$.HCl compound[82]. In collaboration with the Laboratoire des Sciences de la Terre at ENS Lyon, France. The solid state samples were excited with 244 nm radiation from a frequency-doubled Ar^+ laser

using a Jobin Yvon-Horiba LabRam UV Raman system installed at the facility in France. In these micro-beam experiments the incident laser was focused on the sample *via* a UV microscope objective and spectra obtained through the same objective in a back-scattering geometry. The sample area illuminated was 4-5 μm in diameter. During initial experiments we observed spectral changes that could be attributed to sample degradation during UV laser irradiation. In subsequent studies we reduced the laser power to a few mW incident on the sample and no longer observed any time-dependent changes in the spectra. In later experiments we also used facililtes at LEPMI-CMTC at INPG in Grenoble, France and additional measurements were carried using 229 nm laser excitation with the sample mounted on a rotating stage to confirm that no sample degradation had taken place. The spectrometer was a Jobin Yvon T64000 instrument equipped with an 1800 gr/mm grating. The results were identical to those obtained at ENS Lyon.

During UV excitation of graphitic materials with substantial sp^2 bonding and low-energy electronic excitations, the Raman spectra can exhibit significant resonant enhancement of vibrational contributions from structural species present in small concentrations[83-88]. Various graphitic, nanocrystalline and amorphous carbon and carbon nitride materials can also exhibit strong dispersion in Raman peak positions as a function of the excitation wavelength.

In further work Raman spectra of the samples were obtained using near-IR (1064 nm) excitation provided by a Nd^{3+}:YAG laser in a Fourier transform (FT) Raman experiment using a Bruker IFS88 spectrometer at the CRMHT-CNRS Orléans, France. For those experiments the sample was pressed into a

disc in an Al holder and spectra were taken on 100 μm spots. The instrumental resolution was 4 cm^{-1}.

Neither FT-Raman nor UV Raman experiments could be carried out in the diamond anvil cell.

2.8.2 Resonance Raman

The radiation used to excite molecules in Raman spectroscopy usually has a much higher energy than the vibrational motions, but may approach that of electronic transitions. In normal Raman scattering the wavelength of the incident radiation is usually chosen so as not to coincide with optical absorptions of the molecule as the resulting fluorescence or electronic effects may interfere or completely swamp the weak Raman signal. Resonance Raman spectroscopy involves using a tuneable laser so that the energy of the radiation incident upon the sample can be adjusted so that it or the scattered radiation coincides with an electronic transition in the sample molecule or crystal. If the frequency of the incoming laser is tuned to be near an electronic transition (resonance) in the target material the intensity of the Raman scattering associated with the transition will be increased greatly i.e. there is an enhancement in the Raman effect for the vibrational modes that are affected by the electronic excitation[89]. This can overpower the Raman signal from other transitions in the material. One disadvantage of resonance Raman is that the increased energy of the laser used to excite the material can cause photodegradation of the sample. This was the case for the materials studied here so extreme care had to be taken when setting the laser power for such experiments.

The resonance effect can also occur in normal Raman spectroscopy when the energy of the exciting laser is close to that of one of the electronic transitions of the molecule. This can cause certain Raman bands to appear dramatically more intense than they would in the absence of resonance enhancement. It can dwarf the other Raman peaks in a sample spectrum and result in the spectrum appearing very different than might be expected, or to the spectrum seen when using a different wavelength of laser excitation.

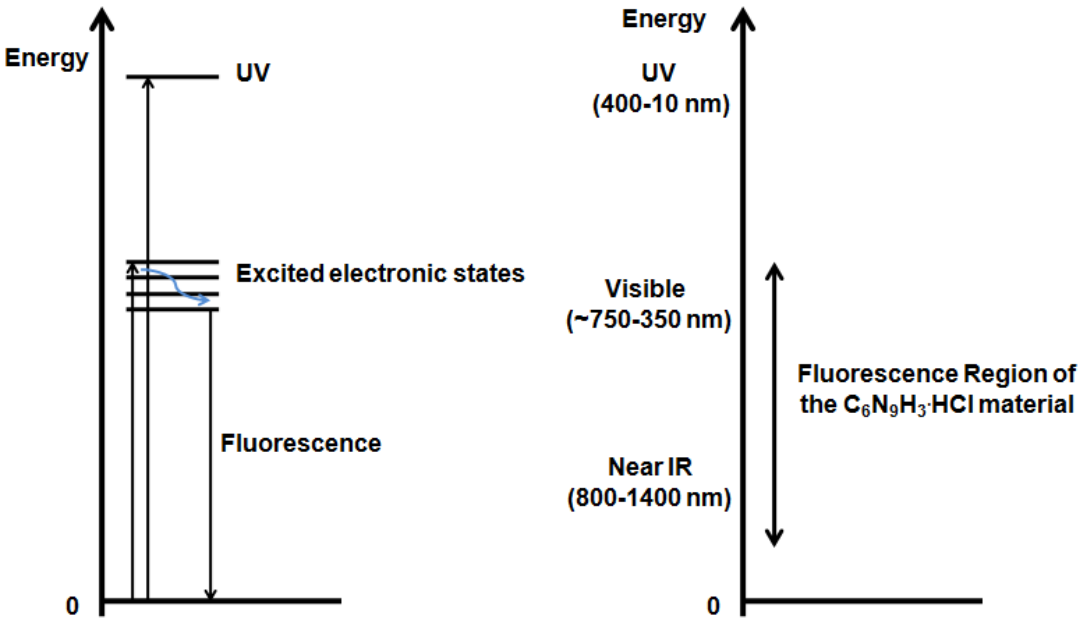

Figure 42. Diagram showing that when UV excitation is used for Raman spectroscopy of the $C_6N_9H_3 \cdot HCl$ material the higher energy of the incident beam excites the molecule past the region where fluorescence is observed.

Chapter Three – High Pressure-High Temperature Synthesis and Characterisation of Layered Graphitic Carbon Nitride Materials from Heterocyclic Aromatic Precursors

3.1 Introduction

The work described here represents a new approach to the preparation of graphitic carbon nitride materials. It combines solid state organic synthesis using heterocyclic aromatic precursors and unusual high-pressure, temperature techniques to synthesise the layered graphitic carbon nitride phases. The first syntheses of this type were reported previously by Demazeau, Montigaud and Alves.[7,22,90] Melamine and cyanuric chloride have been previously used with a nucleophilic amino base under moderate pressures and temperatures (130 MPa and 250 °C respectively) in an attempt to synthesise carbon nitride materials. However, only poorly crystalline samples were produced, with further analysis revealing that the samples were significantly contaminated with hydrogen and chlorine. Subsequent work resulted in a material that was more crystalline with a similar carbon/nitrogen ratio using higher pressures and temperatures (3 GPa and > 800 °C)[90] however it was not possible to index the diffraction pattern of this material to the previously proposed hexagonal graphitic models of C_3N_4 structures, rather an orthorhombic unit cell was proposed with an alternate graphite like structure involving a different ordering scheme for the carbon vacancies. The crystallinity of the material would need to be significantly improved to make a more reliable structural characterisation possible. Later Zhang et al.[8] reported a bulk synthesis of a better crystallised material

containing an alternating network of carbon and nitrogen atoms with a stoichiometry close to C_3N_4 which was investigated with NMR, FTIR, TEM/EELS and XRD. The material also contained some chlorine and hydrogen upon analysis and the stoichiometry was actually determined as $C_6N_9H_3{\cdot}HCl$. This was updated slightly by Wolf et. al.[45] with the synthesis conditions and higher pressure behaviour of the material being explored in more detail.

The experimental synthesis and characterisation of the materials produced have been compared with *ab initio* theory computational calculations performed in collaboration with M. Deifallah and F. Cora at UCL to gain further insights on the structure of the material and to suggest a new model for the N,H ordering within the layers.

3.2 Synthesis of $C_6N_9H_3.xHCl$

The high pressure high temperature syntheses of the carbon nitride materials were conducted in the piston cylinder apparatus, described in Chapter 2, following similar procedures to Zhang et. al[8]. The materials were synthesised using the precursors melamine ($C_3N_6H_6$) and cyanuric chloride ($C_3N_3Cl_3$) (figure 43), these starting compounds were obtained from Sigma-Aldrich and were used as received without further purification.

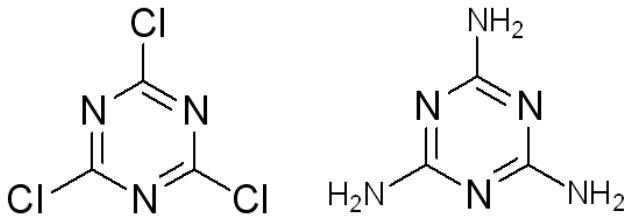

Figure 43. Molecular structures of the precursor materials; cyanuric chloride (left) and melamine (right).

Due to the high O_2/H_2O sensitivity of the starting materials they were stored, and all sample preparations/manipulations were undertaken, in a dry box under argon atmosphere. To achieve the synthesis we used a 1:2 molar ratio of melamine and cyanuric chloride. These are expected to combine according to the general reaction:

$$n C_3N_6H_6 + 2n C_3N_3Cl_3 \rightarrow 3n C_3N_4 + 6n HCl$$

As was found by Zhang et al [8], the material produced does not have the fully dense C_3N_4 graphitic structure originally predicted by Kouvetakis et al.[23] (figure 44).

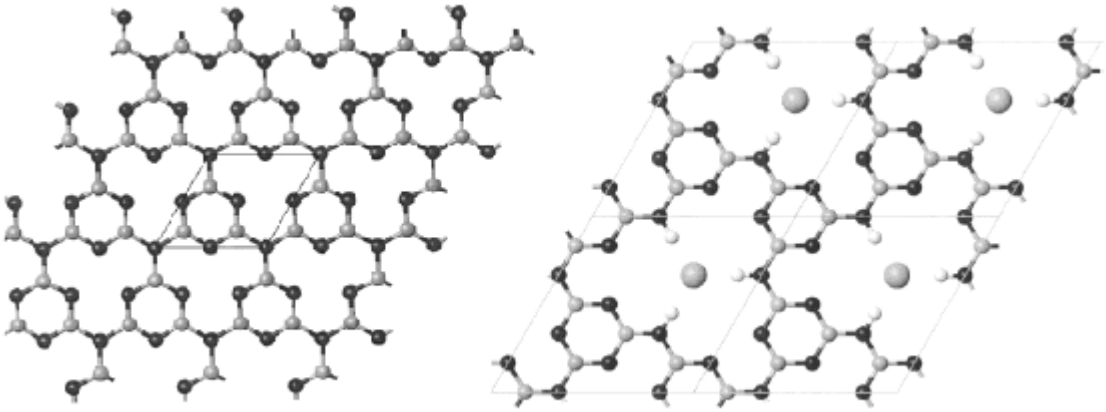

(a) **(b)**

Figure 44. a) 'Fully dense' graphitic C_3N_4 structure (left) b) the more open $C_6N_9H_3.xHCl$ graphene.

However, the synthesis results in a carbon nitride phase that is structurally related to the hypothetical C_3N_4 phase but with an HCl component remaining in the material that is derived from the starting materials. The actual composition of the product material of this synthesis, as elucidated by Zhang et al. is thought to be;

$$C_6N_9H_3.HCl$$

The structure of this material is proposed to be an open 'graphene' layered framework with two thirds of the triazine units missing compared to the fully dense C_3N_4 model structure as is shown in figure 44 b) which shows the structure proposed by Zhang et al. for the material. The parent $C_6N_9H_3$ framework is a layered planar network of $P6_3/m$ symmetry. The network consists of an alternating array of carbon and nitrogen atoms which results from the interconnection of triazine rings connected through imido groups, both of which can be easily related to the precursor materials. The large 24 atom voids

within the structure are occupied by a chloride ion and the charge compensating proton resides around the ring (not displayed in the figure).

3.2.1 Experimental Procedure

About 250 mg of the precursors are weighed out. 0.0641 g of melamine (5.08 x 10^{-4} mol) and 0.1875 g cyanuric chloride (1.02 x 10^{-3} mol) are mixed together and finely ground. This mixture is then pressed into a pellet of diameter 4.5 mm using a custom made pellet press and specially adapted vice inside the dry box. The pellet is then loaded into a platinum capsule with one end crimped and welded shut. Once the materials have been loaded the other end of the capsule is crimped shut tightly in a 'milk carton crimp' using modified needle nose pliers to form the finished sample capsule. The sample capsule is then placed into the furnace assembly which is then loaded into the piston cylinder apparatus as previously described. The samples are then taken up to about 1.5 GPa and 550 ˚C for a period of about 15 hours.

When the synthesis run is complete the experiment undergoes an isobaric quench i.e. the pressure is held approximately constant at the same value as throughout the experiment and the temperature is brought down to ambient very quickly by cutting the power to the furnace. The sample capsules are then extracted from the apparatus and recovered from the furnace assembly and are cut open in air (in a fume hood). It is sometimes possible to observe HCl emanating from the capsule as it is opened by sight and smell. The presence of the HCl is a good indication that the polymerisation has occurred. After the HCl has been allowed to evaporate the product is washed repeatedly with distilled water and then with ethanol and acetone. The washing removes any

$Pt(NH_3)_4Cl_2$, which can be formed at the interface of the sample with the platinum capsule during the reaction. Also the starting materials are partially soluble in water so the repeated washing should remove any un-polymerised reactants present in the sample. The washed material is then dried in an oven at 130 ˚C to remove any residual traces of water or solvent. The final product takes the form of a yellow/brown solid. A typical example of the product can be seen in figure 45.

Figure 45. $C_6N_9H_3.xHCl$ after synthesis (before washing).

3.2.2 Compositional Analysis

The composition of the materials synthesised was investigated using bulk elemental analysis, performed in the elemental analysis lab at the UCL Chemistry Department. Several batches of the material have been analysed in this way and the results are presented in Table 1. The average values determined were: N = 43.19%, C = 24.14%, H = 2.19% and Cl = 23.49%, to give a C:N ratio of 1:1.72 close to the expected 1:1.75 for the ideal 6:9 stoichiometry when calculated by weight percent.

For the majority of the samples an insufficient quantity of material was produced in the synthesis to obtain a value for the chlorine content in the samples. However, the bulk analyses indicated a Cl content that was up to ~ 1.5 times larger than expected. This could be partly due to incomplete removal of

reaction side-products or un-reacted starting materials from the samples submitted for analysis.

	Bulk analysis – weight %			
	C	**N**	**H**	**Cl**
	26.05	48.48	2.88	-
	25.96	42.88	1.75	-
	23.42	38.22	1.94	23.49
Average values	25.14	43.19	2.19	23.49
Ideal values	30.32	53.06	1.70	14.92

Table 1. Table outlining the compositional analysis for the carbon nitride material synthesised.

Samples of the material were also submitted for X-ray photoelectron spectroscopy (XPS) analysis. The composition determined from XPS analysis indicated the following composition: O = 7.7%, N = 38.2%, C = 46.6% and Cl = 6.9 %, with the remaining 0.6% presumably due to H. It can be seen that there is a significant percentage of oxygen present in the analysed material; although it is thought that this is due to oxygen that is adsorbed on the surface of the material. As XPS is a surface specific technique the composition determined is that of the exposed surface layers. Therefore, it is not necessarily characteristic of the bulk composition, and can be affected by molecules adsorbed on to the surface of the material. It is possible that the value for carbon is also higher than expected for the bulk due to excess surface carbon adsorbed on to the material as is commonly seen in such experiments. It is therefore possible that the carbon to nitrogen ratio of 1.2:1 shown from these data is not representative of the bulk material and due to the likely excess carbon, the C:N ratio may be closer to the

expected 1:1.75. The chlorine content of 6.9% is less than half of what would be expected for the "perfect" $C_6N_9H_3 \cdot HCl$ stoichiometry. This could mean that the amount of chlorine left in the structure after synthesis is less than expected and that not all of the available voids in the structure contain Cl. However, again this factor may be an artefact of the surface specificity of XPS.

Experimental data seem therefore to indicate that a certain degree of disorder and variation from the nominal $C_6N_9H_3.HCl$ stoichiometry is present in the material, especially related to the Cl and H content. We therefore identify the solid as $C_6N_9H_3 \cdot x$HCl with $x = 1.0 \pm 0.5$. Similar uncertainties in bulk chemical analysis were previously noted by Zhang et al. in their characterisation of similar materials.

In the present experiments, we attempted further chemical composition analysis using analytical SEM and electron microprobe (EMP) techniques. However, the mechanically friable powdered samples could not be readily mounted or polished for EMP analysis, and the necessary C-coating to avoid charging in the electron beam made determination of C/N ratios impossible. Alternative sample coating using Au or other metals also proved unsuccessful.

3.2.3 Scanning Electron Microscopy

Figure 46 shows SEM images of the material synthesised. On close examination is does look as if there is some evidence of a layered or planar structure to the material. Another thing that can be deduced from the SEM images is the fact that the material is probably electronically insulating. This is indicated by the fact that most of the images taken were extremely bright, this is a consequence of the material charging up in the electron beam even though the samples had

been generously sputter coated with gold in an attempt to prevent the material charging during the study. The charging is particularly apparent in the second image. This property of the material in contrast to what is seen for pure carbon graphite; it is well known that carbon graphite is an electrical conductor, a property which utilises the delocalised electrons which reside between the layers. In the proposed structure for this carbon nitride graphene material there are no such delocalised electrons so conduction between the layers is not possible. The images also appear to show that the material is reasonably crystalline.

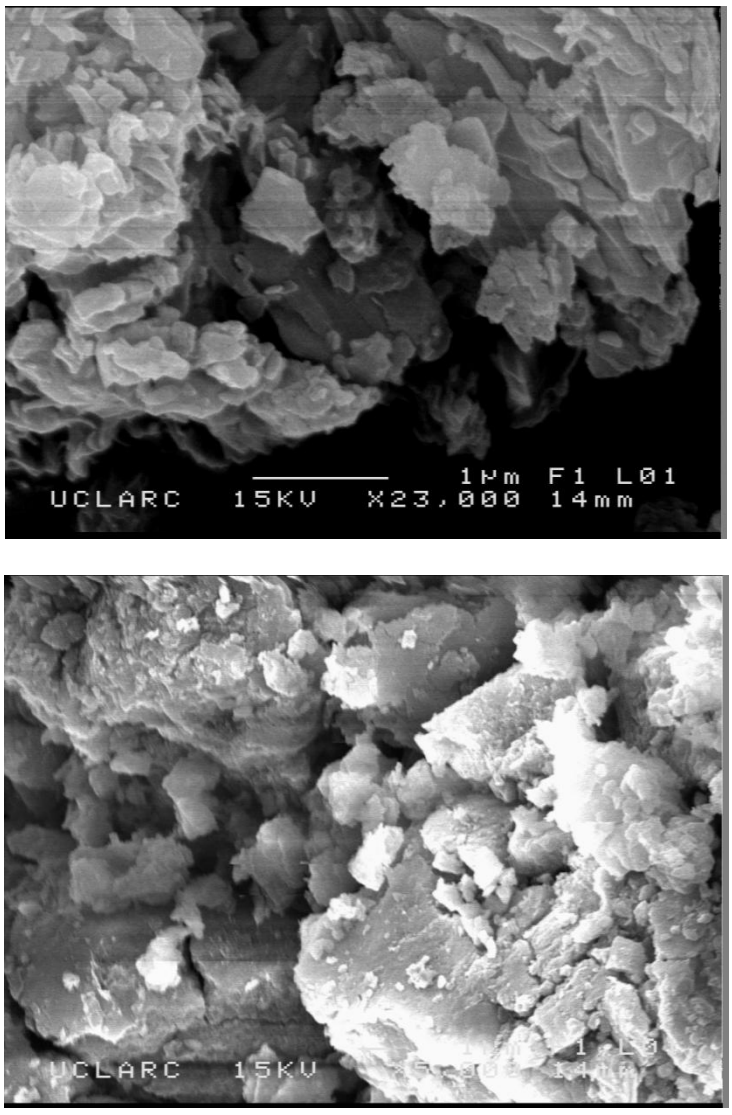

Figure 46. SEM images of the material synthesised.

3.2.4 X-ray Diffraction

The experimentally synthesised material was first characterised under ambient conditions by powder X-ray diffraction carried out in the laboratory using 1.54 Å CuK_{α} radiation on a Bruker D8 diffractometer. The results are in excellent agreement with those reported previously by Zhang et al.[8]; however, our material appears to be slightly better crystallised in that the diffraction peaks are sharper and more features are visible in the spectrum. In both cases, the diffraction peaks are broader than those expected for a well-crystallised fully-ordered solid, with obvious asymmetry in some peak profiles, and both sharper and broader peaks appear in the same spectrum. The diffraction data indicate the presence of a relatively well-ordered bulk crystalline phase, rather than nanoparticles or an amorphous material. The patterns shown in figure 47 correspond to a model where $x \sim 1$.

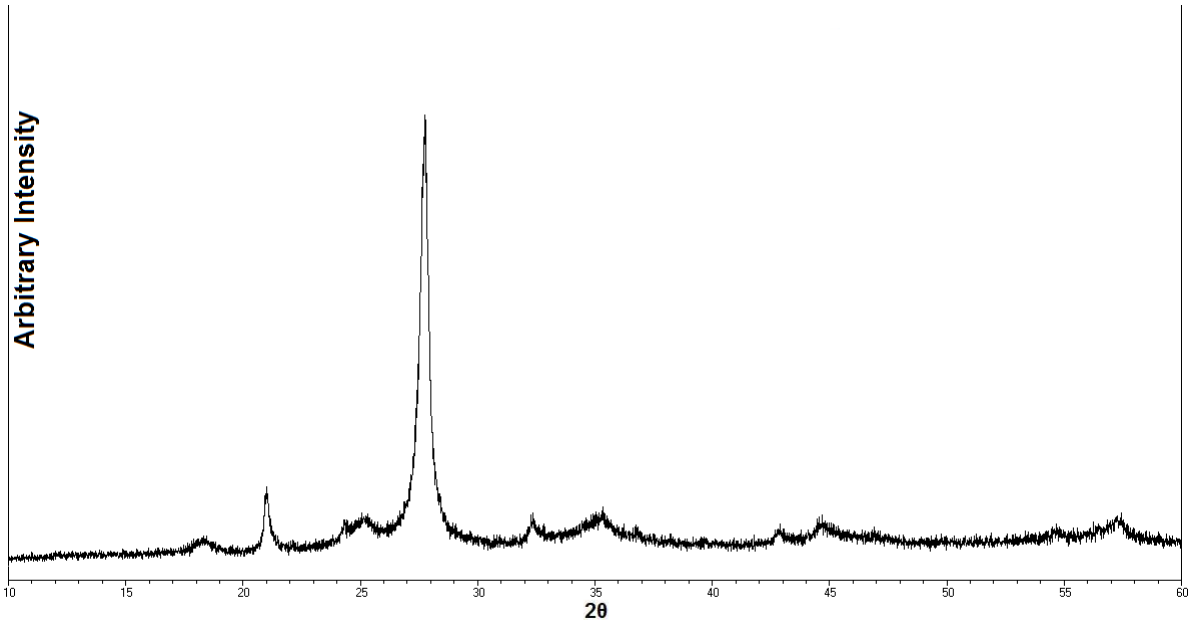

Figure 47. XRD pattern of $C_6N_9H_3.x$HCl synthesised in this work.

The initial structural model used to study the solid *g*-$C_6N_9H_3 \cdot x$HCl compound was that proposed by Zhang et al. with $P6_3/m$ symmetry[8], that was confirmed in the experimental part of the work to represent a good solution to the powder X-ray diffraction data. This model structure was used to generate a diffraction pattern using the program Powder Cell; this simulated pattern was used to compare the experimentally obtained X-ray data with. Figure 48 shows the experimental powder X-ray pattern overlaid on this model. The results show an excellent agreement with this simulated pattern.

No refinement was performed on the X-ray diffraction data obtained for the material, as it was suggested that the quality of the data was insufficient to merit this. Zhang et. al[8] followed by Wolf et. al[45] performed LeBail refinements on the previously synthesised material. However it now seems that the resulting proposed structure was not entirely correct, this is discussed further below in conjunction with the comparison to the computationally calculated data.

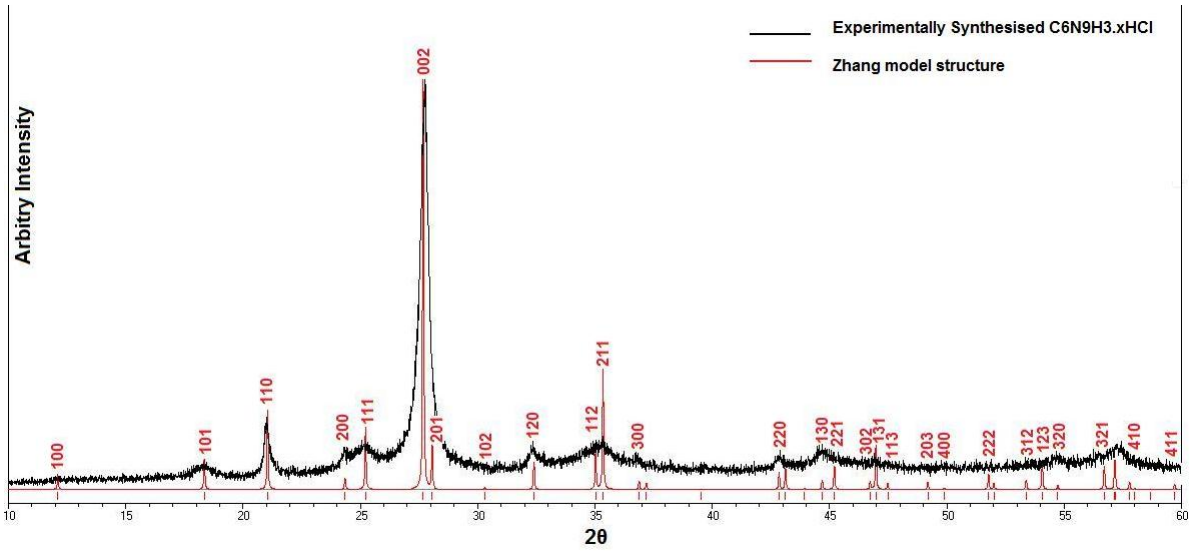

Figure 48. XRD pattern of the experimentally synthesised $C_6N_9H_3 \cdot x$HCl at ambient pressure, compared with the XRD pattern simulated using Zhang's model with $x = 1$.

The experimental data have been indexed according to this model proposed by Zhang et. al. The 2-theta and d-spacing values are tabulated in Table 2.

2θ degrees	***d* – *Å***	***Hkl***
12.10	7.31	100
18.18	4.88	101
21.00	4.23	110
24.39	3.65	200
25.22	3.53	111
27.72	3.22	002
32.33	2.77	210
35.01	2.56	112
35.33	2.54	121
36.80	2.44	300
39.62	2.27	301
42.88	2.11	220
44.61	2.03	310
46.92	1.94	131
54.66	1.68	230
57.22	1.61	303

Table 2. Table listing the positions of the reflections observed in the X-ray diffraction pattern of the synthesised $C_6N_9H_3$.HCl material.

The model structure proposed by Zhang et al. is shown in figure 44; the unit cell comprises of two layers, with stacking sequence ABAB. Note that some of the triazine (C_3N_3) rings in adjacent layers are located directly above each other in the structure, whereas others are located above and below the centre of the $C_{12}N_{12}$ interstices in the two adjacent layers, as indicated in figure 51. The ambient pressure lattice parameters of the synthesised material indexed according to this hexagonal model are a = 8.452Å and c = 6.424Å which are very close to the theoretical values of a = 8.446Å and c = 6.426Å elucidated from the Zhang model. The strong reflection with d = 3.21Å corresponds to the 002 plane that identifies the interlayer separation in the graphitic material.

During the early stages of this work it was necessary to perfect the synthesis process to find the best conditions for the apparatus being used and check the

calibration of the equipment. The reaction conditions were refined by changing the synthesis conditions to attain the correct conditions to produce the target material. During these trial experiments materials that were clearly distinct from the target product were obtained. The pressure and temperature conditions were varied to achieve the best conditions to synthesise the intended product, other conditions such as the sample capsule sealing method and the assembly materials used were also varied to perfect the conditions. It was found that welding the Pt capsule at one end and tightly crimping the other shut in the dry box with specially adapted needle nose pliers was the most effective way to seal it. It was not possible to weld the other end shut after the capsule was filled so as not to risk the precursors decomposing at the high temperatures involved before the beginning of the experiment. Welding one end with a 'trash can lid' type weld, rather than crimp sealing both ends also gave the advantage that there was slightly more space available in the capsule to pack precursor material, making it possible to increase the experimental yield slightly. However, it may also be possible that increasing the length of space available for the precursor material in the assembly could increase the temperature gradient across the sample during the experiment. If this gradient is too large then it is possible that the product material may end up containing different phases at either end of the capsule.

Figure 49 shows the XRD pattern of a very early synthesis attempt. The pattern is compared to the model pattern for graphite and the Zhang structure for $C_6N_9H_3.x$HCl, indicating that the material synthesised is a mixed phase and there is a significant amount of graphite present in the sample. From the high background and the broad peak it also appears that the sample is rather more disordered than samples synthesised subsequently. This may be because the

optimum conditions were not attained and the precursor materials have a tendency to convert to graphite or disordered carbon and molecular nitrogen when the synthesis conditions are too low in pressure and/or the temperature is too high. Other samples were also produced that showed better evidence of the intended product but also showed many other reflections in the pattern in addition to those that were due to the target material (see figure 49).

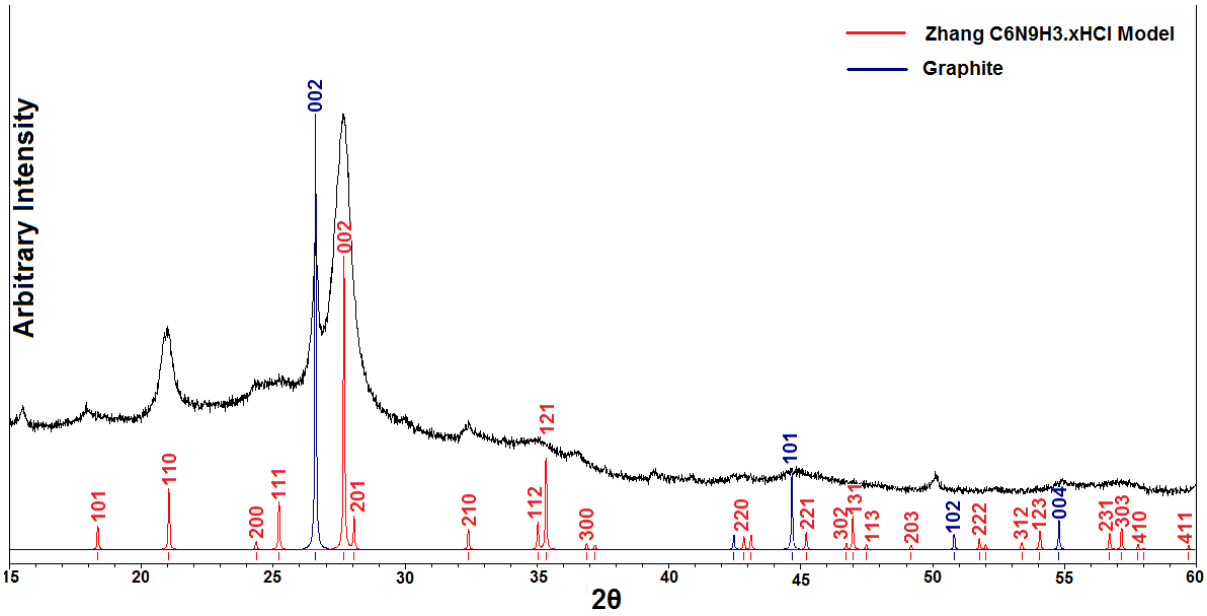

Figure 49. XRD of sample 01-01, the product of an early synthesis run plotted with the model diffraction patterns of C6N9H3.*x*HCl and Graphite.

In figure 50 the XRD pattern of another example of an early synthesis attempt is presented. The material produced here appears to be more crystalline and less disordered. However, there are many more peaks than would be expected for the target material. This may be due to incomplete synthesis and precursor materials remaining in the sample after the experiment had concluded.

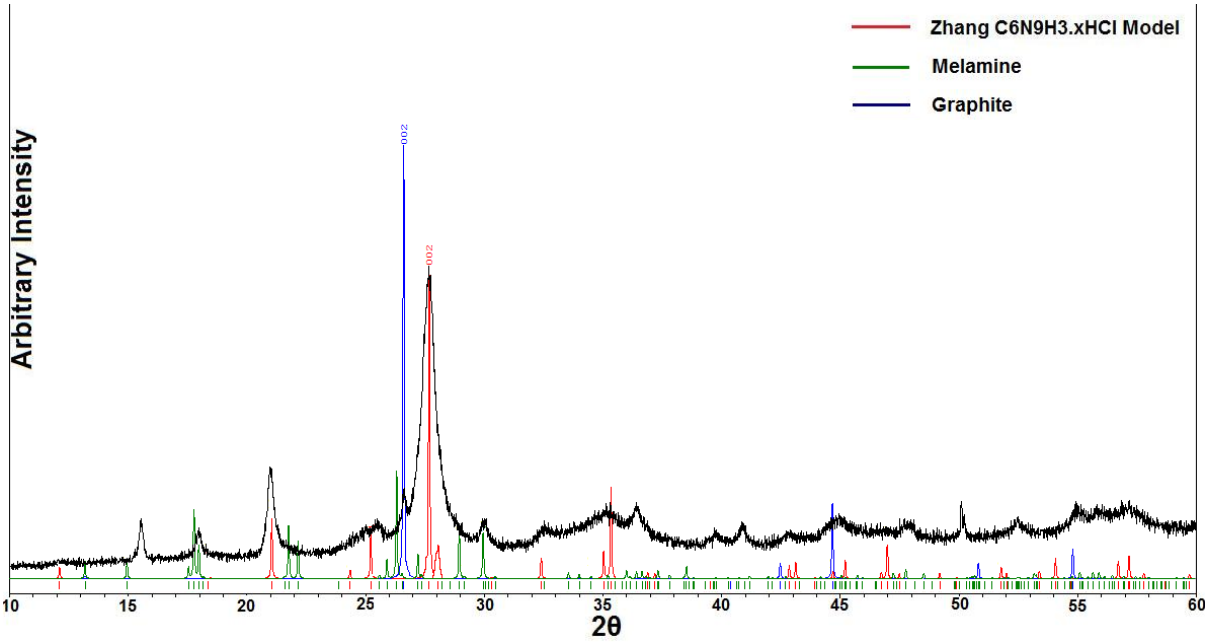

Figure 50. XRD of sample 01-02, an early synthesis run plotted with the model diffraction patterns of C6N9H3.*x*HCl and melamine.

3.3 Theoretical Calculations of Graphitic Carbon Nitride Phases

During part of this work it has been possible to collaborate with Malek Deifallah working with Dr. Furio Cora in the Department of Chemistry at UCL to use DFT calculations to investigate structural details of the *g*-C_xN_y phases. Here is reproduced part of that work that has significance for understanding the structures and interpreting the XRD patterns.

Theoretical calculations of various $C_6N_9H_3$ and $C_6N_9H_3$.HCl layered materials and graphitic compounds were carried out using periodic boundary conditions within the local density approximation (LDA) of density functional theory (DFT) using the plane wave code CASTEP[91,110]. Ultra-soft pseudopotentials for C, N, H and Cl atoms were used and the cut-off energy (450eV) and k-point grid

size (3x3x4) was optimised from single energy point calculations. Further details of the calculations are presented elsewhere[91,110].

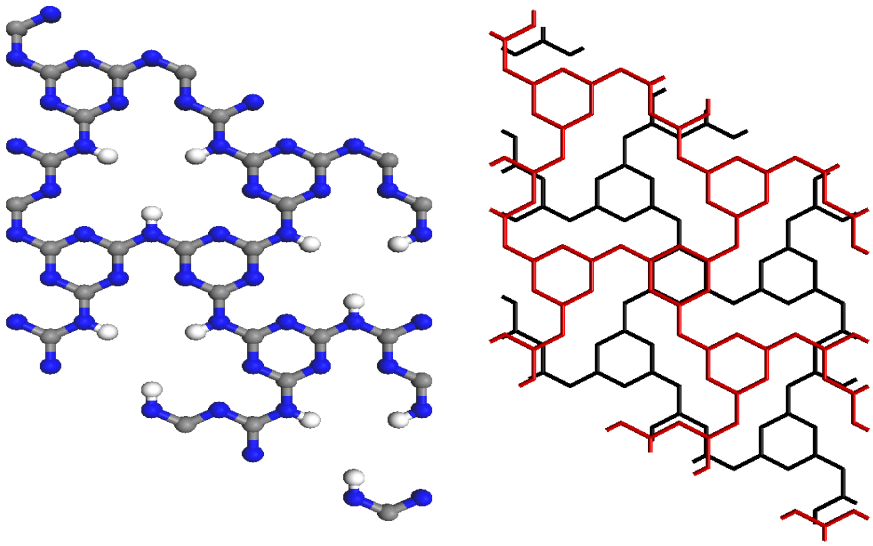

Figure 51. (a) *g*-$C_6N_9H_3$ layer examined in this work with the HCl component absent. Nitrogen is shown in blue, carbon in grey and hydrogen in white; (b) two layers of the material showing that a fraction of the triazine rings of consecutive layers overlap in the solid, whilst other triazine rings correspond to the centre of the voids of adjacent layers.

The initial structural model used to study the solid *g*-$C_6N_9H_3 \cdot x$HCl compound was that proposed by Zhang et al. with $P6_3/m$ symmetry, it was confirmed in the experimental part of the work to represent a good solution to the powder X-ray diffraction data obtained (figure 48). During the theoretical study geometrical optimisations of the material were carried out in the *P1* space group with no symmetry constraints to allow the investigation of H acceptor site ordering and the possible small displacements of C and N atoms in the lattice from their averaged positions that are enforced by the $P6_3/m$ symmetry.

The $C_6N_9H_3$HCl material was first studied theoretically at a pressure of 0 GPa to determine the intrinsic stability of the structure, reproduce the experimentally derived structure and confirm the chemical nature and structural sites occupied

by the HCl component of the material. The positions of the C and N atoms in the $C_6N_9H_3$ backbone suggested by the Zhang et. al. model were generally confirmed. As the HCl component of the material was not confirmed experimentally two limiting cases were examined computationally; one with a full stoichiometric amount of HCl ($x = 1$) and the other with HCl absent from the material ($x = 0$). Comparison of the results enabled investigation of the effects of HCl incorporation on the behaviour of the material under ambient and high pressure conditions, which will be discussed later in a further chapter.

Within the *g*-$C_6N_9H_3$·HCl structure the molecular HCl component can potentially be bound to the carbon nitride framework of the material in one of two ways; physisorptive i.e., molecular HCl species incorporated within voids or chemisorptive, involving H^+ ions attached to N atoms along with Cl^- ions in layer interstices.

FTIR and solid-state ^{13}C NMR data performed in this work[91] and by Zhang et al[8] have indicated that it is most likely that the excess protons are bound to N atoms, consistent with a dissociative chemisorption of HCl, and that Cl ions occupy interstitial sites within voids in the C_xN_y planar graphitic elements. Such a model for *g*-$C_6N_9H_3$·HCl provides two potential non-equivalent Lewis basic sites where H^+ may be accommodated as discussed by Zhang et. al. previously[8]. The two proton-accepting sites are shown in figure 52. The docking site of the proton does not affect the carbon nitride backbone in any way so it is not possible to distinguish between the two using X-ray diffraction.

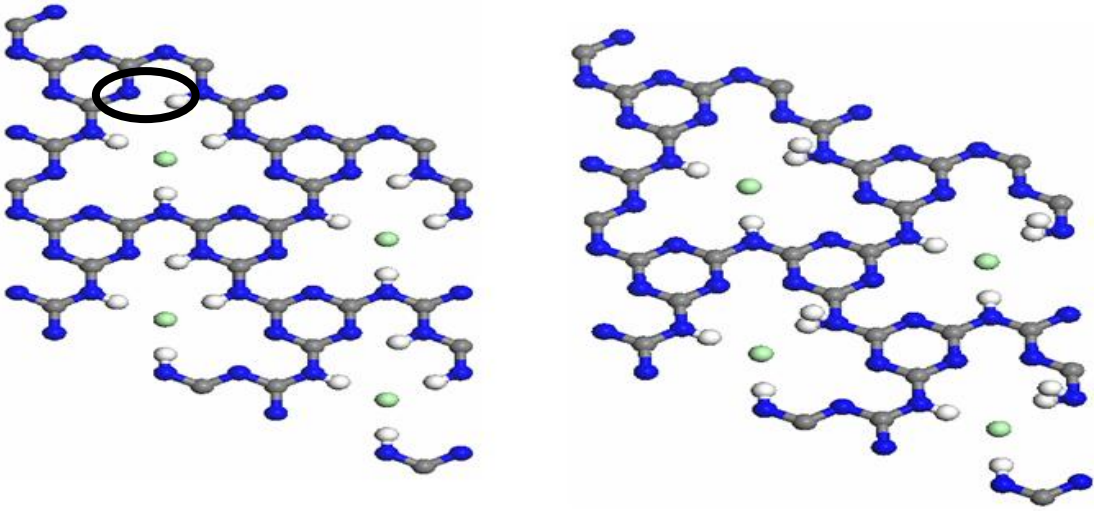

Figure 52. Available proton hosting sites in *g*-$C_6N_9H_3$·HCl (a) proton docked to the N atom of a triazine ring, labelled as N1. The region highlighted indicates that H-bonding may occur between close-lying N and H atoms and; (b) protons docked to bridging NH groups, labelled as N2.

These two potential sites for H^+ binding in the material were investigated computationally. The first case is the 'N1' site as shown in figure 52(a) where the additional HCl protons are located on one of the nitrogen atoms in the C_3N_3 triazine rings in the network. The second case, described in figure 52(b), is where the proton is bound to one of the imide nitrogen atoms linking the triazine rings in the structure. This is labelled as an 'N2' site. If the network is protonated at an N1 site hydrogen-bonding is possible between the proton in question and the nitrogen atom in the adjacent triazine ring, this is shown highlighted by a circle in figure 52(a). If the proton is located on an N2 site then an ammonium like $[R_2NH_2]^+$ species would be formed meaning that the nitrogen atom would have to become sp^3 hybridised therefore disrupting the extended π-electron conjugation of the network. A proton docked at an N1 site would allow the nitrogen atom to remain sp^2 hybridised and there is no disruption of the π-electron conjugation. As can be seen in figure 52 each triangular void in the network contains six N1 sites and three N2 sites. The computational study of

$C_6N_9H_3 \cdot HCl$ considers only a situation where the material is proton ordered, i.e. the same nitrogen atom of the chosen type is protonated in each cavity in the unit cell. In the experimentally synthesised material it is possible that a random protonation of the equivalent sites in each cavity in the network occurs.

The calculations examined four cases at zero pressure; $C_6N_9H_3$, the material with no HCl component present; $C_6N_9H_3 \cdot HCl$ protonated at site N1; $C_6N_9H_3 \cdot HCl$ protonated at site N2 and; $C_6N_9H_3 \cdot HCl$ with the HCl component only physisorbed, that is where the HCl is un-dissociated.

It was found that the calculations for the materials containing HCl always converged to a solution where the N1 site was protonated; this was regardless of the starting location of the proton. If a proton begins at an N2 site it will spontaneously 'hop' to an N1 site upon geometry optimisation. This indicates that protonation of N2 sites does not correspond to a stable energy minimum. A similar situation is seen when starting with a model that has physisorbed HCl, again an N1 site is protonated following geometry optimisation.

$C_6N_9H_3 \cdot HCl$ that is protonated at site N1 only is composed of layers that are atomically flat. This feature has been previously highlighted computationally for a single layer 'graphene' form of the material[91]. As would be expected this structure has an sp^2 hybridisation of the carbon and nitrogen atoms and is stabilised by extended π electron delocalisation across the layers. The forced re-hybridisation to sp^3 on protonation of the N2 site would destabilise the structure by disrupting the delocalised electron network.

The calculations suggest that the dissociated Cl^- ions remain in the centre of the $C_{12}N_{12}$ cavities in the layers having strong electrostatic interactions with the four protons surrounding it bonded to the edges of the cavity. It is also seen that, as

Zhang et. al. suggested, the chloride ions remain in the plane of the layer indicating that the holes are large enough to accommodate the ionic size of the chloride at ambient pressure or it is possible that the chloride ion could have some role in directing the formation of the large holes in the layers of the material. There is a good match between the size of the chloride ion and that of the holes in the layers, this may indicate that the chloride released during the reaction between melamine and cyanuric chloride has a structure directing effect and the particular structure of the layers observed may be a result of this.

The computationally calculated lattice parameters for the $C_6N_9H_3HCl$ and $C_6N_9H_3$ materials are tabulated in Table 3. Comparing the lattice parameters computationally obtained for $C_6N_9H_3HCl$ and the corresponding HCl free analogue; $C_6N_9H_3$, it is observed that the presence of HCl between the layers has a substantial effect on the structural parameters. It gives a reduction of about 0.2Å in the 001 plane and a comparable increase in the interlayer separation, the 002 plane. The local density approximation (LDA) functional, which was used to calculate the structures, is well known for systematically over estimating the strength of interactions, in particular non-bonded ones, and results in lattice parameters underestimated with respect to experiment. The over-binding effect is not observed in the HCl free model but is present when considering the $C_6N_9H_3{\cdot}HCl$ composition. Therefore, comparison of the calculated lattice parameters with the experimental ones supports the idea that HCl is indeed retained in the structure after synthesis. This agrees with the chemical analysis of the experimentally synthesised material as discussed earlier.

parameter	**Comp. *g*-**	**Comp. *g*-**	**Exp. *g*-$C_6N_9H_3$•*x*HCl**

	$C_6N_9H_3$•*x*HCl	$C_6N_9H_3$	
***a* (Å)**	8.372	8.565	8.446
***b* (Å)**	8.370	8.565	8.446
***c* (Å)**	6.230	6.039	6.426
***α* (deg.)**	89.682	90.000	90.000
***β* (deg.)**	92.557	90.000	90.000
***γ* (deg.)**	119.724	120.000	120.000

Table 3. Experimental and computationally predicted cell parameters for *g*-$C_6N_9H_3$ structures. The computational *g*-$C_6N_9H_3$·*x*HCl phase corresponds to protonation at site N1.

The hypothetical material without the HCl component present in the layers recovers to the hexagonal *P6₃/m* symmetry previously suggested. The material containing HCl shows a similar behaviour. However, the calculations indicate that the lowest energy form of the $C_6N_9H_3$·HCl material exhibits small, but non-negligible, deviations from the ideal hexagonal *P6₃/m* symmetry. This is apparent in the different values of the optimised *a* and *b* lattice parameters, and deviation of the predicted cell angles away from 90º and 120º enforced by the hexagonal symmetry.

The proton ordering built into the model breaks the symmetry equivalence of the six N1 sites in the $C_{12}N_{12}$ cavities within the layers. Another effect of the proton ordering is that a dipole is generated in each cavity, the positive and negative poles corresponding to the location of the H^+ and Cl^- ions in the cavity. Interaction of the dipoles in adjacent layers would cause a small relative shift between layers in the 001 plane. The predicted deviation from hexagonal symmetry within the proton ordered model is small, with a difference of about 0.002Å between the *a* and *b* parameters. This shift does present a useful interpretation of the broadening and appearance of additional weak peaks

observed in the X-ray diffraction pattern of the experimentally synthesised samples.

Figure 53 compares the computationally generated X-ray diffraction pattern for the $C_6N_9H_3{\cdot}HCl$ structural model with that of the Zhang model for $C_6N_9H_3.HCl$. Initially when inputting the unit cell parameters to generate a pattern for the computationally calculated structure there is a mismatch between the *d* values. This is mainly due to that fact that the DFT results are calculated for a temperature of 0K, also there is a slight underestimation of lattice parameters calculated with LDA. Therefore it can be seen that the major reflections are present in both patterns but do not quite line up with each other due to the reasons outlined above. If the lattice parameters are altered, as in figure 54, so that the values of *a*, *b* and *c* are the same as those in the experimental data then the positions of the peaks in both model line up as would be expected.

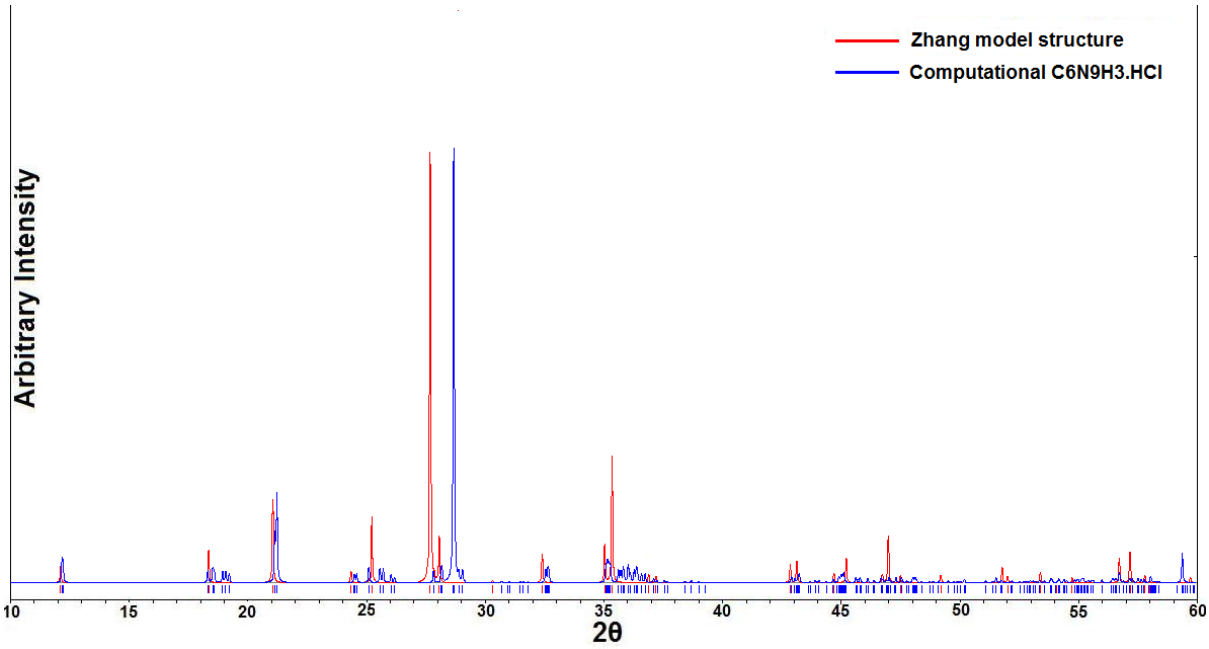

Figure 53. Simulated diffraction patterns for the Zhang et al model and the computationally derived $C_6N_9H_4Cl$ structure.

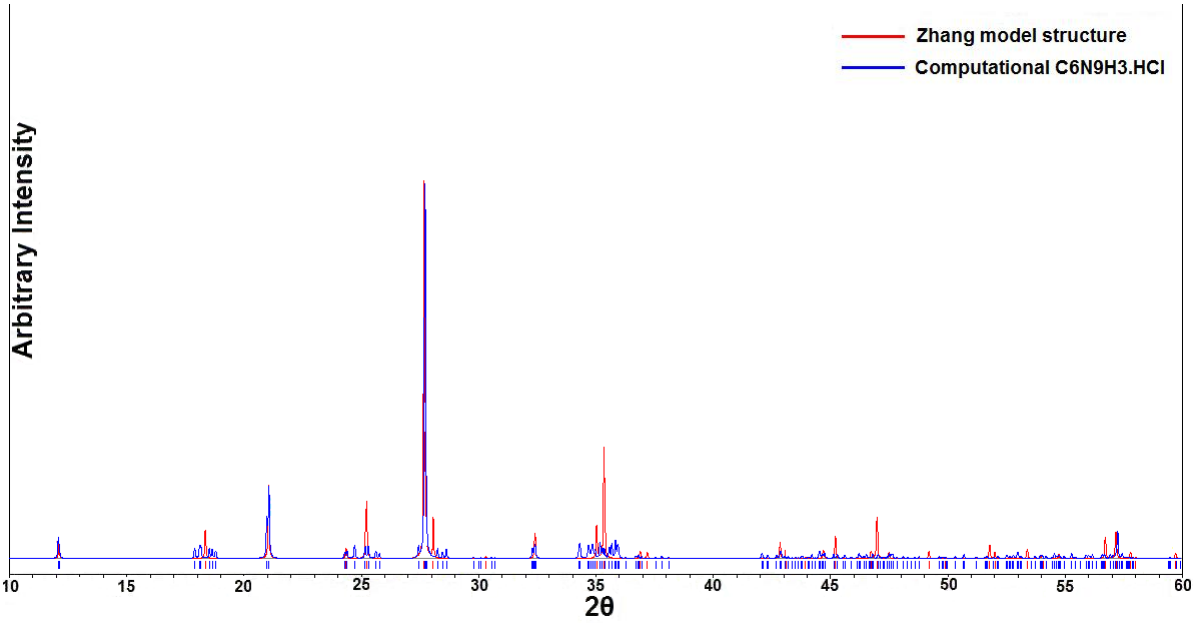

Figure 54. Simulated diffraction patterns for the Zhang model structure for $C_6N_9H_3$.HCl and the computational model of $C_6N_9H_3$.HCl from this work (with unit cell lengths matched to the experimental model).

The pattern generated from the computational data contains small clusters of peaks that are not observed in the Zhang model. These clusters are linked to the symmetry lowering upon proton ordering. In fact if the cell angles of the computational model are altered to 90° and 120° as would be enforced by hexagonal symmetry these small clusters of peaks disappear and the computational data generates a diffraction pattern identical to that of the Zhang model.

Figure 55 shows the computationally derived X-ray diffraction pattern for the $C_6N_9H_3$.HCl material with the X-ray diffraction pattern for the experimentally synthesised material. It is interesting to observe that the clusters of peaks present in the X-ray diffraction pattern generated from the computationally calculated data provide an excellent match with the broad peaks observed in the diffraction pattern of the material synthesised experimentally. It is therefore plausible that the synthesised material actually exhibits a deviation from

hexagonal symmetry consistent with the effect of proton ordering observed in the computational model. Such a phenomenon would therefore enforce a small deviation in cell angles from the values of α = 90°, β= 90° and γ= 120° stipulated by the hexagonal space group originally assigned to the material to α = 89.68°, β= 92.56° and γ= 119.72°. This would also involve a small shift in the layers with respect to each other in the 001 plane. It is therefore likely that the actual layer stacking structure in the experimental material is more complex that Zhang et. al. originally suggested.

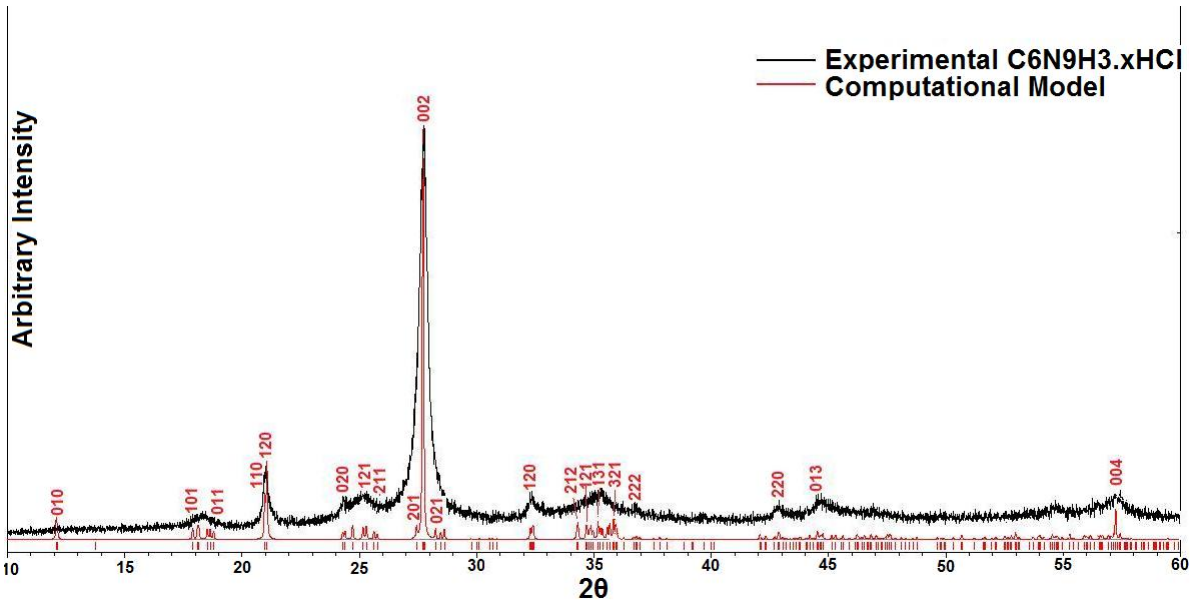

Figure 55. Simulated XRD using the calculated equilibrium structure of $C_6N_9H_3 \cdot HCl$ (with unit cell lengths matched to the experimental model) overlaid to the experimental XRD pattern at ambient pressure.

As already discussed, it was not possible to determine the exact HCl content of the material experimentally. Theoretically two limiting conditions were examined, one with the fully chlorinated stoichiometry of the $C_6N_9H_3 \cdot xHCl$ where x = 1 with all voids in the layers occupied with HCl and the other where x = 0, assuming the structure is completely HCl free.

Comparison of the results allows investigation of the effects of HCl incorporation on the structural behaviour and properties of the material.

Figure 56 displays simulated XRD patterns using the computationally calculated structure for *g*-$C_6N_9H_3 \cdot x$HCl with the Cl occupancy varied from 0 to 1, overlaid is the experimental diffraction pattern for the material at ambient pressure. It is clear that the closest match to the experimental data is when the Cl occupancy is equal to 1. This supports the idea that the synthesised material has a stoichiometry close to $x = 1$. Overall, the combination of the computational and experimentally generated diffraction patterns indicate that there is a significant amount of HCl intercalated within the material and that when considering the $C_6N_9H_3 \cdot x$HCl formula for the material that $x \sim 1$.

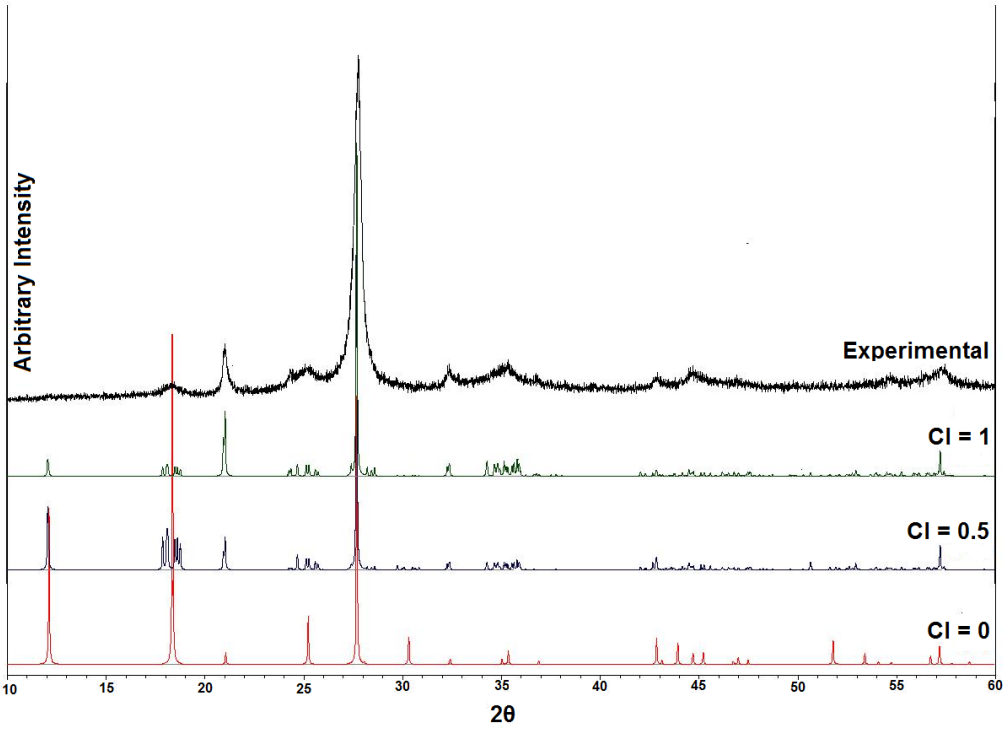

Figure 56. XRD patterns simulated using the computational structure of *g*-$C_6N_9H_3 \cdot x$HCl and varying the HCl occupancy from 0 to 1, compared to the experimental XRD pattern at ambient pressure.

3.4 Infrared Spectroscopic Characterisation

The material has also been studied by IR spectroscopy to gain additional information about the structure and bonding of the material. A typical IR spectrum of the synthesised $C_6N_9H_3 \cdot HCl$ material is shown in figure 57. IR spectra were taken on a Bruker *IFS 66v/S*FTIR spectrometer. Samples were prepared by grinding with KBr and pressing into pellets, the IR grade KBr was obtained from Sigma-Aldrich and used as received. Also presented in figure 58 is a comparison of the FTIR spectrum of the precursor material melamine compared with that for the $C_6N_9H_3 \cdot HCl$ material. Upon inspection of the FTIR spectra the material appears to be well matched with that synthesised by Zhang et. al.[8] as previously reported, a good indication that the material synthesised in this work is indeed comparable and that the previously discussed model structure is a good starting point for the investigation of the structure and composition of the material.

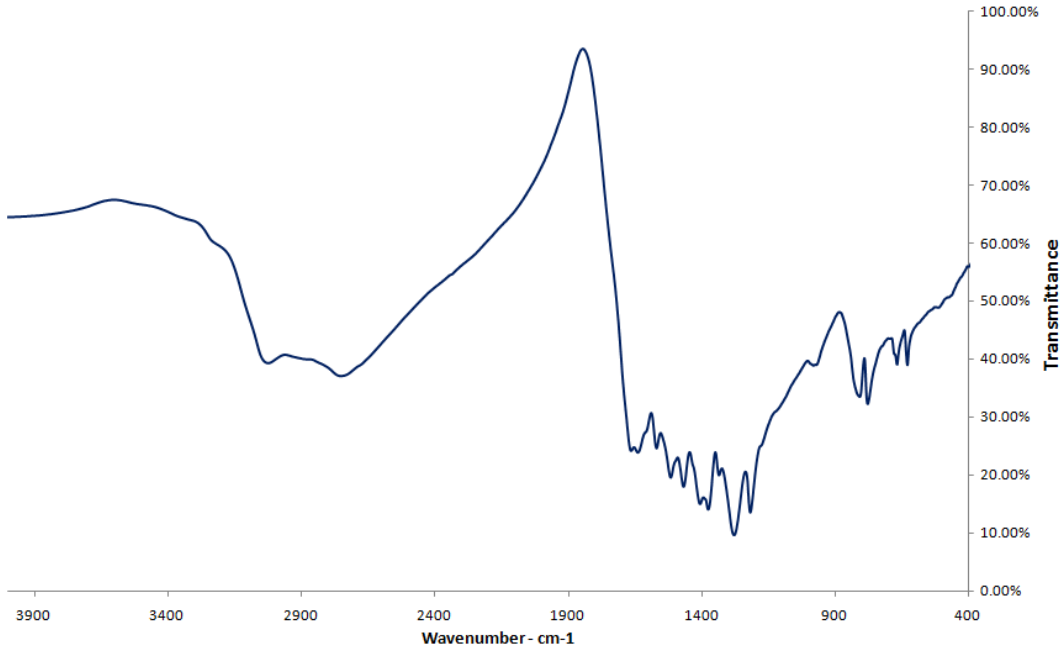

Figure 57. Infrared Spectrum of the $C_6N_9H_3 \cdot HCl$ material in a KBr pellet.

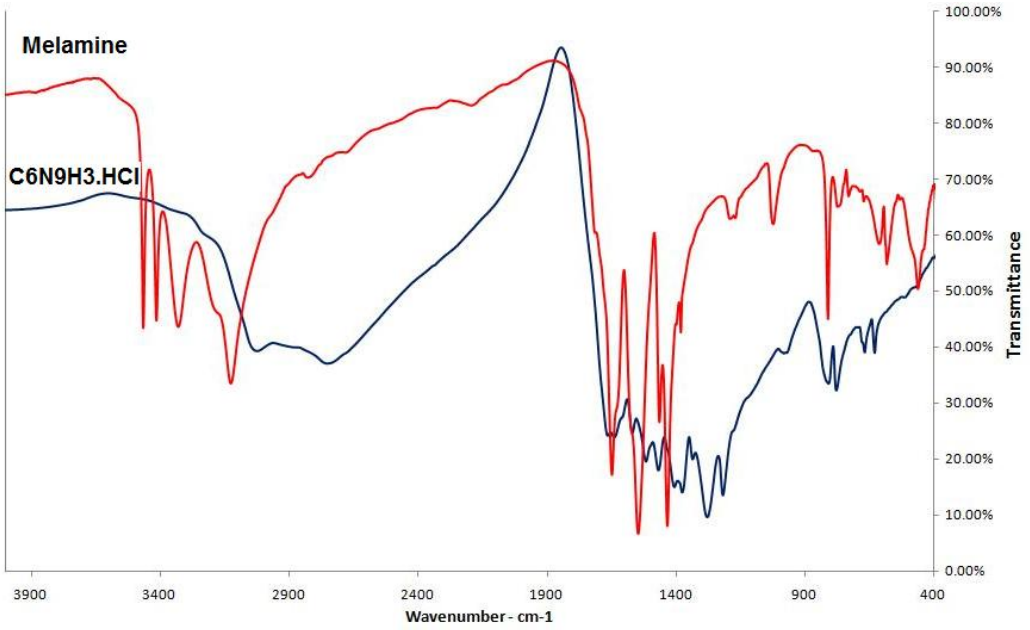

Figure 58. Infrared Spectrum of the $C_6N_9H_3 \cdot HCl$ material compared with that of the precursor material melamine.

Above is shown the IR spectrum of the $C_6N_9H_3 \cdot HCl$ material compared with that of the precursor material melamine. Both spectra are characterised by several strong bands in the 3000 cm^{-1} region which can be related to modes involving the N-H stretching vibrations. Both spectra also exhibit a series of bands in the 1200 – 1600 cm^{-1} region which are typical of the CN heterocyclic structures contained in both materials; features in this region can be associated with the skeletal stretching vibrations of these aromatic rings[92]. For melamine in particular the sharp bands observed above 3000 wavenumbers can be attributed to the symmetric and asymmetric stretching of the terminal $–NH_2$ groups. The sharp bands above 3300 cm^{-1} in melamine are associated with the stretching modes involving hydrogen atoms that are not hydrogen bonded, while the slightly lower frequency, broader bands are associated with the stretching of N-H groups involving units that are hydrogen bonded. The bending vibration for

the terminal $–NH_2$ groups in melamine can be seen just above 1600 wavenumbers[93].

For the $C_6N_9H_3{\cdot}HCl$ product material the symmetric and asymmetric $–NH_2$ stretching modes do not appear above 3000 cm^{-1}. These are replaced by two very broad bands of lower frequency which are observed around 3033 cm^{-1} and 2752 cm^{-1}. These bands are typical of stretching vibrations of N-H units and indicate that there is some hydrogen bonding between these units and other atoms within the framework. In the hypothetical $C_6N_9H_3$ framework structure previously discussed there would only be one N-H environment therefore only one stretching vibration would be expected. In an un-protonated $C_6N_9H_3$ framework the only N-H environment would be the bridging nitride group between the C_3N_3 triazine rings, the band observed at 3022 cm^{-1} would be consistent with the stretching of this imido unit. Ordinarily the observation of this band in neutral species, i.e R_2N-H, would be expected at a higher wavenumber[92]. However, the material under study contains the additional HCl component dissociated within the network, this introduces an electrostatic interaction with the Cl^- ion, i.e R_2N-$H^{\cdots}Cl^-$, which could lower the frequency of the observed band. The presence of the H^+ ion from the dissociation of the HCl component in the layers will also cause the formation of more N-H species within the material through the protonation of the framework, which may give rise to additional bands in the IR spectrum.

As discussed previously there are 2 possible sites that this additional proton could occupy in the material. Figure 52 illustrates the so called N1 and N2 sites that have been investigated computationally, both of which are indistinguishable by X-ray diffraction as the framework structure is unaffected regardless of

where the proton docks. If the proton was to dock on the N2 site (figure 52(b)) the nitrogen atom would re-hybridise to sp^3 and the π-conjugation of the layer would be disrupted. If the N1 site is protonated (figure 52(a)) then the nitrogen remains sp^2 hybridised and the electron conjugation is not disrupted. This option is more energetically favourable and computationally this was calculated as the most likely location for the HCl proton to inhabit. Also the possibility of hydrogen bonding to the adjacent nitrogen atom in the triazine ring (figure 51(a)) would help explain the unusually low stretching frequency seen for the product material at 2752 cm^{-1}[8].

It is worth noting that there are no bands observed in the 2200 cm^{-1} region of the IR spectrum. This indicates that there are no triply bonded CN cyano groups or cumulated double bonds (-N=C=N-) present in the material. Bands in this region are often associated with the high temperature degradation of the triazine ring[43-44].

The multiple bands in the 1600-1200 cm^{-1} region are typical of many compounds that contain carbon nitrogen hetrocycles. These bands can be attributed to the stretching vibrations of the s-triazine ring. It is also possible to assign the bands seen in the 800 cm^{-1} region of the spectrum to out of plane deformations of the triazine ring. The spectrum shows two sets of three sharp IR peaks, one at 666, 636, and 630 cm^{-1}, and the second at 832, 817 and 782 cm^{-1}. The triple peak near 800 cm^{-1} was already noted by Zhang et al.[8] the lower frequency peaks were not observed in that study due to the instrumental cut off and are reported here for the first time. A theoretical study of vibrational modes in *s*-traizine[94] assigned modes at 748 and 675 cm^{-1} to in and out of plane bending vibrations of the C_3N_3 traizine ring. A similar interpretation was put forward for IR and Raman active

bands occurring for melamine in this region[95]. Therefore the bands in the region of 900-500 cm^{-1} can be assigned to triazine like ring deformations.

Chapter Four – Spectroscopic Characterisation of $C_6N_9H_3$.HCl: UV and near-IR (Fourier Transform) Raman Spectroscopy

4.1 Introduction

In this chapter we examine the structure and optical properties of the layered graphitic material $C_6N_9H_3$.HCl using various spectroscopic techniques, especially Raman scattering spectroscopy with UV or near-IR excitation (Fourier Transform Raman spectroscopy). These data provide new insights on the local structure and the ordering of the triazine, and other ring units within the graphitic CN material that cannot be deduced from the X-ray diffraction analysis. Raman scattering spectroscopy is a valuable technique for investigating the structure and bonding in poorly crystalline and amorphous solids. Usually, the Raman spectrum is excited by a laser with a wavelength in the visible range of the spectrum. However, due to the electronic nature of the graphitic CN material that resulted in intense fluorescence, it was not possible to gain useful structural information using conventional visible Raman spectroscopy. However, we could successfully obtain Raman spectra using UV excitation wavelengths (224 nm and 229 nm). UV Raman spectroscopy is a rapidly developing optical technique that is only currently available in a few laboratories throughout Europe. These pioneering experiments were carried out in collaboration with the UV Raman spectroscopy facilities and laboratories at ENS Lyon and Université Joseph Fourier (Grenoble) in France. However, the interpretation of the data is complicated by resonance Raman effects that enter the analysis because of the interaction between electronic transitions of π-

bonded heterocyclic rings contained within the structure in the UV region and vibrational excitations. Additional Raman spectra were then obtained using near-IR excitation (1064 nm) using Fourier Transform methodology, in collaboration with the CNRS-CRPHT laboratory in Orléans, France. Once more, this is a novel technique being applied to Raman spectroscopy of solids, and we encountered additional questions and problems for interpretation of the data, especially since larger ring structures within the graphitic CN materials can exhibit electronic transitions in the near-IR region. The UV and FT-near IR Raman results are interpreted to give some valuable new information on the local structure and ordering within the C,N graphitic sheets; however, they also raise new questions related to the electronic structure and its coupling to radiation that must be addressed in future work.

4.2 Experimental Procedures

It was first attempted to obtain Raman spectra of the $C_6N_9H_3 \cdot HCl$ material using various visible excitations with wavelengths of 787-325 nm on the home built and Rennishaw micro-Raman systems installed at UCL[96]. All such experiments resulted in intense photoluminescence that completely obscured any Raman spectrum that the material may have exhibited. A typical example of which can be seen in figure 59 below.

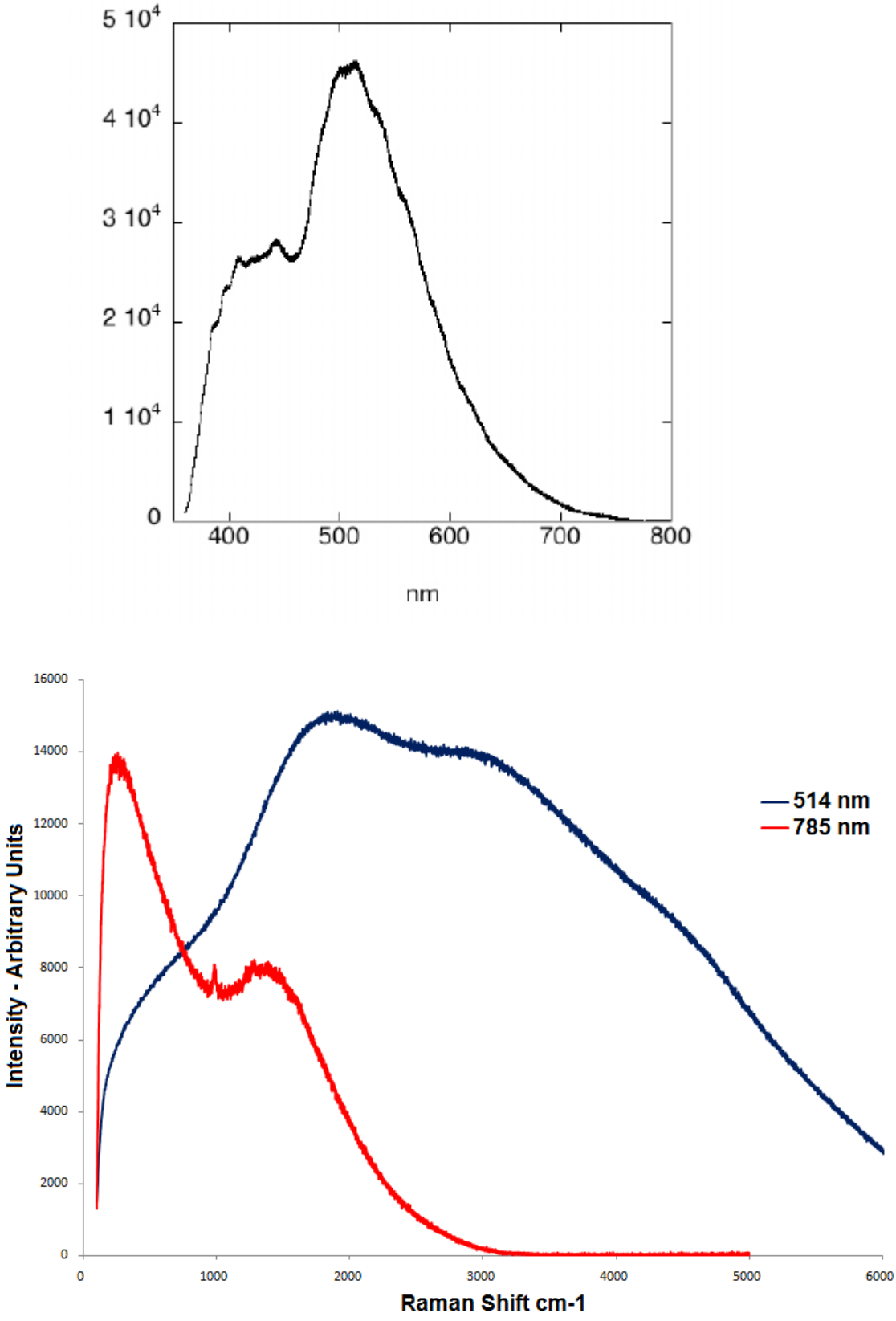

Figure 59. Top, typical photoluminescence spectrum of $C_6N_9H_3 \cdot HCl$ excited using 325 nm laser excitation. The Raman peaks appear as weak features on the low energy side of the main fluorescence peak. Bottom, visible Raman spectra of the material using 514 and 785 nm excitations.

Previous reports of nanocrystalline C_xN_y materials have also noted the appearance of extreme fluorescence under the excitation of visible and UV radiation and no such Raman spectra have been reported thus far[5]. It has been previously documented that molecular, oligomeric and solid state aromatic systems containing heterocyclic C,N units often exhibit strong fluorescence when excited in the UV-visible region because of π-π* transitions and the interaction of other electronic transitions. During this investigation UV excitation was used to obtain Raman spectra for the $C_6N_9H_3{\cdot}HCl$ material[82] (see figure 60).

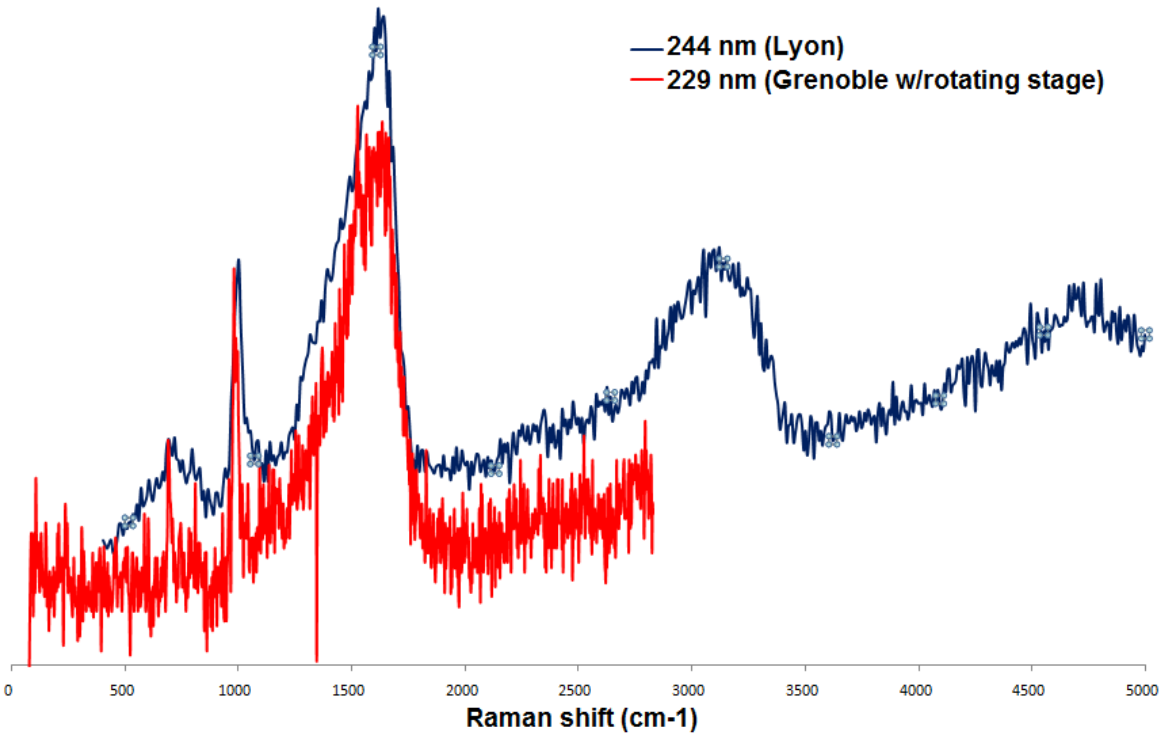

Figure 60. UV Raman spectra of the $C_6N_9H_3$.HCl material taken firstly at the Laboratoire des Sciences se la Terre at the ENS, Lyon with 224 nm excitation and then at the IPNG in Grenoble at with 229 nm excitation and using the rotating stage to prevent sample degradation.

Samples were first excited using 224 nm radiation from a frequency doubled Ar^+ laser using a Jobin Yvon-Horiba LabRam micro-beam UV Raman system installed at the Laboratoire des Sciences se la Terre at the ENS Lyon, France. The incident radiation was focussed on the sample and the scattered radiation collected using a 40x UV objective and the sample area illuminated had a diameter of 4-5µm. Spectral gratings of either 3600 or 600 gr/mm were used to collect spectra over a wide range with low resolution or with high resolution over a narrower range.

During initial experiments changes in the spectra as a function of time were observed (see figure 61). This could be an indication that the sample was being degraded or affected upon irradiation by the UV laser during the course of the experiment. Therefore in subsequent studies the power of the incident laser was limited to 100-500 µW before it entered the microscope and tests indicated that the power incident on the area of the sample illuminated was on the order of 10-15 µW. When the sample was subjected to only low laser power, no time dependent changes in the resulting spectra were observed. Also further experiments were carried out using a 229 nm laser excitation at the IPNG in Grenoble that involved using a specially built rotating stage that supported the sample during irradiation. The stage ensured that the sample under investigation was constantly moved under the beam so that no one particular portion of the material was irradiated constantly so that it was less likely that photo-degradation of the material would occur. The results obtained were identical to those from the Lyon experiments as can be seen in figure 60 indicating that no time/exposure dependent degradation had taken place.

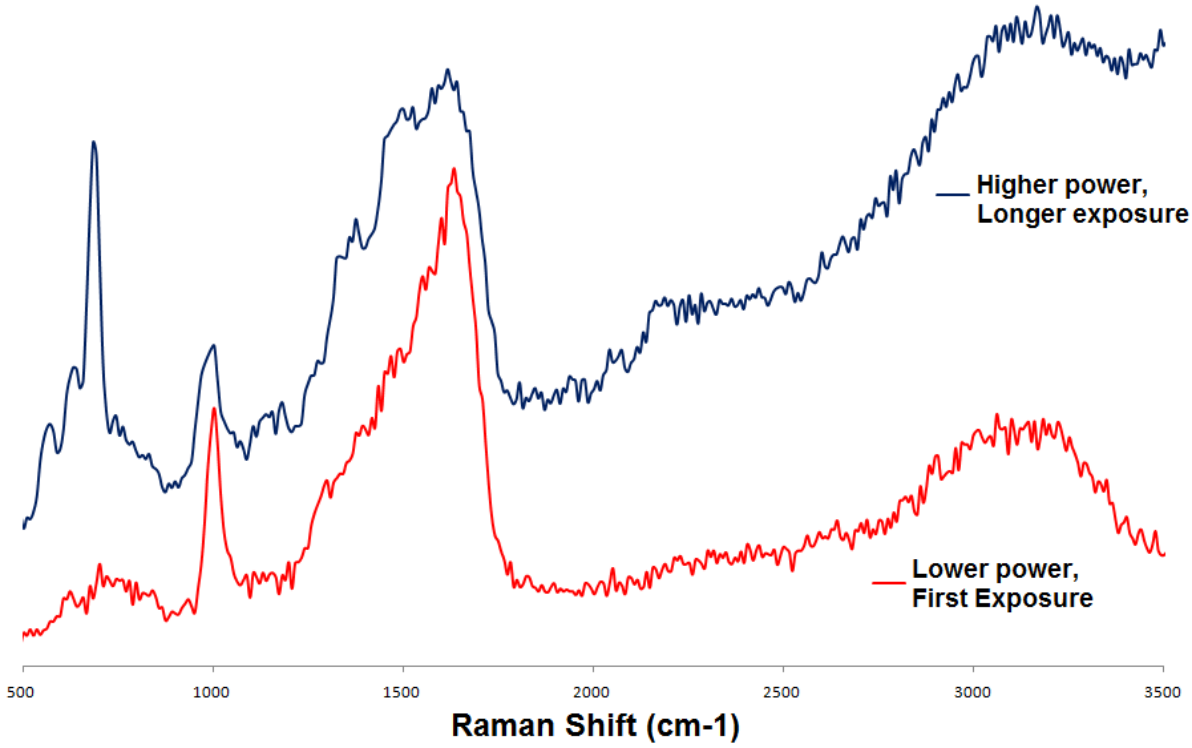

Figure 61. Comparison of 229 nm UV Raman spectra of the $C_6N_9H_3$.HCl material when it was exposed to the laser with high power and the same spot irradiated for some time and with a spectrum of the material with the laser at much lower power and the spot being irradiated for the first time.

4.3 Results and Discussion

The first attempts to study the $C_6N_9H_3$·HCl material spectroscopically were undertaken using laser excitations ranging from various wavelengths in the visible through to the UV region, i.e. 785, 514, 488 and 325 nm. All these experiments resulted in intense photoluminescence that completely obscures the Raman spectrum of the material (see figure 59). It was therefore necessary to use a laser excitation of a different wavelength to try to avoid exciting the electronic transitions that result in the fluorescence. UV Raman spectra free from fluorescence effects were obtained using a 224 and 229 nm excitation at the ENS in Lyon, France and with 229 nm excitation with a rotating stage system at

the IPNG in Grenoble, France (figure 60). UV Raman spectra were of the materials triazine, cyanuric chloride, melamine and "melon" as molecular standards using the same systems.

UV Raman spectra of $C_6N_9H_3{\cdot}HCl$ obtained during this investigation display an intense, broad, asymmetric feature in the 1200-1700 cm^{-1} region of the spectrum, this is attributed to C-N stretching vibrations, see figure 60. This region is characteristic of the "D" and "G" bands that are often observed for disordered carbon and graphite materials and also seen in amorphous C,N containing systems[84,-88,97]. The observation of this feature associated with "disordered" materials is interesting to note. The $C_6N_9H_3$.HCl material has been studied using several other characterisation techniques and appears to have a relatively high degree of structural order so it is surprising to find such "amorphous" features in the Raman spectrum. The broad bands observed in the 3000 cm^{-1} and 4500 cm^{-1} region are attributed mainly to 2nd and 3rd order Raman scattering associated with the fundamental C-N stretching vibrations occurring in the 1200-1700 cm^{-1} region. However, IR spectra of the material also indicate the presence of N-H stretching modes in the 2500-3000 cm^{-1} region. Sharp peaks are observed at 690 and 980 cm^{-1}; these can be attributed to the breathing mode of the C_3N_3 triazine rings within the network structure[8,46,98]. The peak at 690 cm^{-1} is observable with both the 224 nm excitation and the 229 nm excitation with the rotating stage. However, the intensity of the peak is higher in the latter experiment but this may be due to the lower power laser excitation used to conduct the earlier experiment. Due to the optical cut off filter used to discriminate against the exciting laser in the Jobin Yvon-Horiba instrument

spectra could not be obtained below 500 cm^{-1} for the 224 nm excitation experiments conducted in Lyon.

Using the rotating stage and the JY T64000 spectrometer, UV Raman spectra could be obtained down to 100 cm^{-1}. No additional features are observed in this low frequency region. One important feature to note is that neither the Raman nor IR spectra of the material exhibit features in the 2000-2500 cm^{-1} region. Features in this region are attributed to the presence of triply bonded species such as C≡N units or N=C=N groups in the structure. Therefore it can be assumed that these groups are absent from the structure of the $C_6N_9H_3{\cdot}HCl$ material under study[99-102]. These features are however observed in CN_x films and in 'tholin' materials designed to model the atmospheric composition of Titan in gas discharge experiments that produce aerosols containing CN compounds which appear to contain a lot of aromatic species and seem to be related in some way to the $C_6N_9H_3{\cdot}HCl$ material studied here[9,46].

The Raman and IR spectra of *s*-triazine ($C_3N_3H_3$) and melamine ($C_3N_3(NH_2)_3$) have been studied using *ab initio* theoretical calculations[95,103]. Both gas phase IR and solid state FT-Raman spectra have been recorded for *s*-triazine[9,46,95] and solid state IR and FT-Raman spectra are known for melamine[8,9,11,46,95]. The materials are therefore well understood spectroscopically. The *s*-triazine molecule is the simplest heterocycle containing the C_3N_3 ring. However, it is not the best model for understanding the vibrations of condensed carbon nitride. Both the species *s*-triazine and melamine are molecular and not part of a large continuous network, as the heterocyclic units in

the $C_6N_9H_3{\cdot}HCl$ material would be. The molecular vibrations of these small molecules are not constrained by the connectivity to a planar lattice.

The symmetric breathing vibration of the nitrogen atoms in the C_3N_3 ring gives rise to a strongly Raman active peak that can be observed in the Raman spectra of *s*-triazine and many of its derivatives, including melamine; this feature appears at around 970-1000 cm^{-1}[95,103], which can be seen in figure 62 below.

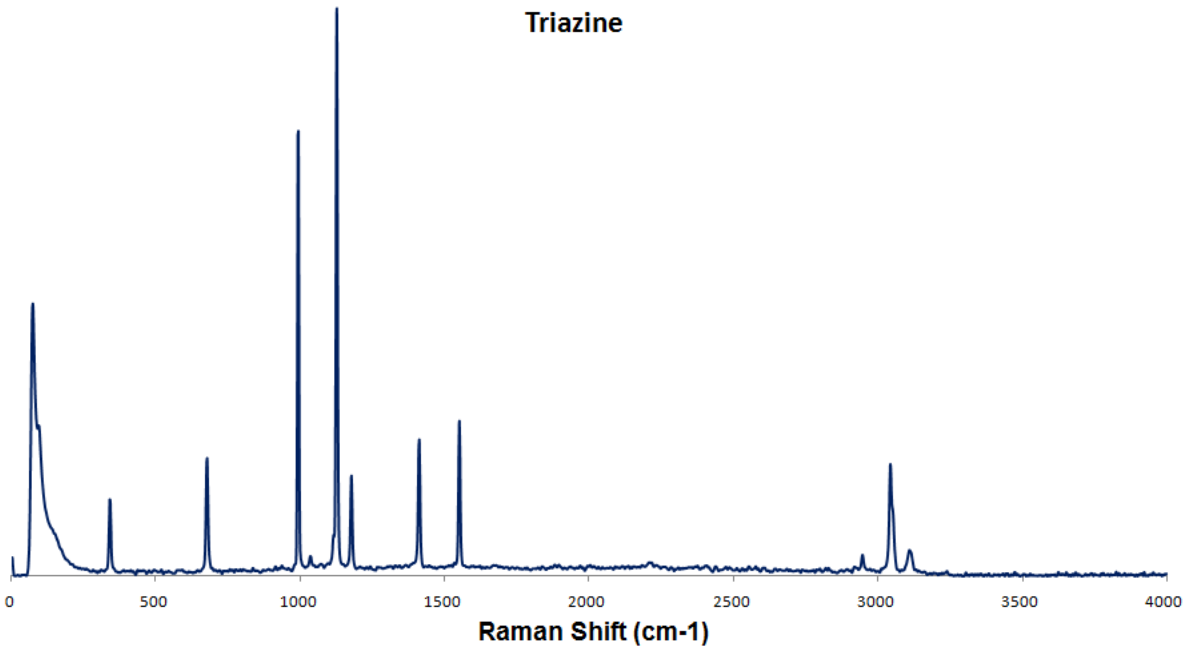

Figure 62. FT Raman spectrum (1064 nm excitation) of *s*-triazine.

The mode is not coupled to other atomic displacements in the molecule so a similar symmetric nitrogen breathing vibration might be expected to appear in the Raman spectra of condensed materials containing the C_3N_3 unit where the polymerisation occurs through the carbon atoms. This is indeed seen to be the case; the UV Raman spectra of $C_6N_9H_3{\cdot}HCl$ and graphitic carbon nitride tholin

structures contain a peak at 980 cm^{-1} that can be assigned to the symmetric nitrogen breathing vibrations of the C_3N_3 triazine ring units. Figure 62 shows the Raman spectrum of triazine.

Another sharp peak appears in the UV Raman spectra of the $C_6N_9H_3 \cdot HCl$ material at 690 cm^{-1} which corresponds to a strong Raman feature that is observed in both *s*-triazine and melamine; the Raman spectra of melamine is shown in figure 63. This feature is due to a mode involving in-plane bending vibrations of the C-N-C linkages[95,99].

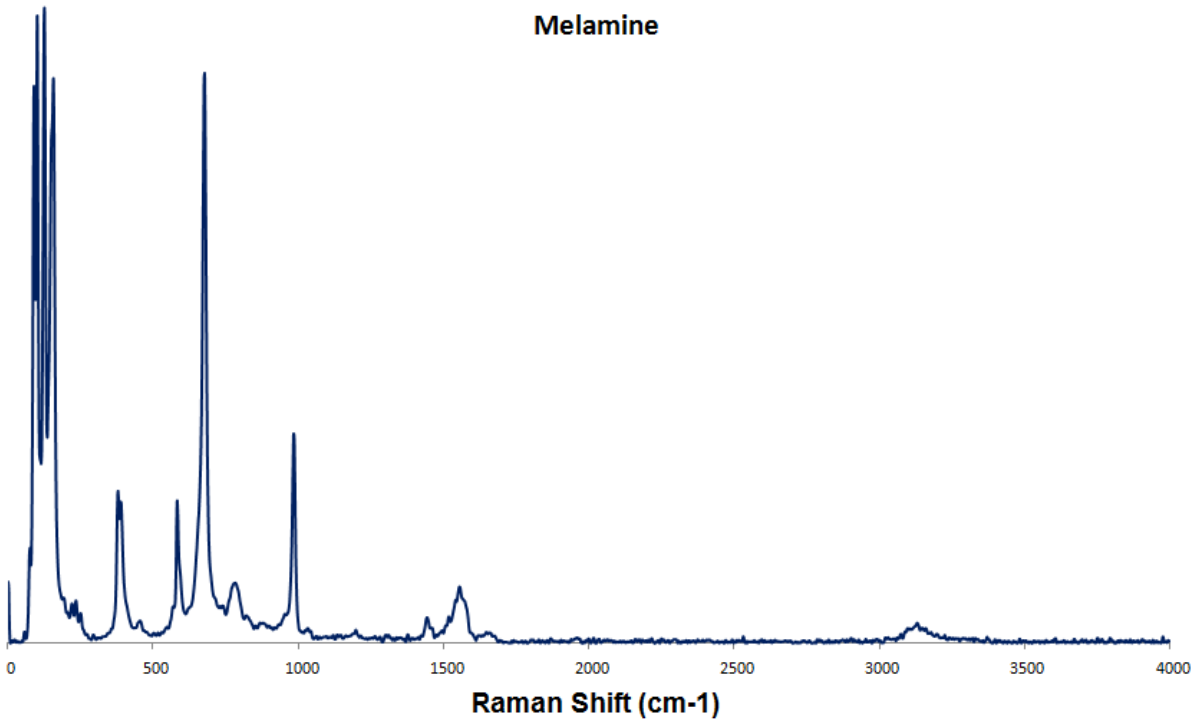

Figure 63. FT Raman spectrum (1064 nm excitation) of melamine.

An important question in this work is why the main C-N stretching vibration observed in the UV Raman spectrum should resemble the broad asymmetric G and D bands of highly disordered graphite or amorphous carbon samples[85-86,91]. The previously discussed X-ray diffraction patterns of the

material appear to indicate that the material is relatively well crystallised at ambient pressures so it is therefore difficult to understand why the material also exhibits an "amorphous" Raman spectrum. One possibility is that it is a feature of the nature of the Raman experiment itself. It is well known that the UV Raman spectra of hydrocarbon materials including solid state and molecular C_xN_y materials can exhibit significant resonance effects[83-88,104]. This effect can greatly enhance the intensity of bands relating to certain vibrational modes within a given spectrum or the contribution of relatively minor species within a sample. The effect is dependent on the local and intermediate range electronic structure and its coupling with the vibrational modes relative to the excitation wavelength. It is known that the π-π* and other electronic transitions in polycyclic aromatic molecules and extended systems including heterocycles are highly dependent on the degree of condensation, with the HOMO-LUMO gap or solid state band gap closing rapidly throughout the UV-visible-IR ranges as the system becomes more extended. Therefore the smaller heterocyclic aromatic units, i.e. the C_3N_3 triazine rings, within a structurally disordered graphitic carbon nitride system would be expected to exhibit the highest intensity in such a UV Raman experiment. It is possible that the $C_6N_9H_3{\cdot}HCl$ material contains a degree of in-plane structural disorder that is not effectively sampled by X-ray diffraction experiments but that does involve electronic and phonon localisation that would give rise to the observed UV Raman effects.

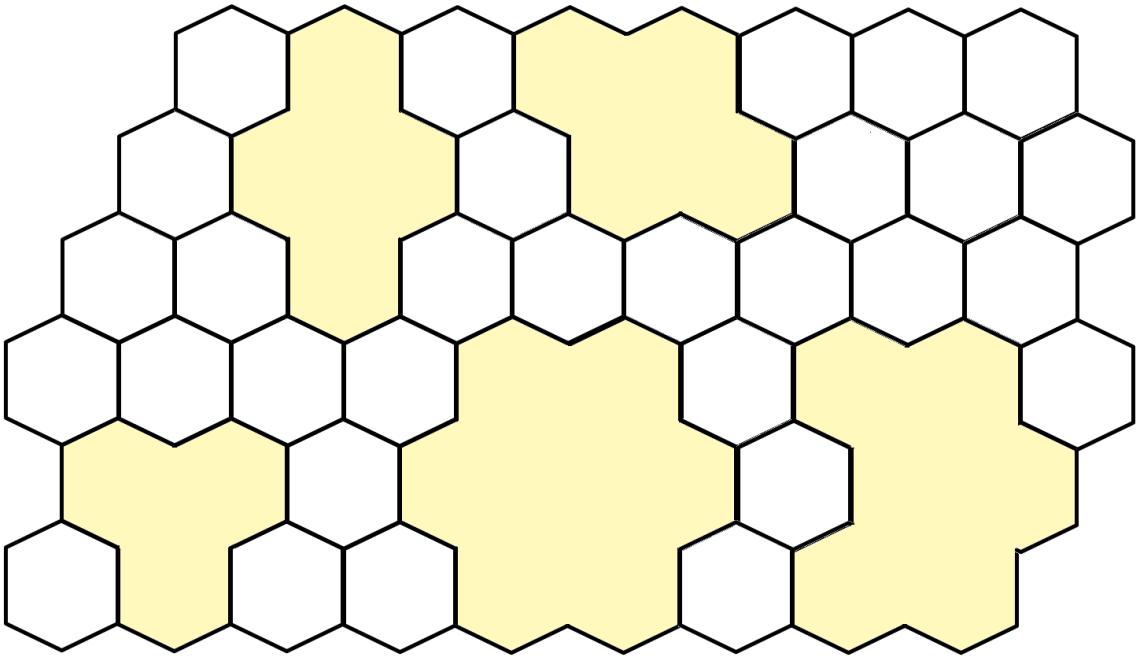

Figure 64. Schematic representation demonstrating the possible random dispersion of voids sizes and locations within the layers of the $C_6N_9H_3$.HCl material. Voids are shown by the shaded areas.

For example it could be that there is some kind of disorder of the size and regularity of the heterocyclic units within the layers of the material so that within a particular layer of the material the distribution of the heterocyclic units and the size of the holes created by them may not be completely uniform. If the distribution of the location and the size of the voids is not uniform within and between the layers this may present some sort of disorder on a level that is not probed by the X-ray diffraction experiments. Figure 64 is a schematic diagram that demonstrates this principle.

After the unexpected results produced by the UV Raman experiments additional studies were carried out using near-IR (1064 nm) excitation in a series of FT-Raman experiments at the CNRS in Orlèans, France. This technique is not expected to cause resonance enhancement and therefore not lead to a specific

excitation of a small proportion of structural species and should give a better average picture of the Raman spectrum of the $C_6N_9H_3$.HCl material. The 1064 nm FT Raman spectra of the material can be seen in figure 65.

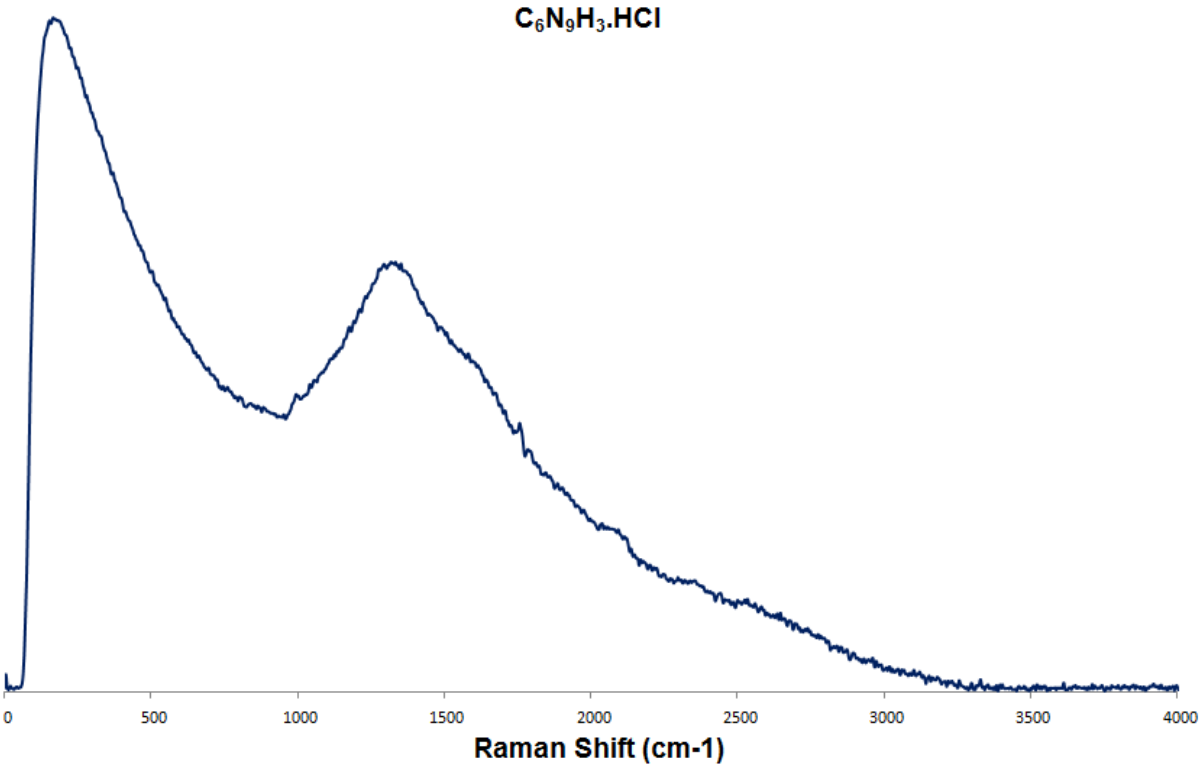

Figure 65. FT Raman spectrum (1064 nm excitation) of $C_6N_9H_3$.HCl performed at CNRS Orlèans, France.

The FT-Raman spectrum shows a broad band in the 1300-1400 cm^{-1} region with shoulders at about 1600 cm^{-1} and 1800-2000 cm^{-1}. These occur in the general range of C-N stretching vibrations expected for condensed phase carbon nitride materials. However they definitely appear to indicate an amorphous or disordered structure. Again the observation of this feature contrasts with the X-ray diffraction results as previously discussed. The peak shape and its maximum differ substantially from those recorded using UV

Raman spectroscopy. This is an indication that the UV Raman results did indeed sample a small fraction of the structural units present in the sample. Ferrari et al. have documented excitation wavelength dispersion among the G and D peaks of amorphous carbons and graphitic carbon nitride materials[83-88]. The main peak frequency is generally expected to move to lower wavenumber with longer excitation wavelength among amorphous carbons and graphitic carbon nitride materials as is seen with these spectra. A very weak feature appears in the FT-Raman spectrum near 980 cm^{-1}, this can be attributed to symmetric stretching of the nitrogens in the C_3N_3 rings incorporated in the structure as described previously. The FT-Raman spectrum also shows a broad feature rising up at low frequency, it is cut off by the bandpass filter at 60 cm^{-1}. Figure 67 shows this feature as it goes over into negative Raman shift. The intensity of the band relative to the high frequency Raman bands can be seen as the 'anti-stokes' version of the 'Stokes' bands seen in the positive Raman shift region; this can be better seen in figure 66.

These experiments were followed up by a series of experiments on the same materials using a similar system in Nottingham, England. This was to ensure the continuity and reproducibility of the results and confirm that the large broad features seen in the Raman spectrum were in fact due to the sample under study and not a feature of some malfunction of the setup in Orlèans as had been suspected by a local technician. As can be seen in figure 66 the two sets of spectra are almost identical and there are no features of significance differing between them. The collection of bands in the 2000-2500 cm^{-1} region are a consequence of the spectrum from Orlèans being conducted under vacuum and the Nottingham data being recorded in air. This part of the spectrum in the

Nottingham data is due the presence of air in the sample chamber when the measurements were being taken.

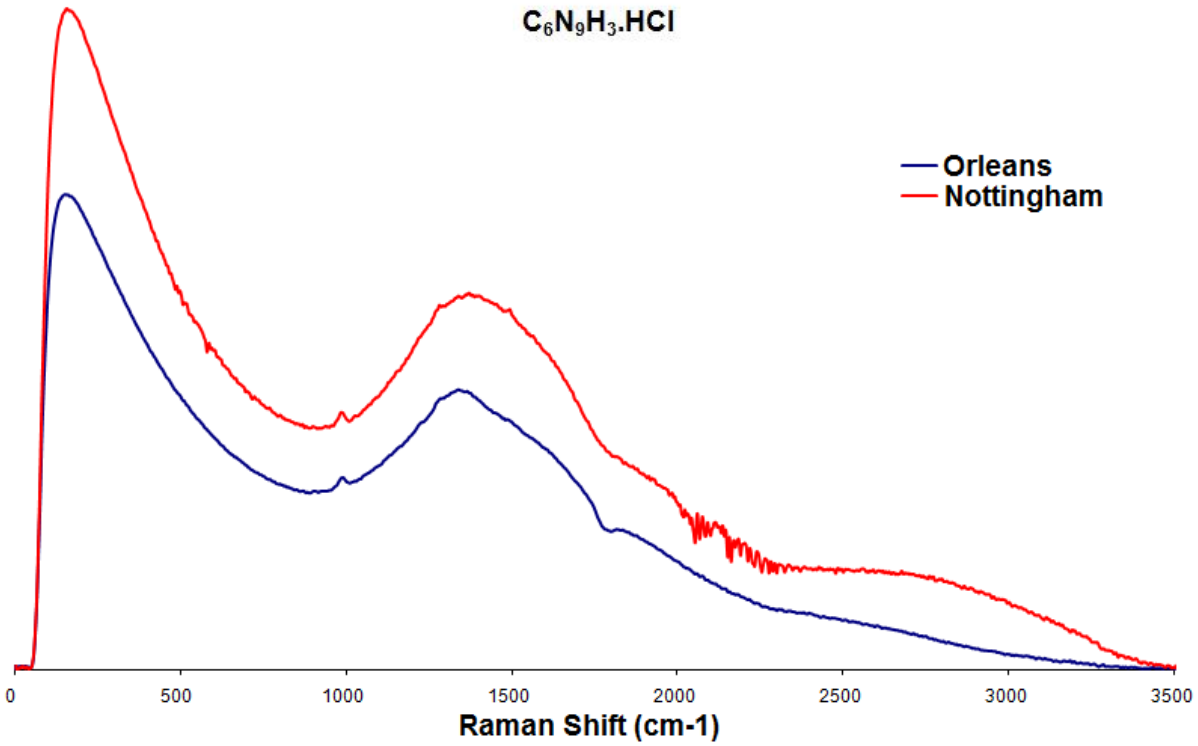

Figure 66. FT Raman spectrum (1064 nm excitation) of $C_6N_9H_3$.HCl performed at CNRS Orlèans, France compared with that taken in Nottingham, England.

4.4 Low Temperature FT-Raman

Due to the nature of the spectra that resulted from the 1064 nm excitation FT-Raman spectra, i.e. it being very broad, it was possible that that this could be again due to fluorescence. Therefore the 1064 nm excitation FT-Raman measurements were repeated at low temperature to ascertain whether the origin of the broad features is due to vibrational or fluorescence/electronic effects. Figure 67 shows the 1064 nm FT-Raman spectrum of $C_6N_9H_3$.HCl at ambient (300 K) and low (80 K) temperature. The low temperature data confirms that

the band has a vibrational origin in the low frequency region. In figure 67 both the Stokes and anti-Stokes components of the spectra can be seen, this indicates that the broad nature of the peaks is not a fluorescence feature as this 'mirror image' effect characteristic of the Stokes/anti-Stokes nature of the Raman experiment can be seen. When the ambient and low temperature spectra are compared a change in the relative intensities of the of the Stokes and anti-Stokes features is observed. This is a temperature dependent process because it depends on the population of the ground state, which will increase as the temperature decreases. Therefore it is likely that the features in the spectra are due to vibrational effects rather than fluorescence as this is not temperature dependent. This behaviour is normally only activated in amorphous solid materials[104-107]. Again this poses the question as to why a material that displays such a feature normally associated with amorphous or disordered vibrations should appear in the FT-Raman spectrum of $C_6N_9H_3$.HCl when the material is apparently crystalline in nature according to other characterisation methods. It is possible that the $C_{12}N_{12}$ voids and the C_3N_3 rings in the structure may be distributed in a random manner resulting in the 'amorphous' propagation of phonons within the layers.

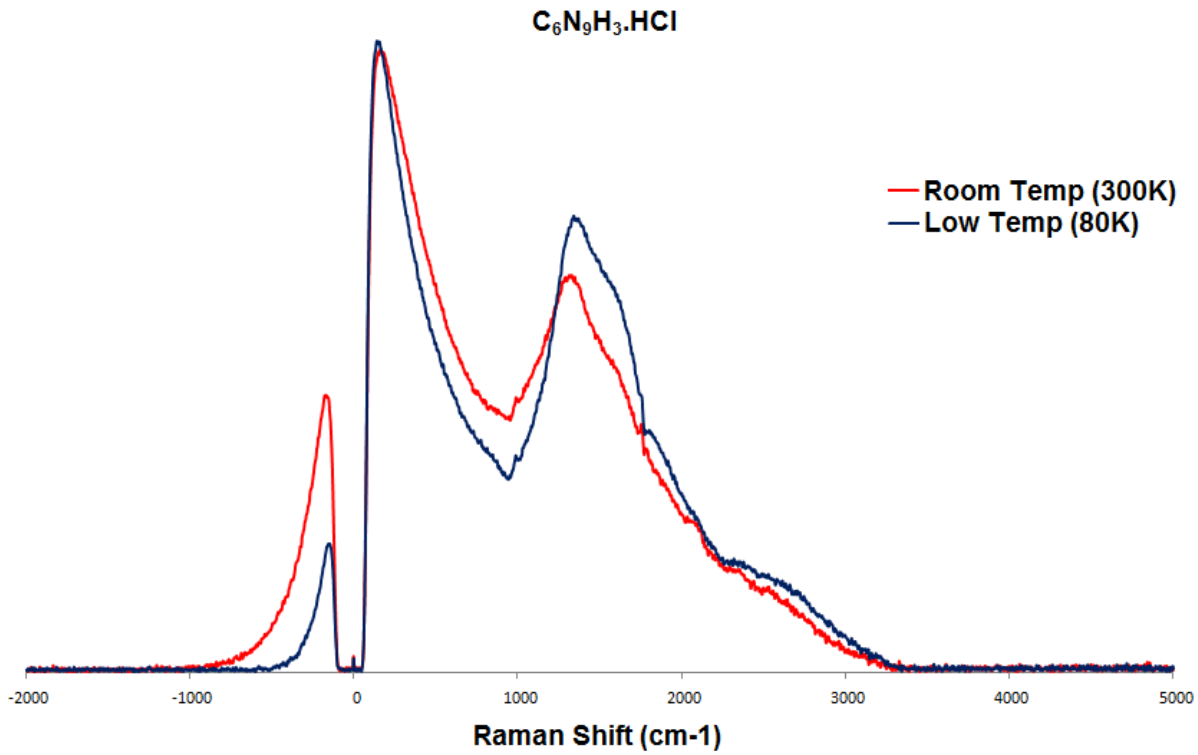

Figure 67. FT Raman spectrum (1064 nm excitation) of $C_6N_9H_3$.HCl performed at CNRS Orlèans, France comparing the low and high temperature measurements.

4.5 Tholin Materials and Comparisons

'Tholins' are hydrogenated carbon nitride materials that are produced from mixtures of N_2 and CH_4 gasses under cold plasma discharge conditions. It is thought that this process simulates the composition and conditions of the aerosols found in the atmosphere of the planet Titan which is a moon of Saturn[99,108-109]. During the course of this work collaborations were made with a group at the Laboratory of Planetology at Université Joseph Fourier in Grenoble, France where these materials are produced and studied. It was found that certain features seen in the IR and Raman spectra of some of the Tholin materials were comparable to features observed for the carbon nitride material studied here. As with the $C_6N_9H_3 \cdot HCl$ material the tholins are found to fluoresce strongly when

excited using visible radiation. Similarly it was found that the use of excitation wavelengths between 458 and 785 nm could not obtain useful Raman spectra due to fluorescence and the experiments using 1064 nm FT-Raman also presented broad features. It was also found that these materials did produce a useful Raman spectrum when excited in the UV. Studies of these materials in conjunction with the $C_6N_9H_3{\cdot}HCl$ material led to the assignment of several common features in the spectra of the two materials. Figure 68 shows a comparison of several tholin materials with the $C_6N_9H_3{\cdot}HCl$ material and the standards *s*-triazine (C_3N_3) and melamine. The UV-Raman spectra of the tholins and the $C_6N_9H_3{\cdot}HCl$ material are strikingly similar and are dominated by broad bands in the 1200-1700 cm^{-1} region that again appear analogous to the D and G bands observed for disordered carbon-based graphitic materials[82-86]. The breathing modes of the triazine ring marked A_1 and A_2 at around 690 and 980 cm^{-1} respectively can be identified in the tholin materials

Again, due to the nature of the UV-Raman experiment, it is likely that these features are resonantly enhanced in the spectrum; some of the tholin materials do not display the peaks associated with the triazine ring anywhere near as intensely as in $C_6N_9H_3{\cdot}HCl$ or some of the other tholin materials, this indicates that there is much less of a triazine ring component to these materials. The features labeled C_1 and C_2 at 2180 and 2225 cm^{-1} respectively are likely to be due to features of a –NC component in the material that is not present in $C_6N_9H_3{\cdot}HCl$ as was shown by the lack of a corresponding feature on the IR spectra of the material.

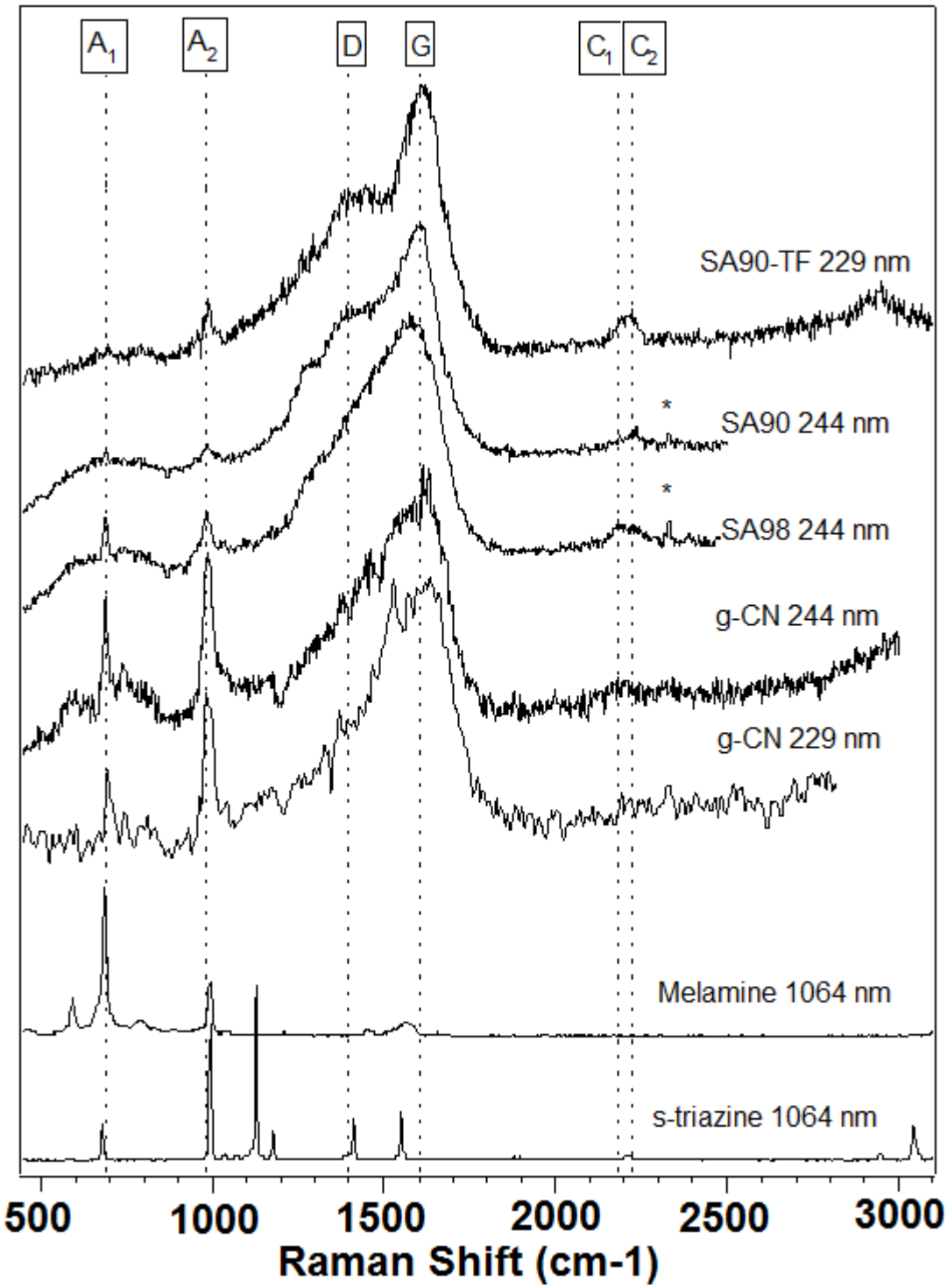

Figure 68. Comparison of the UV Raman spectra of a selection of tholin materials with different preparation compositions and $C_6N_9H_3 \cdot HCl$ along with the standards traizine and melamine.

4.6 Conclusions

The structure of the $C_6N_9H_3{\cdot}HCl$ material has been investigated by visible, UV and near IR excitation FT-Raman spectroscopy. Previous attempts at obtaining conventional Raman spectra using visible excitations have been unsuccessful due to the strong fluorescence the sample exhibits under these conditions. The UV Raman spectrum for the sample exhibits a strong, broad asymmetric feature similar to that seen for amorphous carbon and highly disordered graphitic carbon structures. Sharp peaks are observed at lower wavenumbers and are likely to be due to symmetric stretching vibrations of the C_3N_3 triazine rings in the $C_6N_9H_3{\cdot}HCl$ material. It is possible that the UV Raman spectra are dominated by resonance Raman effects meaning that the observed spectra could represent only a small fraction of the structural species present in the sample.

FT-Raman spectra of the $C_6N_9H_3{\cdot}HCl$ material using near IR excitation of 1064 nm was also obtained, this was performed at both ambient and low temperatures to further examine the possibility of resonance effects occurring. In these spectra the main Raman band moved to lower wavenumber but remained broad. These results indicate either that disorder occurs within the carbon nitride graphitic layers which could be correlated with disordering in the linkage formation between the C_3N_3 triazine rings and resulting in a dispersion in the void sizes within the layers, or that the electron-phonon coupling effects result in extreme broadening of the Raman active modes upon excitation across a wide range of the optical spectrum.

The comparison between the UV Raman spectra of the $C_6N_9H_3 \cdot HCl$ material and the ‘tholins’ sheds a bit more ‘light’ on the nature of both the tholins and the carbon nitride material produced in this work.

Chapter Five – Structural behaviour of $C_6N_9H_3$.HCl at High Pressure

5.1 Introduction

The synthesis and characterisation of the layered graphitic compound $C_6N_9H_3 \cdot HCl$ has been presented in the previous two chapters. In this section we describe the structural changes that occur in this material under extreme densification, at pressures of up to 60 GPa. These studies were carried out in the diamond anvil cell using synchrotron angle dispersive X-ray diffraction at the SRS to probe the structural changes. Some preliminary complementary experiments were also carried out using FTIR spectroscopy in the diamond anvil cell however these were limited to around 8 GPa due to limitations of the available diamonds.

The experimental studies were combined with theoretical investigations carried out by Malek Deifallah, a UCL PhD student working with Dr. Furio Cora in the Davy-Faraday Research Laboratory at the Royal Institution and then at UCL. The theoretical results provide a possible model for understanding the structural changes observed experimentally.

5.2 Experimental High-Pressure Behaviour of $C_6N_9H_3$.HCl

The structural behaviour of the layered *g*-$C_6N_9H_3 \cdot x$HCl material during compression to p ~ 60 GPa was investigated using angle dispersive synchrotron X-ray diffraction in the diamond anvil cell. Angle dispersive X-ray diffraction experiments were carried out using monochromatic synchrotron radiation (λ = 0.44397Å) at station 9.5HPT at the Synchrotron Radiation Source in Daresbury, UK. Several experimental runs at the facility contributed to the data presented. Both screw-driven cylindrical Mao-type cells built at UCL and membrane-driven (Diacell, UK) diamond anvil cells were used for the experiments. All diamonds used were cut with 300 µm culets, and small piece of rhenium foil indented to ~ 30 µm thickness was used as a gasket with holes of between 160 µm and 80 µm in diameter drilled into the centre to provide the sample chamber. The larger holes were used in earlier experiments where the low to moderate part of the pressure range studied was attained and the size being decreased for later experiments where the maximum target pressure was higher. Ruby chips placed inside the sample chamber of the cell were used for pressure determination. The samples were loaded into the cells with no pressure-transmitting medium. This is because of the tendency of most common pressure transmitting media to interfere with the diffraction pattern of the actual sample material. Therefore no cryogenic loading with N_2/Ar could be carried out, and other fluid media such as MeOH/EtOH crystallise at too low a pressure to be compatible with the experimental range under investigation. Attempts made to conduct experiments using such a medium were abandoned as it was not possible to obtain useful data in this way. Due to the poorly scattering nature of the material under study and its tendency to undergo loss of order and possible

amorphisation, as will be discussed in more detail later, the crystallisation of a pressure medium surrounding the sample proved to overpower the weak diffraction pattern of the material itself. Similarly a solid pressure transmitting medium such as NaCl or CsI would also severely affect the resulting diffraction pattern; also being crystalline solids even at the lowest experimental pressures would negate any benefit of increased hydrostaticity that can be offered by some liquid pressure transmitting mediums. The addition of a pressure transmitting medium would also reduce the intensity of the diffraction pattern acquired, by reducing the available volume of actual sample exposed to the X-ray beam of such a weakly scattering material. As the solid sample material is quite soft and packs easily into the sample chamber it was therefore considered most beneficial to fill the sample chamber with material.

The structural behaviour of the layered carbon nitride material and how it evolves under applied pressure will now be discussed. As can be seen in Figure 69 the low pressure synchrotron X-ray diffraction patterns of $C_6N_9H_3{\cdot}HCl$ compare very well to the ambient pressure patterns obtained on the laboratory diffractometer. These have already been presented previously and are shown here again for completeness. The difference in the position and broadening of the peaks is due to the slight difference in pressure between the two patterns, as it is not possible to load a sample in a diamond cell without exerting any pressure on it at all. Note the relatively large shift in the main diffraction peaks at quite a low pressure; this indicates the very high compressibility of the material at low pressure.

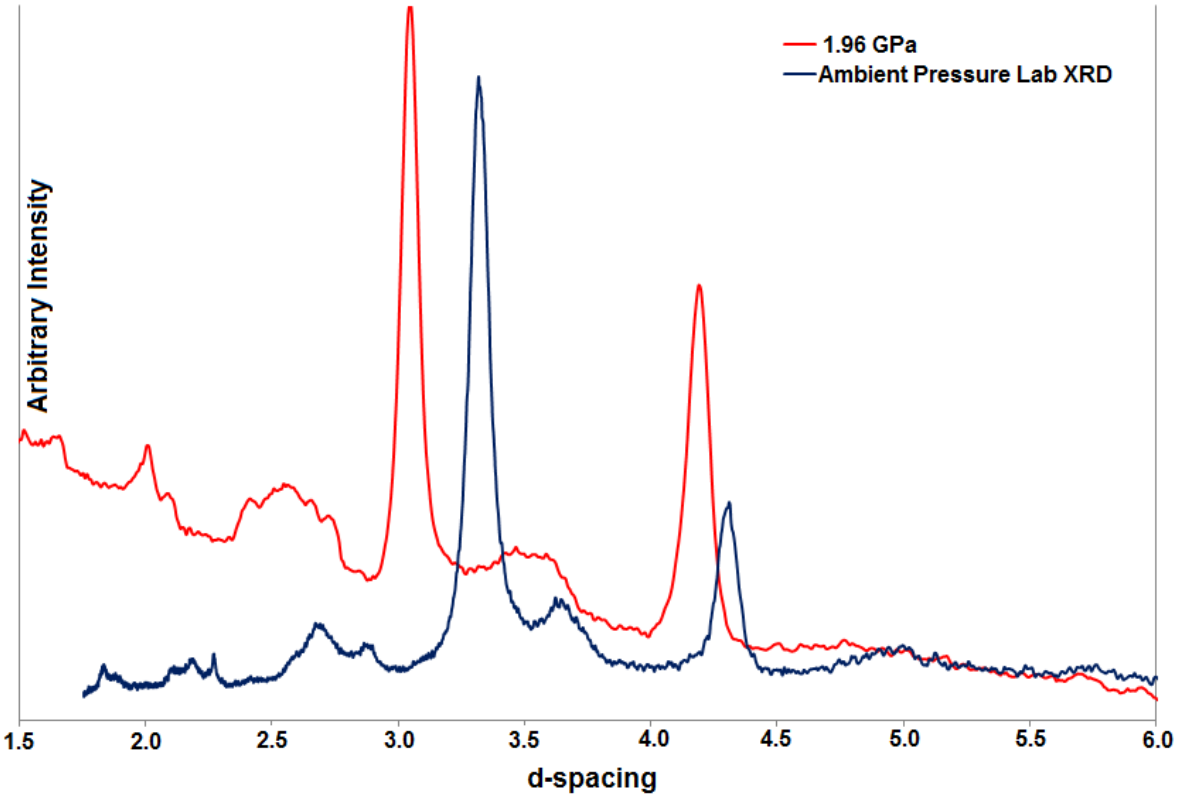

Figure 69. X-ray diffraction patterns of the $C_6N_9H_3$.HCl material at ambient pressure measured in the laboratory (blue) compared with the synchrotron X-ray diffraction pattern in the diamond anvil cell at 1.96 GPa (red).

Figure 70 displays a collection of diffraction patterns as pressure is applied to the material over a range of 1-60 GPa. The analysis yields valuable information about the changes in the lattice parameters; in particular it was possible to monitor the position of the 110 and 002 reflections (which are the most intense peaks), and these have been used to calculate the *a* and *c* lattice parameters as a function of pressure. Upon initial compression, the crystalline diffraction peaks of the *g*-$C_6N_9H_3$·HCl phase remain clearly visible up to p ~ 25-30 GPa: analysis of the data yields information about the relative changes in the *a* and *c* lattice parameters, as discussed previously by Wolf et al[45].

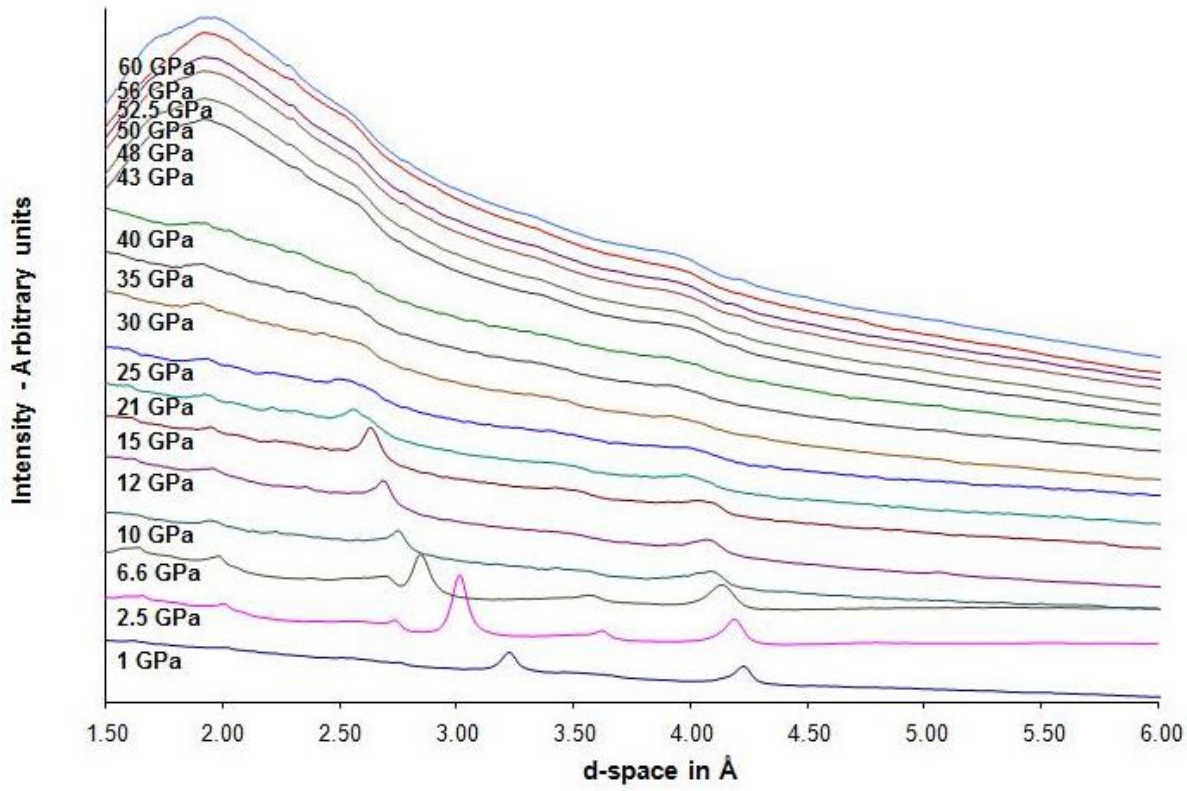

Figure 70. XRD patterns of the $C_6N_9H_3 \cdot x$HCl material under compression in the diamond anvil cell in the pressure range 1-60GPa.

As would be expected, when pressure is applied to the material the unit cell parameters change accordingly in reaction to the compression. The 110 and 002 peaks in the diffraction pattern were monitored as pressure was applied. Figure 73 shows how the X-ray diffraction data during the compression can be indexed. The *d*-spacing value in angstroms for each peak can be followed and has been recorded and tabulated in table 4.

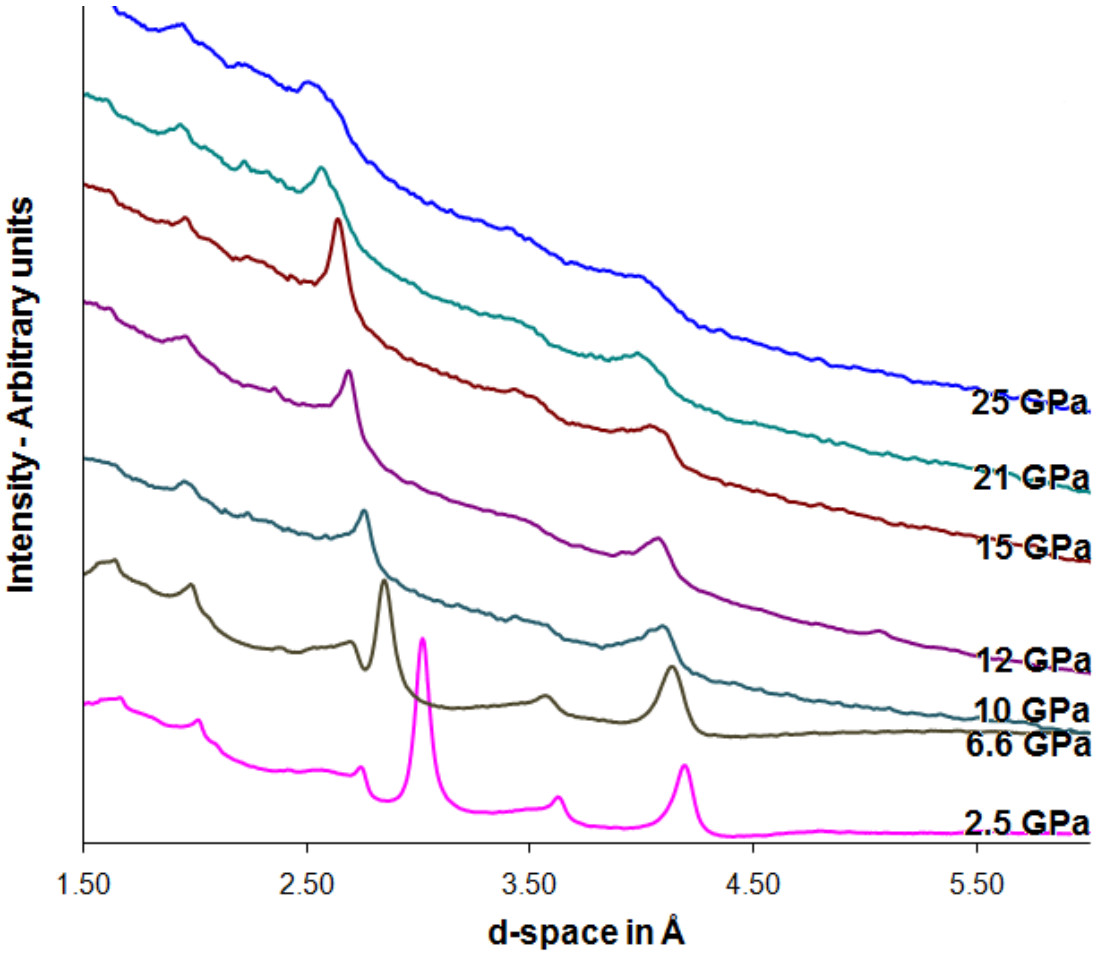

Figure 71. Experimental XRD data for pressures 2.5–25 GPa.

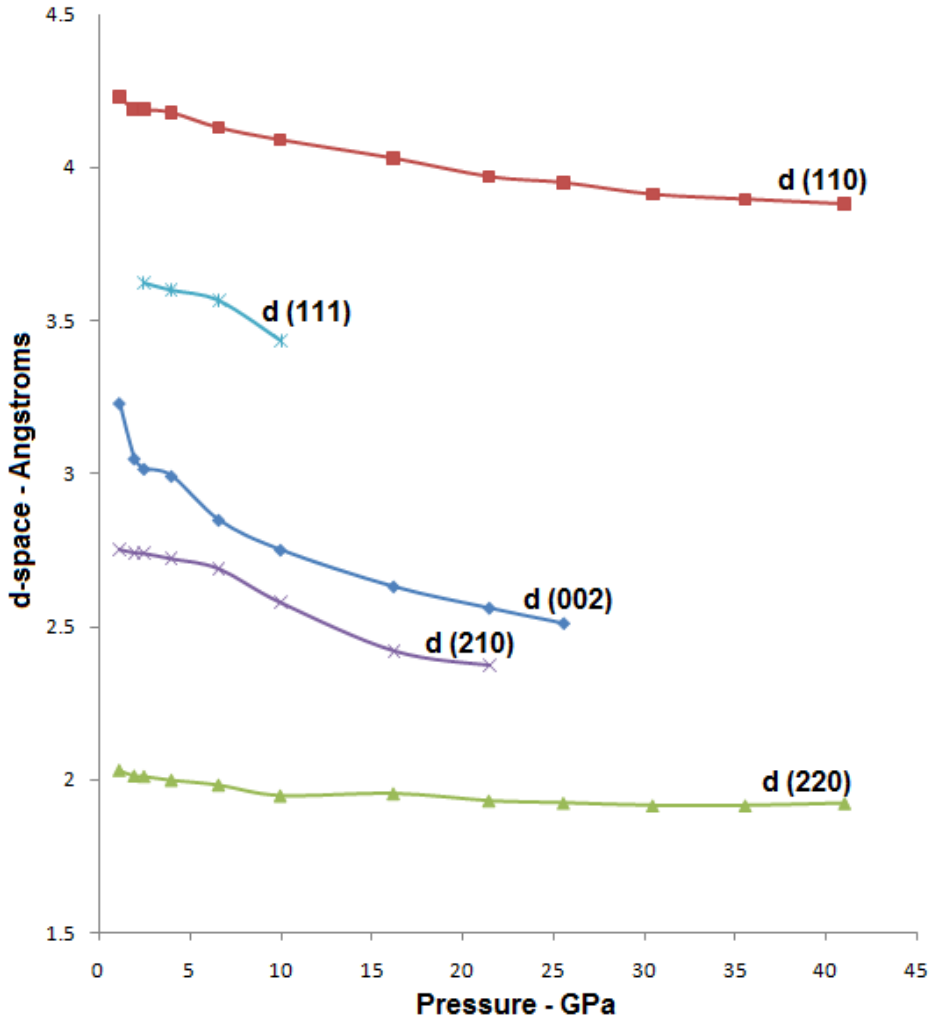

Figure 72. Change in *d*-spacing of the reflections as pressure is increased.

Pressure (GPa)	*d* (002) (Å)	*C* (Å)	*d* (110) (Å)	*a* (Å)
1.14	3.23	6.46	4.23	8.46
2.50	3.02	6.03	4.19	8.38
6.60	2.85	5.70	4.13	8.26
10.00	2.75	5.50	4.09	8.18
12.70	2.69	5.38	4.07	8.14
16.23	2.63	5.26	4.03	8.06
21.49	2.56	5.12	3.97	7.94
25.59	2.51	5.02	3.95	7.90
30.50			3.91	7.82
35.60			3.90	7.79
41.08			3.80	7.61

Table 4. Table of *d*-spacings of the 002 and 110 reflections as pressure increases with the values of the *a* and *c* calculated from these figures.

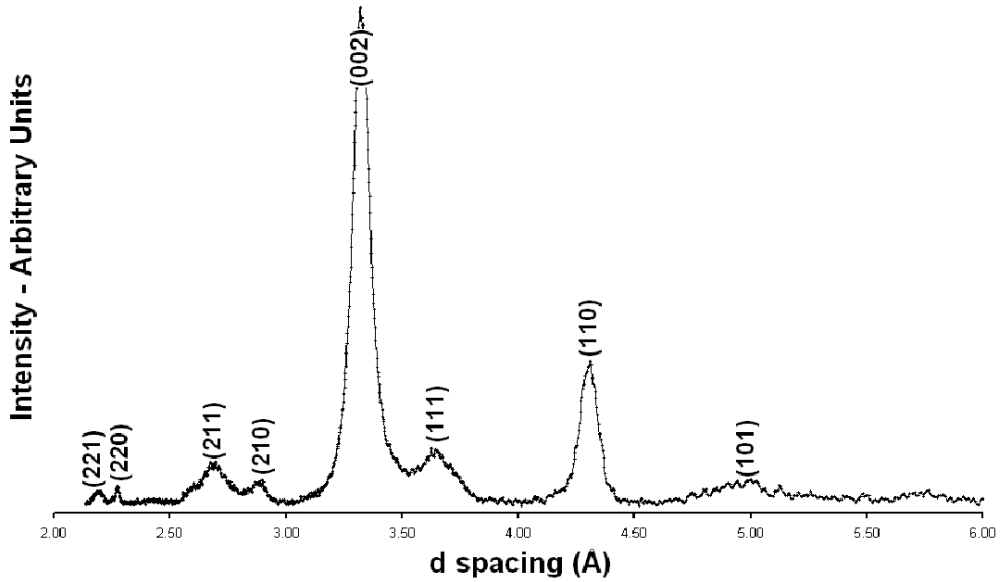

Figure 73. Laboratory X-ray diffraction pattern of the synthesised $C_6N_9H_3HCl$ material at ambient pressure.

Analysis of the dependence of the parameters *a* and *c* on pressure indicates that the material behaves highly anisotropically, as would be expected for a layered material of this nature. That is, the material is much more compressible in the *c* direction than in the *a* direction. This is evidenced by the change in the *c* parameter being much more pronounced than that for *a* (where *a* = *b*) (figure 74). The *c* axis of the unit cell is the one that encompasses the interlayer spacing of the material therefore there is more scope for contraction in this direction to relieve to compressive strain imposed on the material than in the *a* direction which involves contraction within the layers. This is illustrated in figure 75 showing the orientations of the unit cell lengths in relation to the layers in the material. The data are consistent for that of a layered solid. If the material possessed a more symmetrical continuous three dimensional framework structure it would have a similar compressibility in all directions.

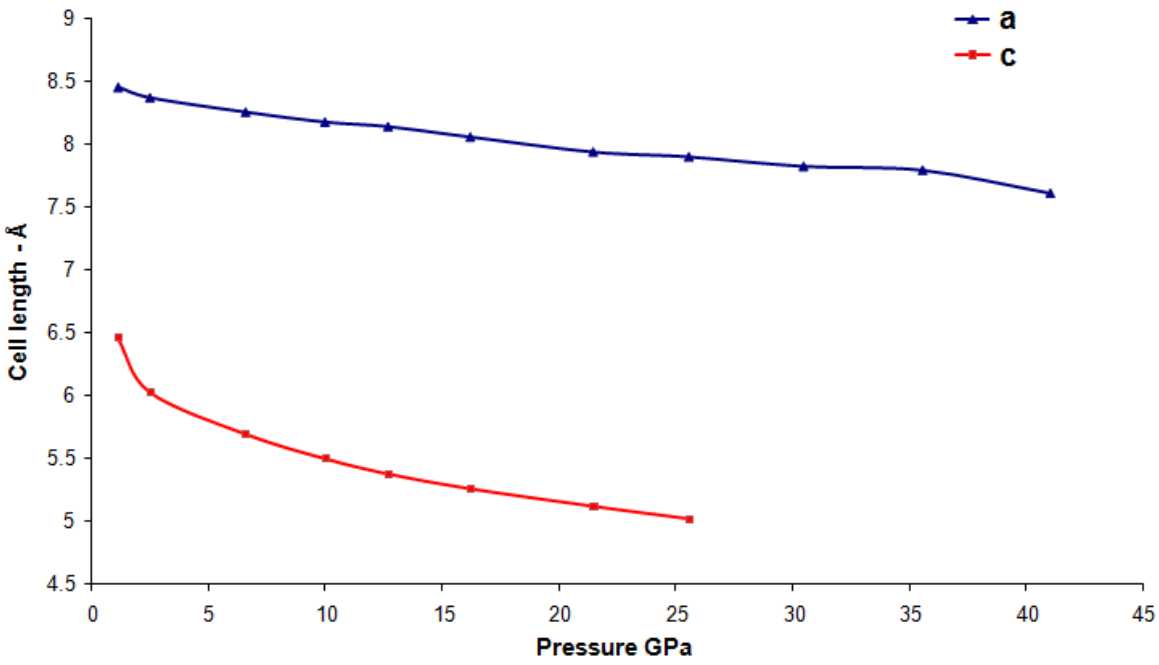

Figure 74. Change in cell parameters *a* and *c* on compression, determined experimentally.

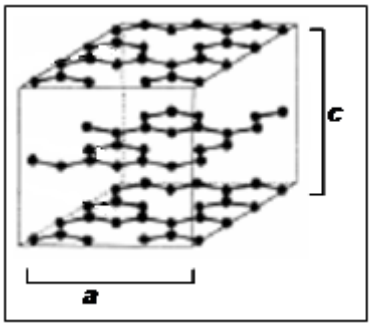

Figure 75. Schematic diagram of unit cell parameters in the $C_6N_9H_3HCl$ material at ambient pressure.

As further pressure is applied to the material, the diffraction pattern begins to broaden and flatten out until it is no longer possible to resolve any peaks and an apparent amorphisation appears to occur by ~35 GPa. At these pressures we were only able to resolve the 002 reflection up to a pressure of 25 GPa; above this it is lost. It is however possible to follow the 110 reflection to a

higher pressure of 35 GPa but not above this value of P. It is therefore not possible to deduce the lattice parameters above 35 GPa from this data.

In the range where it is possible to follow the change of both *a* and *c* cell parameters, the experimental data show that there is a sharp decrease in the value of *c* and a less marked decrease in *a*: on pressurisation, the *c* parameter drops from 6.43 Å at 1 GPa to 5.02 Å at 25 GPa, a change of 22%, while *a* goes from 8.45 Å to 7.90 Å over the same pressure range, with a change of only 6.5%. It is interesting to note that during the experimental compression the value of *c* drops to 5 Å while it is still possible to clearly resolve the 002 reflection that directly relates to that lattice parameter. This could be an early indication of the onset of a structural change within the graphitic layered material, and may be associated with sp^2 to sp^3 rehybridisation occurring within the bridging C-N bonds, which will be discussed in more detail later. The change of unit cell volume observed experimentally in the 1-25 GPa range is 32%, which is surprisingly large. The emergence of a plateau-like feature in the diffraction pattern above 30 GPa (figure 76) indicates severe structural disorder occurring within the material at these pressures, supporting the observation that a high degree of structural change or rearrangement has occurred.

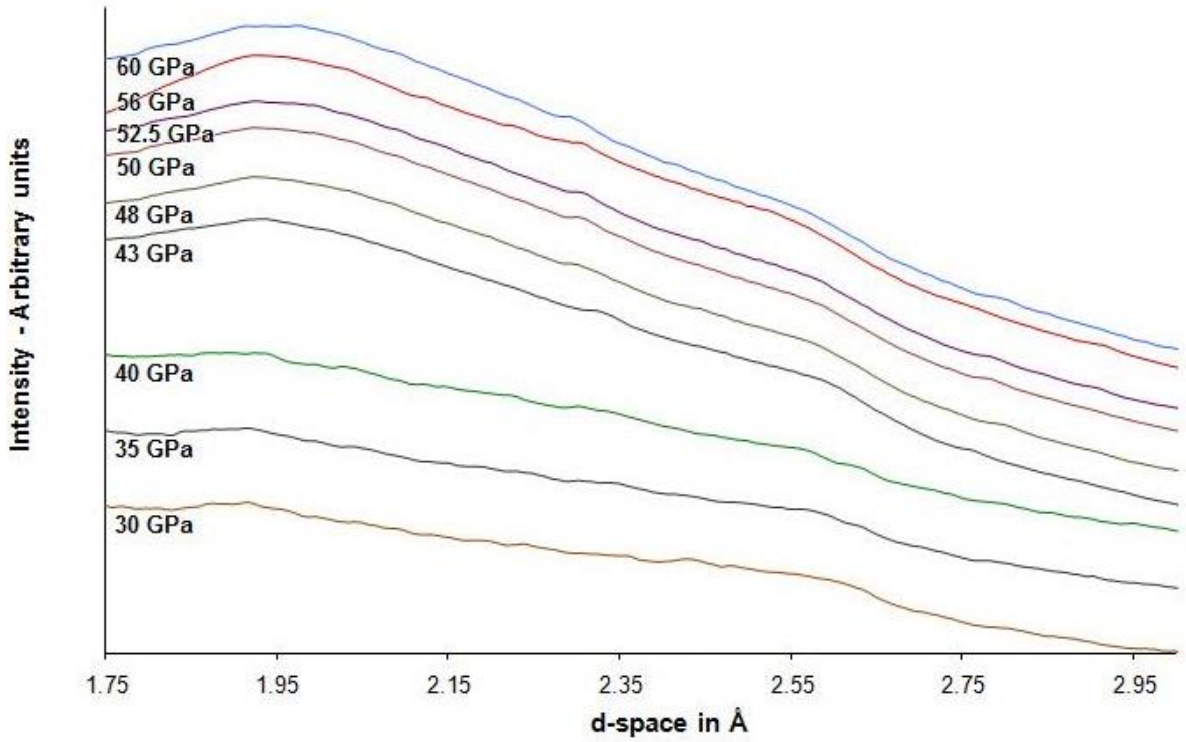

Figure 76. A close-up view of the 1.75–3.00 Å region of the experimental XRD data of the $C_6N_9H_3HCl$ material pressures 30–60 GPa.

Experimental diffraction data were obtained for pressures up to 60 GPa. No new diffraction peaks appeared in the XRD patterns; between 25-35 GPa the material appears to undergo a loss of structural order upon compression, whereas above 35 GPa it appears to have undergone pressure-induced amorphisation. This is further supported by appearance of the diffraction rings in the raw two-dimensional diffraction images obtained. The gradual diffusion and loss of the diffraction rings can be seen in figure 77. As the pressure is increased the sharp rings characterising reflections from planes in the crystal broaden out and become more diffuse until one faint, very broad ‘halo’ type ring is observed above 40 GPa. This could be an indication that the structure of the material is no longer ordered over the short range probed by X-ray diffraction and that some amorphisation or major structural change has begun within the material.

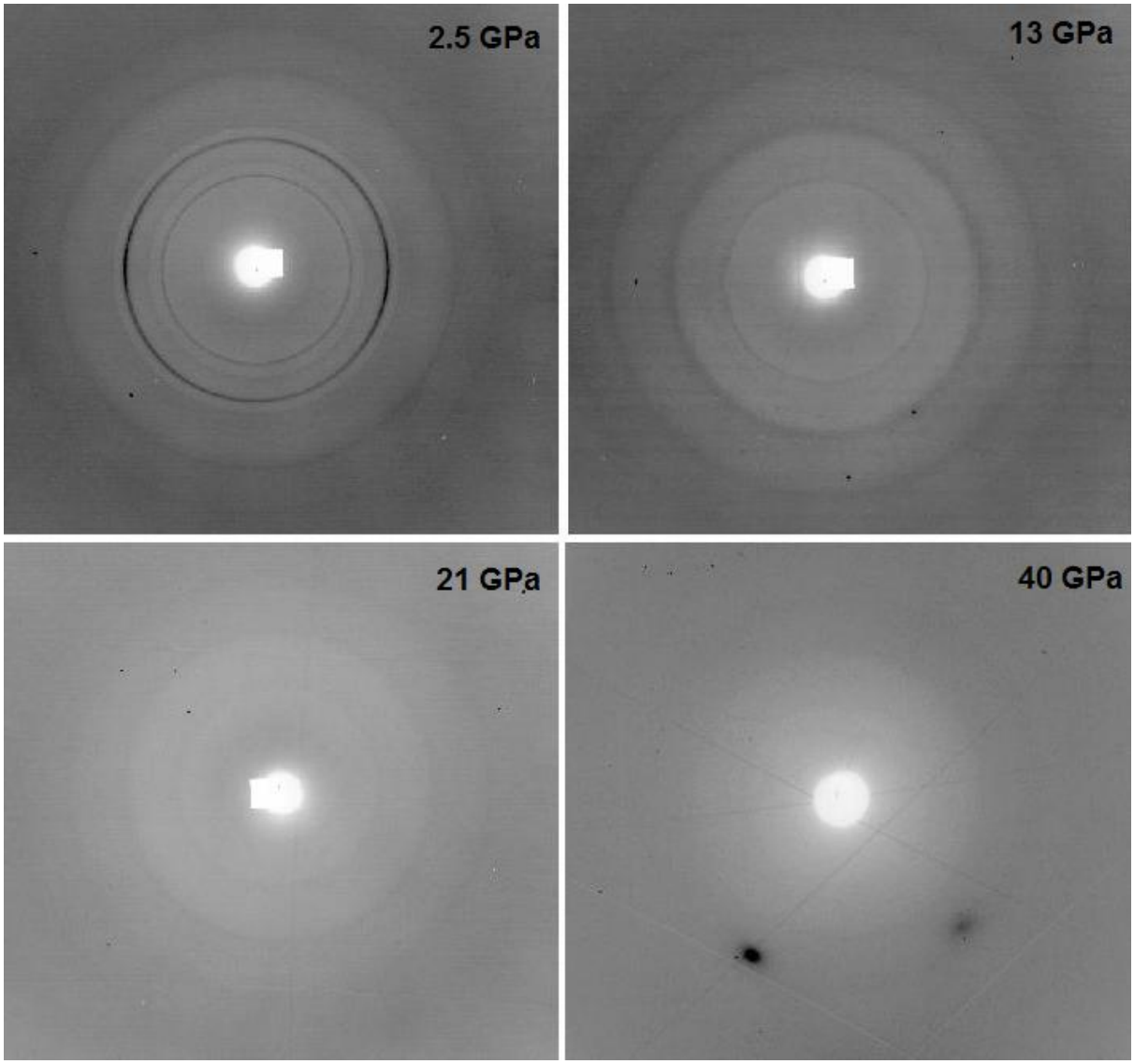

Figure 77. X-ray diffraction ring images of the material for various pressures.

As highlighted previously it is only possible to resolve the 002 reflection, which relates to the *c* direction of the unit cell and the inter layer spacing of the material, up to a pressure of 25 GPa. However the 110 reflection, relating to the *a* parameter of the unit cell and the in plane direction of the layers, is observable up to more than 35 GPa. A possible explanation of this phenomenon is that as the pressure applied to the material is increased the layers come closer and closer together, as indicated by the reduction in the value of *c* on increasing

pressure. There will come a point when the layers are so close together that it is not possible for the distance to reduce any further to relieve the compressive strain generated within the material. At this point it is possible that there is zero distance between the layers. In this case the *c* lattice parameter in the unit cell would be affected and therefore it explains why it is no longer possible to resolve the 002 reflection in the diffraction pattern. One possibility is that the layers become so close that bonds starts to form between the layers. This interlayer boding could be manifested in the re-hybridisation of carbon atoms from sp^2 to sp^3 and be the beginning stages in the conversion of the material to a more dense three-dimensional structure. The *a* lattice parameter would not be affected in the same way as the *c* parameter as the material is likely to be stronger across the layers due to its planar network structure. This is a reasonable explanation for why the 110 reflection is observable to a higher pressure than the 002. The apparent loss of structural order in the material could be an indication of the onset of a more dense phase akin to those predicted and discussed previously[16-21].

The results obtained in this work compare well to those presented previously by Wolf et. al.[45] Considering that the previous results were obtained using energy dispersive X-ray diffraction and a neon pressure medium was used in the experiments it is possible that more information can be gained about the structure of the material from this study as it is possible to resolve more reflections to a higher pressure.

5.3 Comparison of Experimental and Computational High Pressure Behaviour of $C_6N_9H_3$.HCl

The computational work discussed in the previous chapter for the ambient pressure structure was extended to consider the effects of hydrostatic pressurisation on the layered graphitic C,N structures, with the goals of assisting the interpretation of experimental results, and identifying possible atomic level mechanisms responsible for the observed behaviour.

Theoretical calculations of various $C_6N_9H_3$ and $C_6N_9H_3$.HCl layered materials and graphitic compounds were carried out using periodic boundary conditions within the local density approximation (LDA) of density functional theory (DFT) using the plane wave code CASTEP[91,110]. Ultra-soft pseudopotentials for C, N, H and Cl atoms were used and the cut-off energy (450eV) and k-point grid size (3x3x4) was optimised from single energy point calculations. Further details of the calculations are presented elsewhere[91,110].

The theoretical studies examined the response to increasing pressure of both the $C_6N_9H_3$.HCl and $C_6N_9H_3$ compositions for a pressure range of 0-100 GPa. As for the ambient pressure data the calculations were performed in the *P1* space group to ensure that there were no symmetry constraints on the evolution of the structure.

The $C_6N_9H_3$ structure was the first system to be examined, figure 78 shows the calculated cell parameters (*a*, *b* and *c*) as a function of pressure applied. Two discontinuities are observed for the $C_6N_9H_3$ material at 50 and 90 GPa. Therefore the following discussion is divided into the following pressure ranges; 0-40 GPa, 50-85 GPa and > 90 GPa.

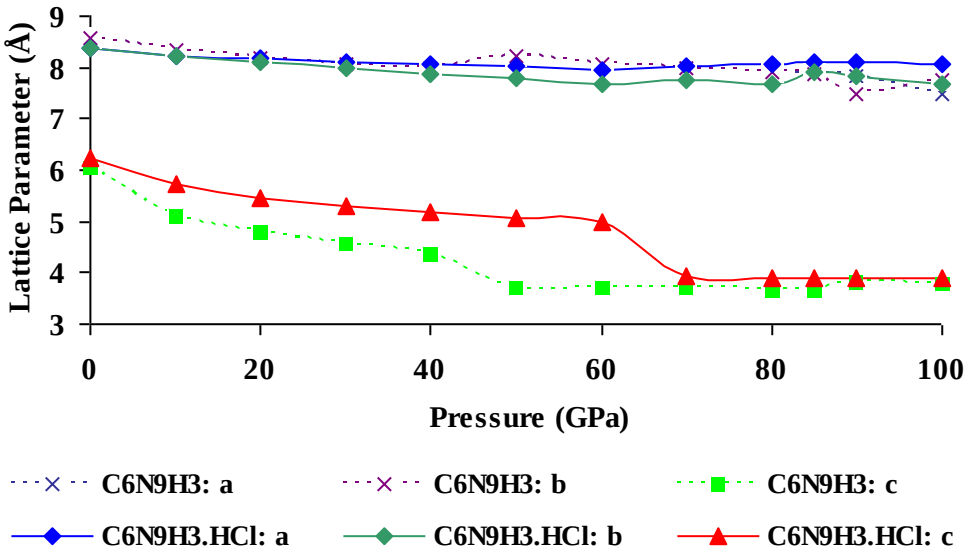

Figure 78. Equilibrium lattice parameters of *g*-$C_6N_9H_3$ and *g*-$C_6N_9H_3$·HCl as a function of pressure from the computational work.

In the 0-40 GPa pressure range no rearrangement is observed in the calculated high pressure structures compared with the ambient pressure one. As seen with the experimental data the calculated material also displays a highly anisotropic change in the lattice parameters under compression. The compressibility along the *c* axis is far greater than in the *a* (and *b*) directions. At 40 GPa, the *c* lattice parameter equals 4.367 Å, a reduction of 28% with respect to the value of 6.039 Å at p = 0; the corresponding change in *a* is of 6.7%, from 8.565 Å to 7.995 Å, resulting in a 37% drop in unit cell volume (figure 78). These values compare very well with the experimental results discussed earlier in the range of 0-25 GPa in which the material retains its crystalline features in the XRD patterns. It is important to notice that the small interlayer separation of 2.18 Å has been obtained without formation of any interlayer bonding feature between adjacent layers.

The geometry of the $C_6N_9H_3$ layer at ambient pressure was found to be atomically flat; this feature is retained throughout the 0-40 GPa compression range. Figure 79 shows the values of two dihedral angles within the calculated $C_6N_9H_3$ structure as a function of pressure. These are the internal dihedral angles of the triazine rings that overlap each other in the unit cell (A-B-C-D in the figure) and the dihedral angle across a bridging NH group (A-B-E-F in the figure). Both values are zero for an atomically flat layer, and as we can see in figure 79, this condition is satisfied in the entire range of pressure up to 40 GPa.

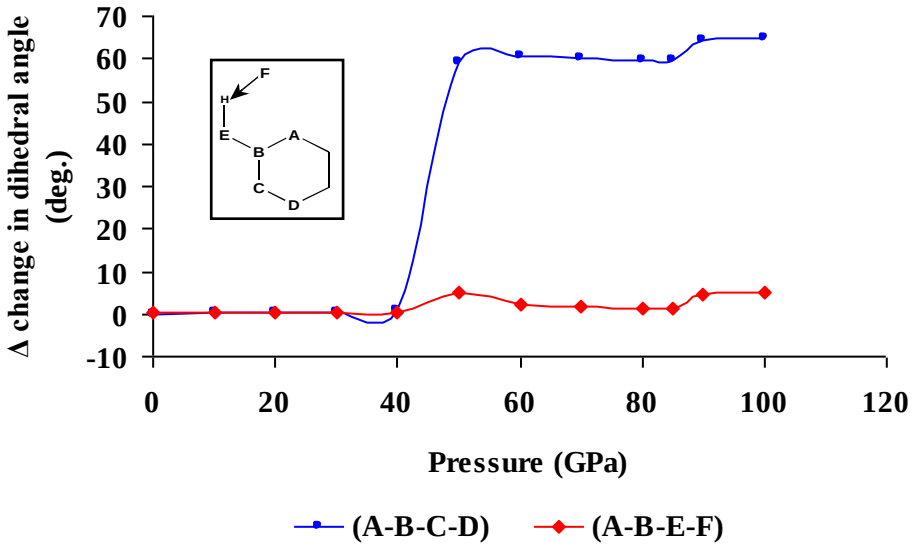

Figure 79. Dihedral angles in the equilibrium geometry of *g*-$C_6N_9H_3$ as a function of p: A-B-C-D is the internal dihedral angle of triazine rings that overlap each other in the unit cell and A-B-E-F is the dihedral angle across a bridging NH group.

In an earlier work considering only single layer *g*-$C_6N_9H_3$ by Deifallah et. al.[110] a similar feature was identified, compression in excess of 6.7% along the *a* cell edge was required to induce any buckling in the layer. It may be significant that at 40 GPa, the compression of the bulk unit cell along *a* has not reached this threshold value; compression in excess of 40 GPa appears to be

required to perturb the atomically flat nature of the $C_6N_9H_3$ layers. The equivalence of *a* and *b* lattice parameters, as required for hexagonal symmetry, is retained by $C_6N_9H_3$ in the 0-40 GPa range.

The first discontinuity in figure 78 is observed at a pressure of between 40 and 50 GPa for $C_6N_9H_3$. This discontinuity is characterised by an abrupt increase in the value of the *a* and *b* lattice parameters, and a decrease in the value of the *c* lattice parameter and cell volume. These observations suggest that a structural change occurs between 40-50 GPa in the calculated $C_6N_9H_3$ solid. The internal dihedral angle of the triazine rings that overlap each other in the unit cell (figure 75) changes from 0° at 40 GPa to ~ 60° at 50 GPa, consistent with a sp^2 to sp^3 rehybridisation of its constituent atoms. In fact the calculated $C_6N_9H_3$ structure at 50 GPa shows the first signs of interlayer bonding, particularly between the triazine rings that lie directly above and below each other in the structure, this is highlighted in figure 80.

The change in dihedral angle observed in figure 79 indicated that the sp^2 to sp^3 re-hybridisation is not a gradual process but an abrupt change. So the data can be interpreted in the following way; as the pressure is increased up to 40 GPa the intra-layer stress is absorbed by contraction of the C-N intra-layer bonds, not by the buckling of the layers, so the layers remain flat ensuring the maximum amount of π-electron delocalisation. At 50 GPa this process is no longer energetically favourable and the layers begin to buckle, re-hybridisation from sp^2 to sp^3 of the atoms in triazine rings in the layers creates dangling bonds on the C and N atoms which point out perpendicular to the ring. The triazine rings that lie directly above and below each other in adjacent layers are able to combine dangling bonds which results in interlayer bonding. The process is not

local but is long ranged in the 001 direction. Once a C_3N_3 ring becomes sp^3 hybridised, it projects its dangling bonds on both sides (above and below its original plane), and therefore forms interlayer bonds simultaneously with both adjacent layers in the structure. As a consequence, the structure contains pillars of a carbon-nitride phase with three-dimensional connectivity that protrudes along the 001 direction as highlighted in figure 80. The interlayer bonding mechanism is probably able to absorb most of the compression strain at 50 GPa, leaving the remaining parts of the layers relatively flat.

Figure 80. (a) Structure of *g*-$C_6N_9H_3$ after geometry optimisation at 50 GPa. The highlighted area indicates the region where interlayer bonding occurs and; (b) a representation of the 1-dimensional pillars spanning the structure along (001) as a result of interlayer bonding (the triazine rings between much of the layers is not shown for ease of viewing)

Finally it can be observed that, while the sharp decrease in the value of the *c* lattice parameter at 50 GPa can be easily explained by the formation of

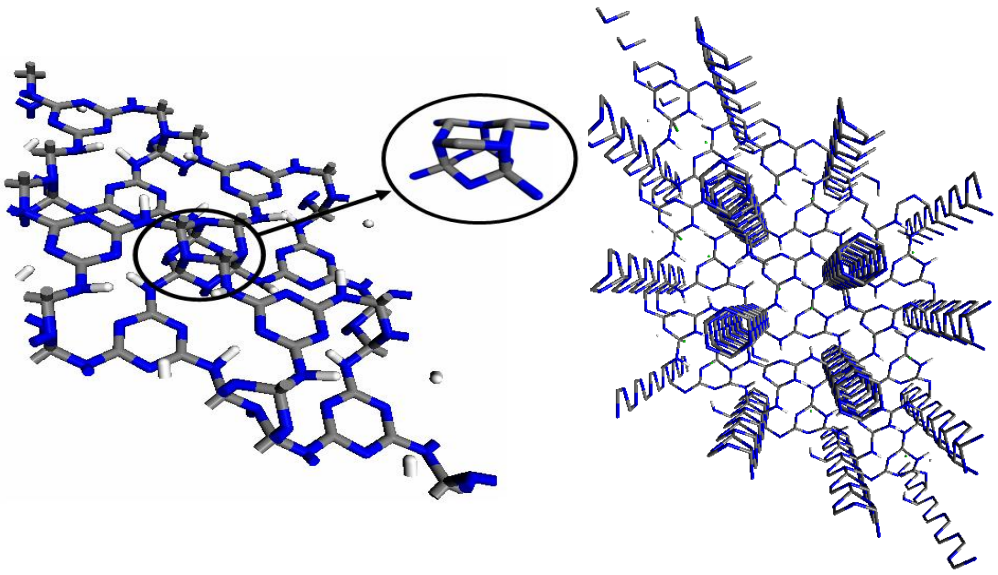

interlayer bonds, the corresponding increase in *a* and *b* is less obvious. However, this change could be attributed to the increased length of the sp^3 hybridised C-N bonds, which have now single-bond character instead of partial double bond as

in the sp^2 hybridised triazine ring, and cause an expansion of the lattice spacing in the 001 plane.

The structure with inter-layer bonding formed at 50 GPa retains hexagonal cell shape, and evolves without further chemical changes up to 85 GPa, above which a second discontinuity appears in the e lattice parameter plot in figure 78. In the structure observed at 90 GPa the *a* and *b* lattice parameters are no longer degenerate and the structure has lower symmetry than hexagonal. In fact, the geometry-optimised structures calculated at 90 and 100 GPa (see figure 81), bear only a minor resemblance to the ambient-pressure phase. The one-dimensional pillars originating from interlayer bonding and first observed at 50 GPa remain stable at 90 and 100 GPa; however, the remaining parts of the structure show significant distortions, and the large $C_{12}N_{12}$ interstitial cavities associated with the ambient-pressure $C_6N_9H_3$ structure have now collapsed leading to extensive reconstructions. The 100 GPa structure comprises an extensive array of new bonds, some of which form dense C_2N_2 rings; the almost total loss of short and medium-range order, which may indicate the onset of amorphisation in the structure, in agreement with the experimental observation. Although the pressure at which this process is observed is largely overestimated in the computational work. The structure obtained computationally at the highest pressure examined (100 GPa, shown in figure 81) appears to have full three-dimensional connectivity and low crystallinity.

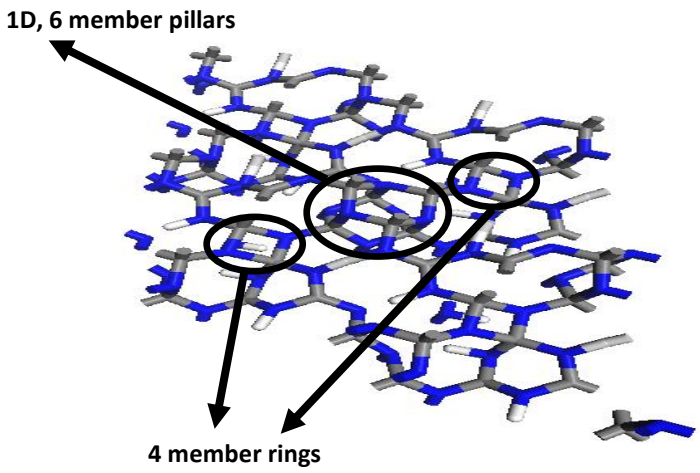

Figure 81. Geometry optimised $C_6N_9H_3$ solid at 100 GPa.

The behaviour of the solid of composition $C_6N_9H_3 \cdot HCl$, with full occupancy of the interstices by HCl, was also investigated computationally in a similar way to the $C_6N_9H_3$ phase discussed above. The change of calculated cell parameters (*a*, *b*, *c*) as function of pressure is also reported in figure 78 above.

The overall behaviour of $C_6N_9H_3 \cdot HCl$ is similar to that discussed earlier for $C_6N_9H_3$, and even in this case two discontinuities appear in the curve of figure 78, but they appear at higher pressure values of 70 and 90 GPa, respectively. Up to a pressure of 60 GPa, no major electronic or structural rearrangements occur in $C_6N_9H_3 \cdot HCl$, and the structure is best described as the evolution of the ambient-pressure system. It is however important to notice that the hexagonal cell shape is lost at much lower pressure: already at 20 GPa a noticeable difference in the *a* and *b* cell edges can be observed. This increases on further pressurisation. It is also notable that irrespective of pressure only type 1 nitrogens (N1) will be protonated (as discussed in a previous chapter).

In the pressure range of 0-60 GPa the $C_6N_9H_3$·HCl structure retains the same connectivity as the ambient-pressure model. A more pronounced decrease in the *c* than in the *a* and *b* parameters can be observed, this is consistent with the layered nature of the structure and the experimental results for the pressurisation of the $C_6N_9H_3$·HCl material and the calculated $C_6N_9H_3$ model. The quantitative changes of the individual lattice parameters are however smaller for $C_6N_9H_3$·HCl than for $C_6N_9H_3$. At 40 GPa, the variation of the *a*, *b* and *c* lattice parameters is 3.7%, 5.8% and 17% respectively in $C_6N_9H_3$·HCl, compared with 6.7%, 6.7% and 28% in $C_6N_9H_3$. The resulting change of volume in the 0-40 GPa range is of 32% in $C_6N_9H_3$·HCl, compared to 37% in $C_6N_9H_3$, and in $C_6N_9H_3$·HCl increases to 37% at 60 GPa. The inclusion of the large Cl^- ions in the interstices, therefore, makes the material less compressible. We attribute this feature to the close contact between the Cl^- ion and the H atoms that decorate the $C_{12}N_{12}$ cavities of the layer. The steric effect of Cl^- ion prevents the contraction of the large $C_{12}N_{12}$ voids in the layers that are unhindered in the $C_6N_9H_3$ model solid.

A further difference between the behaviour of $C_6N_9H_3$·HCl and $C_6N_9H_3$ is that the former loses the atomically flat nature of the layers at a relatively low pressure. This is highlighted in figure 82 which shows the variation of a number of dihedral angles in the $C_6N_9H_3$·HCl model as a function of pressure.

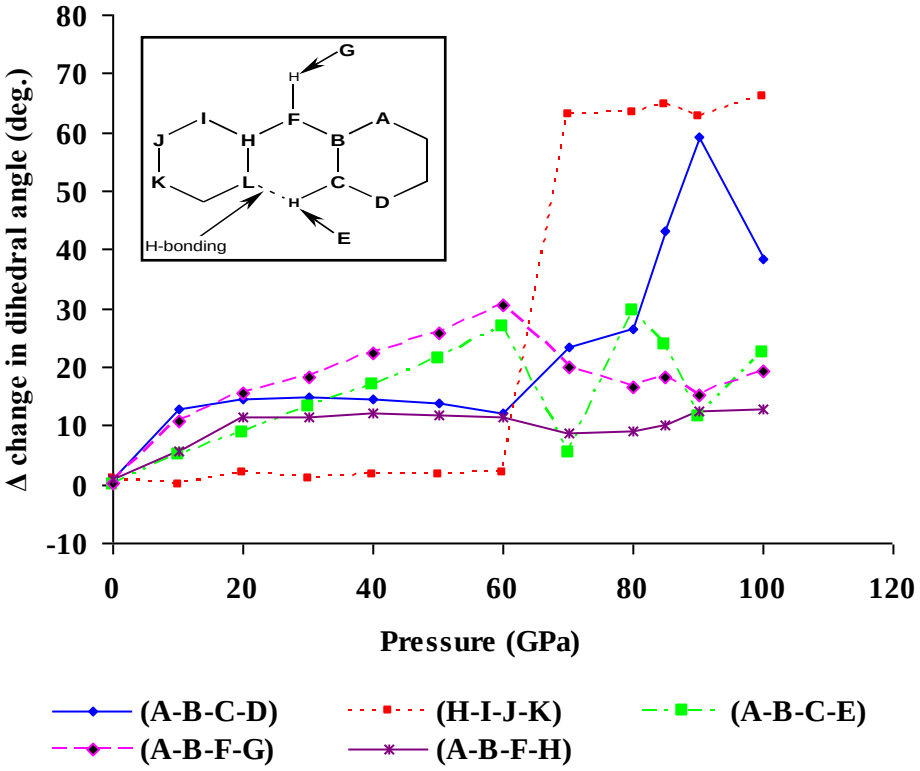

Figure 82. Dihedral angles of *g*-$C_6N_9H_3$·HCl as a function of p: A-B-C-D corresponds to the internal dihedral angle of the protonated triazine ring, H-I-J-K to the internal dihedral angle of the unprotonated triazine ring, A-B-C-E to the dihedral formed by the acid proton with the C_3N_3 ring to which it is bonded, A-B-F-G to the dihedral angle formed by the skeletal H with the neighbouring triazine ring and A-B-F-H to the dihedral angle between consecutive triazine rings.

The measurements in figure 82 refer to; 1) the internal dihedral angle of the protonated C_3N_3 ring (A-B-C-D); 2) the dihedral formed by the acid proton from HCl with respect to the C_3N_3 ring to which it is bonded (A-B-C-E); 3) the dihedral angle formed by the skeletal proton (i.e. the bridging NH group) with respect to the neighbouring triazine ring (A-B-F-G); 4) the dihedral angle between consecutive triazine rings (A-B-F-H) and; 5) the internal dihedral angle of the non-protonated C_3N_3 ring (H-I-J-K). There are a number of features worth noting.

- The un-protonated triazine rings in the model remain flat up to a pressure of 60 GPa, this is evidenced by the deviation of the internal dihedral angle HIJK being less than 2° from flat (0°) all the way up to this pressure. This was also the case for the $C_6N_9H_3$ indicating that the heterocyclic rings within the structure have a resistance to compression at lower pressures.
- The largest variations in the 0-60 GPa range are observed for the angles involving the proton from the dissociated HCl and H atoms of the $C_6N_9H_3$ backbone (ABFG and ABCE). Upon compression these H atoms experience strong short range repulsion from the Cl^- ions located in the $C_{12}N_{12}$ voids in the layers, towards which the N-H bonds are directed. As a result the N-H bonds are bent out of plane in an effort to lower this repulsion at the expense of less effective π-electron delocalisation in the layer. The re-orientation of the N-H bonds out of the plane reaches a maximum of 27° and 30° at 60 GPa.
- The protonated traizine ring shows some internal relaxation (the ABCD angle reaches a maximum of 14°), however this appears to be a secondary process driven by the re-orientation of the N-H bond.
- There is a small twisting distortion of adjacent triazine rings (ABFH) with a maximum value of 12° at 40 GPa.
- The chloride ions are only slightly forced out of the plane of the layers and the anchored protons align themselves towards the chloride ion. This combination of distortions suggests that the NH groups provide soft degrees of freedom to the $C_6N_9H_3$ layers and can be distorted relatively easily to alleviate the compression strain in the material caused by the

pressure exerted upon it. These observations are consistent with the study on single layers conducted previously[110].

Therefore, the computational model suggests that the overall distortion of the $C_6N_9H_3{\cdot}HCl$ layer is driven by the large steric size of the chloride ions. These ions cause short range repulsion with the hydrogen atoms in the $C_6N_9H_3$ backbone. These repulsions force the N-H bonds to bend out of plane. Consecutive triazine rings are twisted with respect to each other to form hemispherical cages around the chloride ions to maximise the electronic interaction between the positively charged hydrogens and the chloride ions.

For the $C_6N_9H_3{\cdot}HCl$ model the first discontinuity in the lattice parameter curve, displayed in figure 78, occurs between 60 and 70 GPa this is characterised by a sharp drop in the *c* lattice parameter while the unit cell simultaneously expands across the *ab* plane. These variations closely resemble those observed with the onset of inter-layer bonding at 50 GPa in the $C_6N_9H_3$ model. A similar process also occurs for the $C_6N_9H_3{\cdot}HCl$ model but the pressure at which it is first observed is higher. In the optimised structure for the $C_6N_9H_3{\cdot}HCl$ model at 70 GPa inter-layer bonding has occurred in the triazine rings that lie above and below each other in adjacent layers. Analogously to the $C_6N_9H_3$ model an abrupt change in the internal dihedral angles of the triazine units (HIJK) from 0 to 60°, indicative of an sp^2 to sp^3 re-hybridisation.

As for $C_6N_9H_3$ the $C_6N_9H_3{\cdot}HCl$ model the inter-layer bonding is a collective process that produces one dimensional pillars of a three dimensionally connected carbon nitride structure along the 001 direction. However, in contrast with the $C_6N_9H_3$ model, where the parts of the layer not involved in inter-layer bonding showed minor, if any, relaxation. Inter-layer bonding in the

$C_6N_9H_3{\cdot}HCl$ model is accompanied by an extensive relaxation involving realignments of the N-H$^{\cdots}$Cl bonds as indicated by the widespread variation of all dihedral angles accompanying the occurrence of inter-layer bonding at 70 GPa, see figure 82.

The second discontinuity in the $C_6N_9H_3{\cdot}HCl$ model occurs between 85 and 90 GPa. Again it is similar to that seen for the $C_6N_9H_3$ model and in this case takes place at a similar value of applied pressure and results in a structure with extensive three dimensional connections with a loss of short and medium range order indicating that an amorphisation process may have occurred within the material.

Comparison of the experimental and computational data provides a consistent picture of the likely transformation mechanisms in the $C_6N_9H_3$.HCl material under compression. However, the onset of structural rearrangements in the computational calculations (at 50 or 70 GPa depending on the HCl content of the model) is largely underestimated compared to the value of 25-30 GPa observed experimentally. This may be due to constraints of the computational study; the ambient pressure structure identified earlier in the computational calculations corresponds to a local minimum in the potential energy surface. Any chemical or structural transformation is therefore likely to require a non-zero activation barrier in order to take place. Experimentally this energy is provided by both pressure and temperature of the free energy. While in a static computational calculation, such as these, the temperature contribution is neglected. Therefore, it is expected that the onset of any transformation will be shifted to a higher value of pressure in the calculation compared with experiment.

To investigate the system in greater detail further calculations were performed on the $C_6N_9H_3$ and $C_6N_9H_3{\cdot}HCl$ models starting from the high pressure structures where the inter-layer bonding is first observed and gradually decreasing the pressure exerted on the model in steps of 10 GPa. As the pressure was gradually decreased the $C_6N_9H_3$ model was able to retain the structure with inter-layer bonding back down to ambient pressure, while the inter-layer bonding in the $C_6N_9H_3{\cdot}HCl$ model was retained only down to a pressure of 3 GPa.

Upon further reduction of the pressure inter-layer bonding in $C_6N_9H_3{\cdot}HCl$ was lost. However, the layers did remain buckled and do not return to their initial un-compressed planar confirmation. From this series of calculations the enthalpies of the models with and without inter-layer bonding are available in the pressure range of 3-70 GPa for the $C_6N_9H_3{\cdot}HCl$ model and this is shown in figure 83. It is clear that the transition pressure observed in the first series of calculations (as pressure was increased) was indeed overestimated. From figure 83 is it possible to estimate that at 7 GPa the two phases, with and without inter-layer bonding, of $C_6N_9H_3$ are iso-energetic, while this value increases to 45 GPa for the $C_6N_9H_3{\cdot}HCl$ model. This new value is much closer to the pressure at which the structural order appears to be lost from the experimental material.

In agreement with the earlier discussion, the presence of HCl within the voids in the layers of $C_6N_9H_3{\cdot}HCl$ has a considerable retarding effect on the onset of phase transitions in the solid.

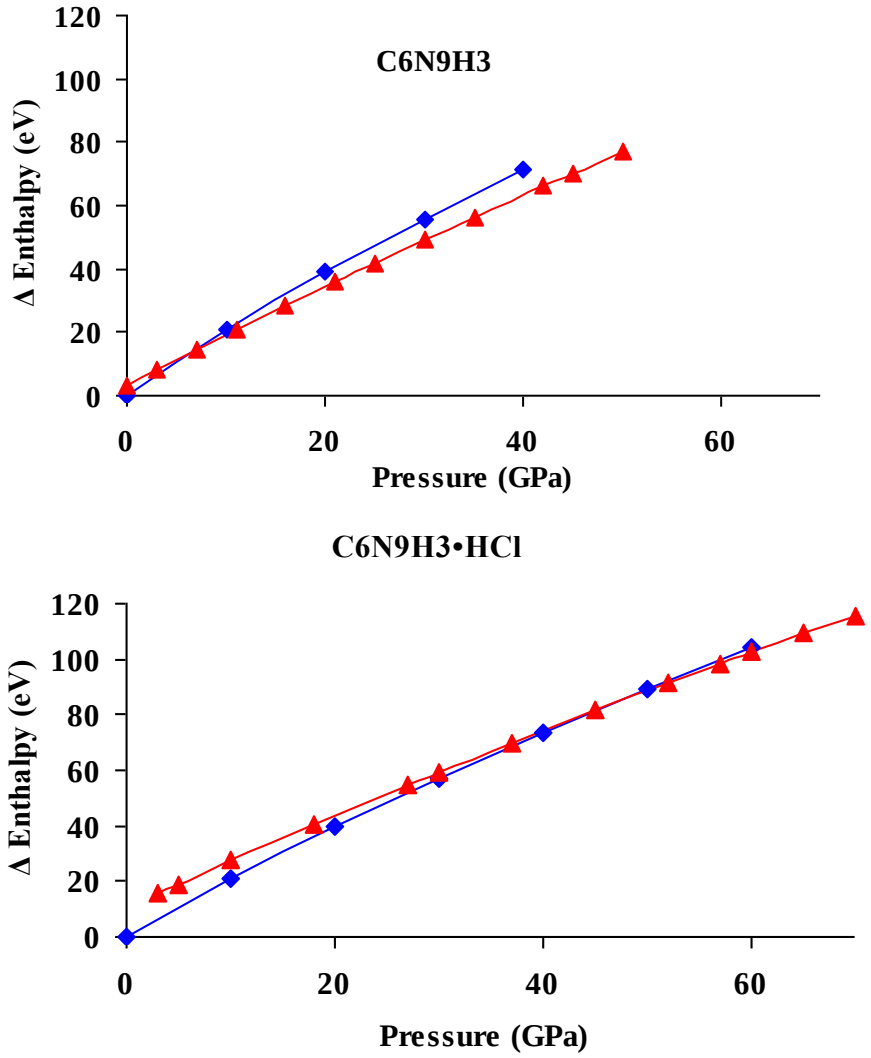

Figure 83. Calculated enthalpy for the phases with interlayer bonding (blue line) and without interlayer bonding (No ILB (red line): top for *g*-$C_6N_9H_3$ and bottom for *g*-$C_6N_9H_3$·HCl.

In the light of the computational calculations discussed above it is likely that the actual HCl content of the $C_6N_9H_3$.*x*HCl material plays a major role in the pressure induced structural reconstructions. The experimental data appear to indicate a large degree of disorder and/or non-uniformity in the HCl content. If this is the case, according to the computational calculations, it is likely that different regions of the material will begin to buckle and form inter-layer bonds at different values of pressure. It is therefore expected that a gradual, rather than

abrupt/discontinuous, transition will be observed as pressure is increased which agrees with the observations from the experimental X-ray diffraction data presented in figure 70.

An outcome of the computational calculations is the prediction that the pressure of the onset of a phase transition under compressive strain would be minimised for an HCl free solid, therefore representing a useful synthetic target. Also an HCl free structure with inter-layer bonding would likely be recoverable to ambient conditions by a gradual pressure decrease. However, this would not be the case for the material with all the voids being occupied by HCl (i.e. $C_6N_9H_3.x$HCl where $x = 1$). These observations provide valuable strategies for future experimental extensions of the work.

5.4 Experimental Decompression Behaviour of $C_6N_9H_3$.HCl

In addition to the experiments studying the effect of increasing pressure on the $C_6N_9H_3.x$HCl experimental material it was also possible to obtain a few sets of data measuring the X-ray diffraction pattern of the material while the pressure was decreased. Figure 84 shows the synchrotron X-ray diffraction pattern of the $C_6N_9H_3.x$HCl material as the pressure is decreased from 21 to 10 GPa.

The material was first taken up to a pressure of 30 GPa in the diamond anvil cell in steps of about 5 GPa over a period of 2 days as experiments were conducted to study the behaviour as pressure was increased. At this pressure the

material should have attained the highly disordered/amorphous structural composition previously discussed. Once the pressure of 30 GPa was attained the cell was held at this pressure for 60 minutes to allow the material to equilibrate. The pressure was then decreased to 21 GPa and the X-ray diffraction measurements recorded, the process was repeated after decreasing the pressure to 15.7 and 10 GPa subsequently. It was not possible to obtain more data points at other pressures due to time and technical constraints at the facility.

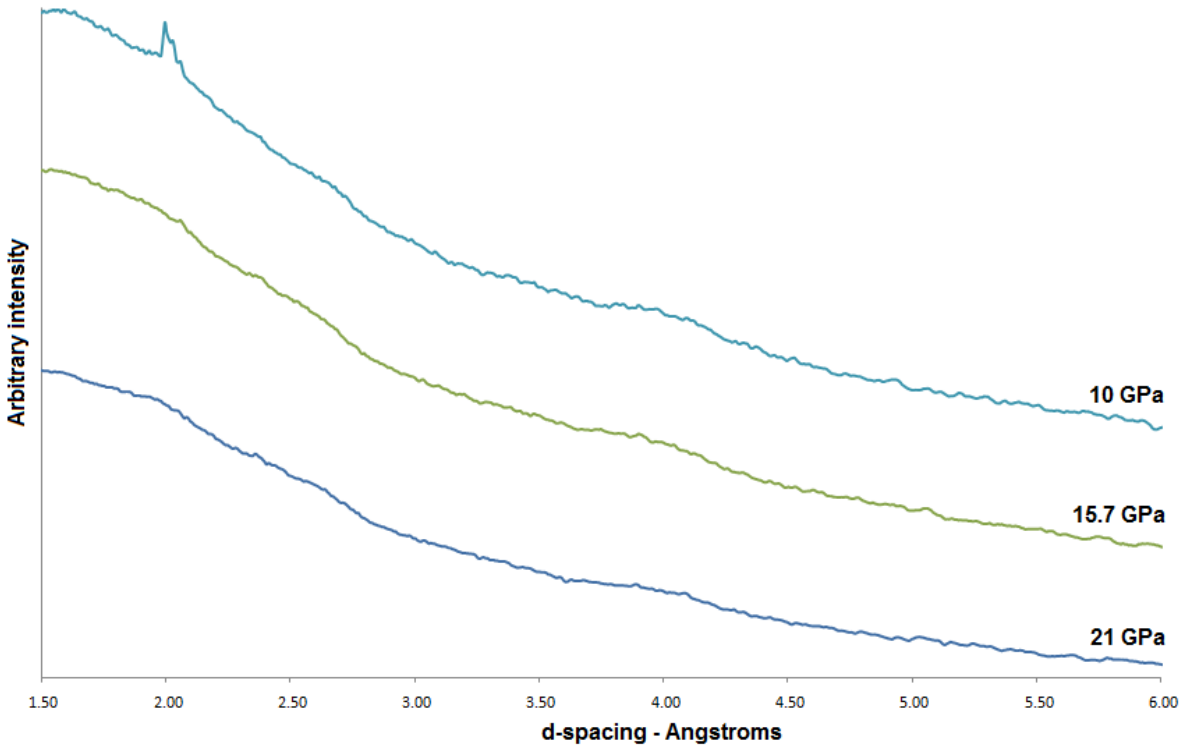

Figure 84. Synchrotron X-ray diffraction patterns of the $C_6N_9H_3.xHCl$ material as the pressure is decreased from 21-10 GPa.

At a pressure of 21 GPa the diffraction pattern of the $C_6N_9H_3.xHCl$ material appears very similar to that observed for higher pressures. There is a distinct lack of any resolvable diffraction peaks. The characteristic 'plateau' like feature is visible between about 2 and 2.5 Å indicating that the material is still very disordered and likely to contain the inter-layer bonding predicted by the computational studies. As the pressure is decreased to 15.7 GPa the 'plateau'

like feature seems to be slightly less well defined and that some more small peaks may be starting to appear, however these are very broad and small with very low intensity from the background so it is difficult to tell whether they could be an effect of noise or something more significant. At a pressure of 10 GPa the main notable feature in this diffraction pattern is the relatively sharp peak now present at a d-spacing value of 2.0Å. This is interesting as it may be an indication that the material is beginning to recrystallise, either back to something resembling its original form or something slightly different as predicted by the computational study of the model $C_6N_9H_3$.HCl material. It is also possible that the peak is an anomaly due to the presence of the gasket material (rhenium) in the diffraction pattern. This is a possibility as one of the two most characteristic peaks for rhenium metal would be expected to appear at around 2 Å at such pressures. Figure 85 shows a diffraction pattern of the material where the rhenium gasket has become visible with the characteristic sharp peaks at 2.1 and 2.4 Å. However, it is odd that the other peak is not visible as it is expected to be just as intense as the first.

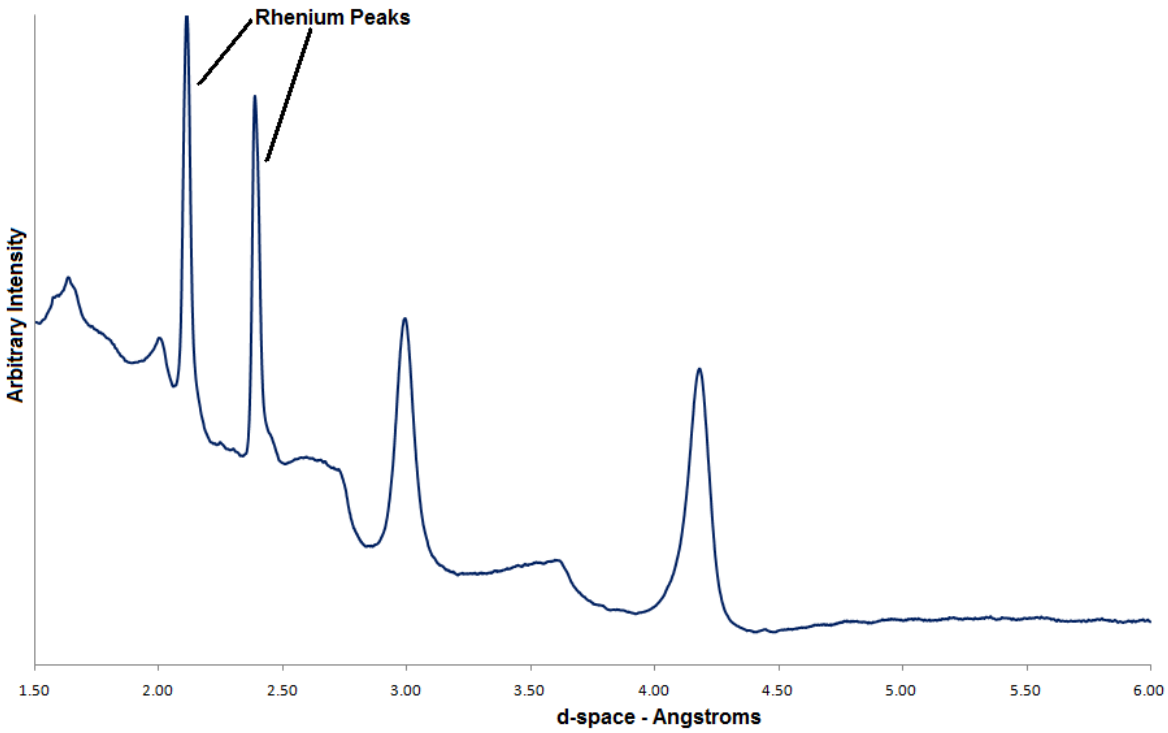

Figure 85. Synchrotron X-ray diffraction pattern of the $C_6N_9H_3$.HCl material at 4 GPa showing the characteristic peaks from the rhenium metal gasket.

Figure 86 shows synchrotron X-ray diffraction patterns of the $C_6N_9H_3$.HCl material at ambient pressure both before and after compression to over 25 GPa and subsequent decompression to ambient pressure. The data were taken without the diamond anvil cell as it is not possible to completely release the pressure from the material while the gasket is still contained with the cell.

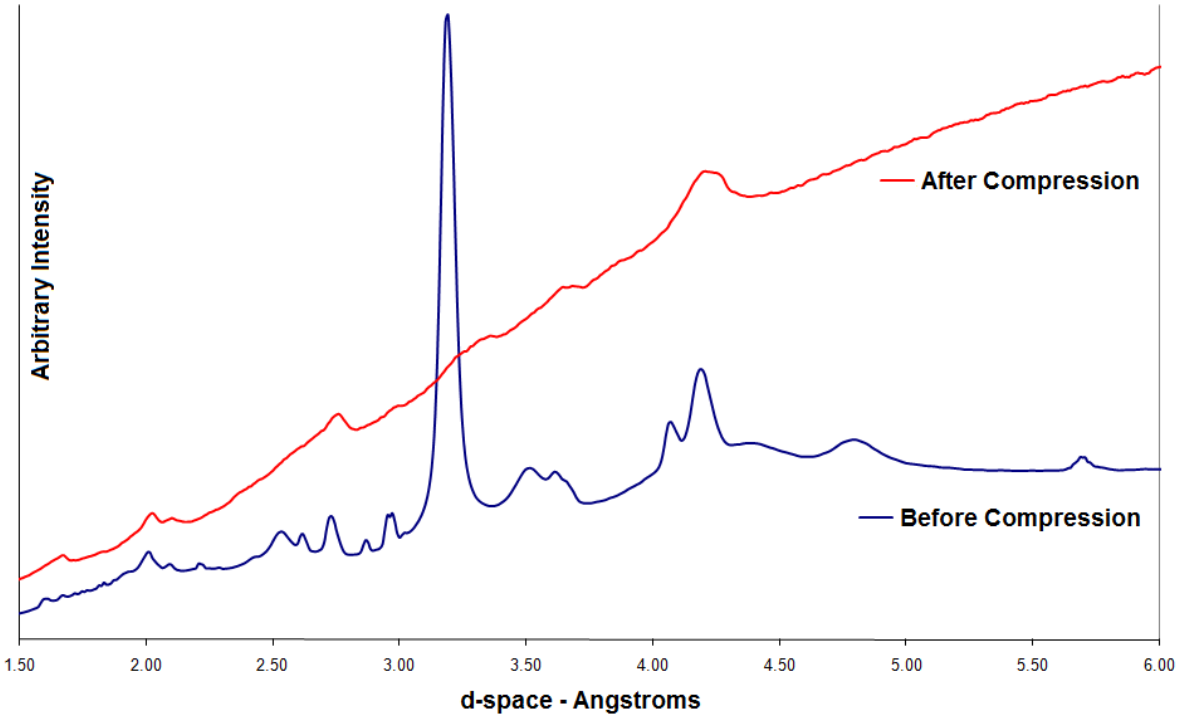

Figure 86. Synchrotron X-ray diffraction patterns of the $C_6N_9H_3$.*x*HCl material before and after compression at ambient pressure.

Before compression the crystalline structure of the material is clearly shown by the pattern of sharp peaks which correspond to the model structure proposed for the material, as previously discussed. It is interesting to note that after compression and upon complete decompression of the material that the 002 peak is absent, even though some peaks matching certain reflections from the original uncompressed material do still appear to be visible. This indicates that there is still significant disruption to the regular layered structure in the material once the material comes back to ambient pressure. It is possible that the layers are severely buckled, as suggested by the computational calculations, after decompression and that the layers have not returned to their planar conformation, even if the inter-layer bonding does not persist, this would be an explanation for the absence of the 002 reflection in the diffraction pattern. The computational calculations predict that a $C_6N_9H_3$ material with HCl component

would retain its inter-layer bonding all the way down to ambient pressure. It is therefore also a possibility that the experimental $C_6N_9H_3.xHCl$ has a value of *x* that is less than one, closer to zero perhaps. The weak and broad nature of the reflections observed after decompression compared to those observed prior to compression indicates that the structure of the material is still in a very disordered state after compression and that the original structure of the material is not recoverable to ambient conditions following compression past the point at which the material appears to become disordered and that the material is clearly very different on decompression to the original material pre-compression.

5.5 Infra Red Spectroscopy of $C_6N_9H_3{\cdot}HCl$ at High Pressures

In addition to the ambient pressure infra red measurements discussed in the previous chapter, experiments were also attempted to follow the IR spectra of the $C_6N_9H_3{\cdot}xHCl$ material as a function of pressure. These experiments were conducted in the diamond anvil cell using specially selected type IIa diamonds that are necessary for IR experiments. A full explanation of this is found in the experimental methods. The measurements were carried out using the bench mounted IR microscope (*IRscope II, Bruker Optiks*) with a Bruker *IFS 66v/S* FTIR spectrometer. The use of the microscope allows routine transmission and reflectance measurements to be taken with samples in a diamond anvil cell. All the measurements presented here were taken using the transmission mode.

The spectra were taken using a screw driven 'Mao' type diamond anvil cell fitted with type IIa diamonds with the culets cut to 800 µm, this was the only pair of IR compatible diamonds available for use in the laboratory. This

culet diameter is relatively large, especially when compared to the 300 µm culets that were used in the diffraction experiments. The size of the diamond culets used has a direct relationship with the maximum pressure achievable for a diamond anvil cell experiment. Therefore the IR experiments presented here were limited to a relatively low value of pressure (8.3 GPa) and it was not possible to obtain an analogous pressure range to that of the diffraction study (up to 60 GPa) for comparison. It was possible to obtain spectra in the diamond anvil cell for six pressure points ranging from 0.7 GPa up to 8.3 GPa, and also the ambient pressure spectrum (not in DAC) for comparison. The data are displayed below in figure 87.

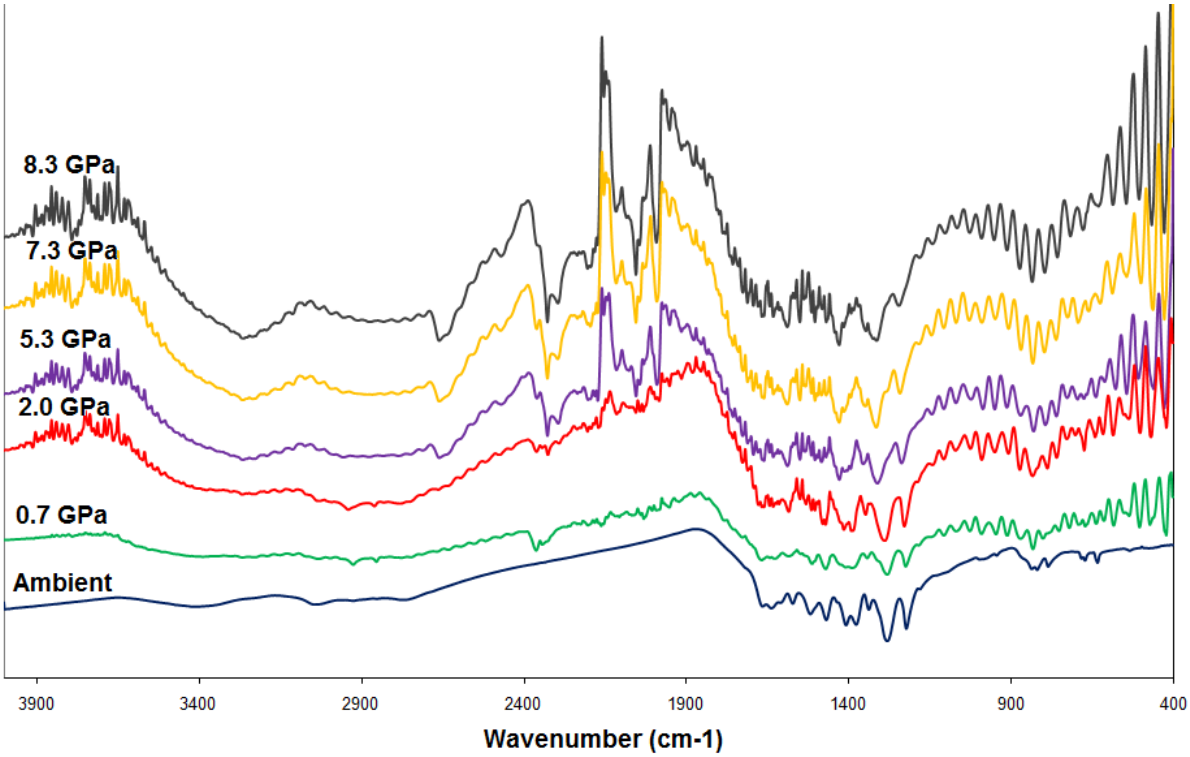

Figure 87. IR spectra of the $C_6N_9H_3$.HCl material at high pressures.

It can easily be seen that the general shape of the high pressure spectra are a good match to that of the ambient. However, the high pressure data are a lot less smooth and much noisier than the spectrum seen for the $C_6N_9H_3$.HCl

material at ambient pressure. There are two reasons for this, the first being that the background subtraction attempts to remove a great many peaks from the spectra that are a result of the diamond windows, when this removal takes place there may be a slight difference in intensity between the background spectra and the experiment spectrum. This effect is seen in the ~1900-2200 and ~3400-3900cm^{-1} regions where the diamond peaks are found. These intensity variations can be due to the variation in the detector temperature (as the coolant evaporates and is replaced periodically during experiments). The other thing affecting the signal to noise ratio and appearance of the spectra is the fact that the experiments conducted in the diamond anvil cell are affected by the observation of interference fringes (these can be seen as a wobble or modulation of the base line in the spectrum) caused by the separation distance between the diamonds and the fact that the IR radiation passes through the diamond, sample then diamond again. The change in refractive index between these affects the radiation as it passes through.

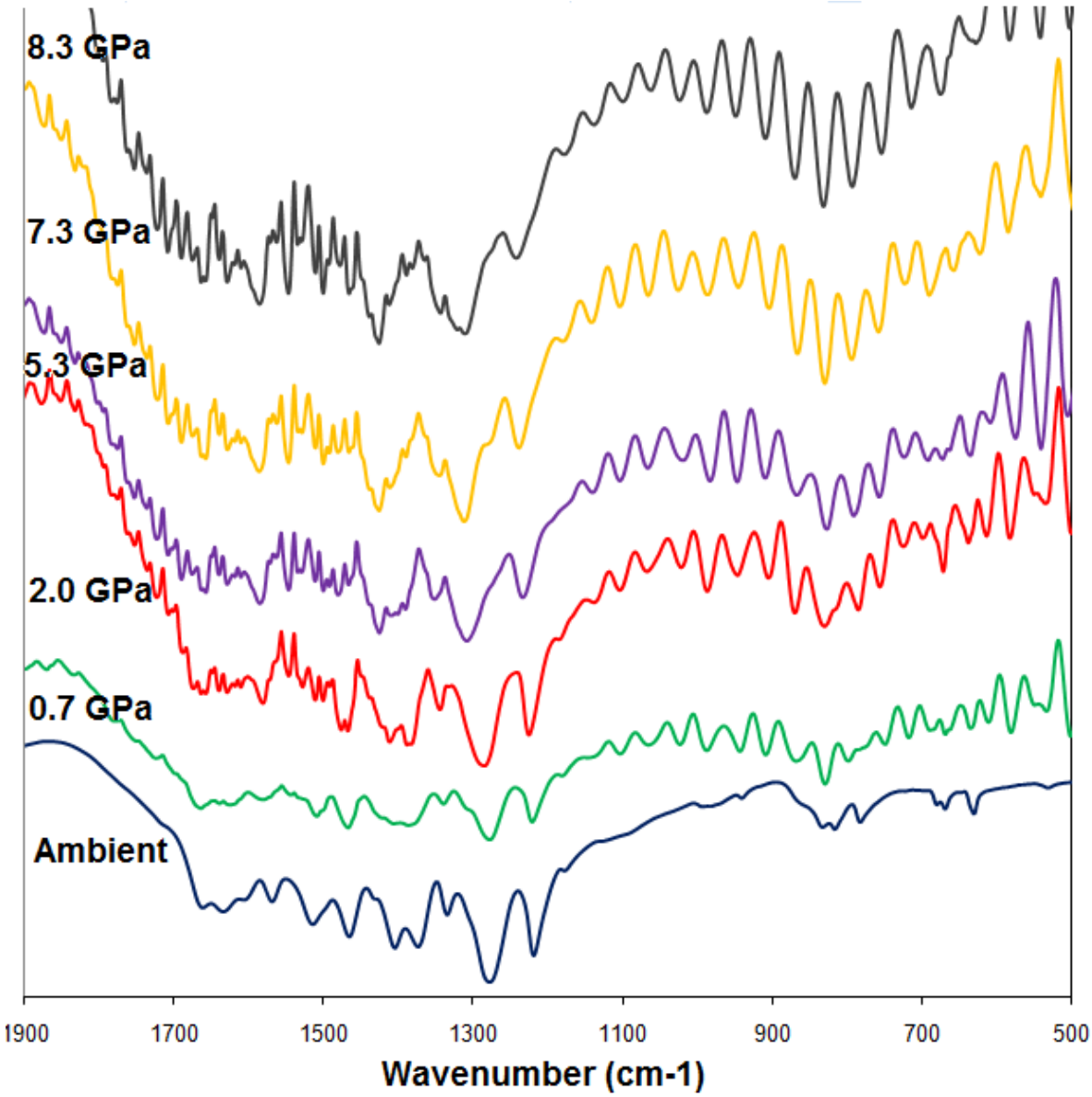

Figure 88. Close up of the 500-1900 cm^{-1} region of the high pressure IR spectra.

Figure 88 above shows the high pressure IR spectra close up in the 500-1900 cm^{-1} region, the main region of interest for the material. It is clear that the high pressure spectra have the same general shape as the ambient material but again the interference fringes cause a problem when trying the pinpoint specific peaks and features in the material. It is possible to make out the series of features in the 1400-1700 cm^{-1} region of all spectra which are typical of the stretching vibrations of the CN heterocyclic structures, namely the *s*-triazine ring, in the

material. It is also possible to make out the peaks in the 800 cm^{-1} region in some of the lower pressure spectra. This is assigned to the out of plane deformation of the triazine ring. However, as the pressure is increased it becomes less easy to resolve these features in the higher pressure spectra. This could be due to a loss of intensity as the sample becomes thinner in the cell as the pressure is increased or indeed to changes in the material as the pressure is increased.

The two most intense and easily recognisable peaks in the IR spectra shown above lie at 1221 and 1279 cm^{-1} at ambient pressure and are labelled as a and b respectively. The shift of these peaks under pressure can be plotted and is displayed in figure 89. As pressure is increased the peaks move to lower wavenumber. This is as would be expected, as the material is compressed and densifies the bonds within the layers are also compressed and the vibrational frequency of the bonds increases.

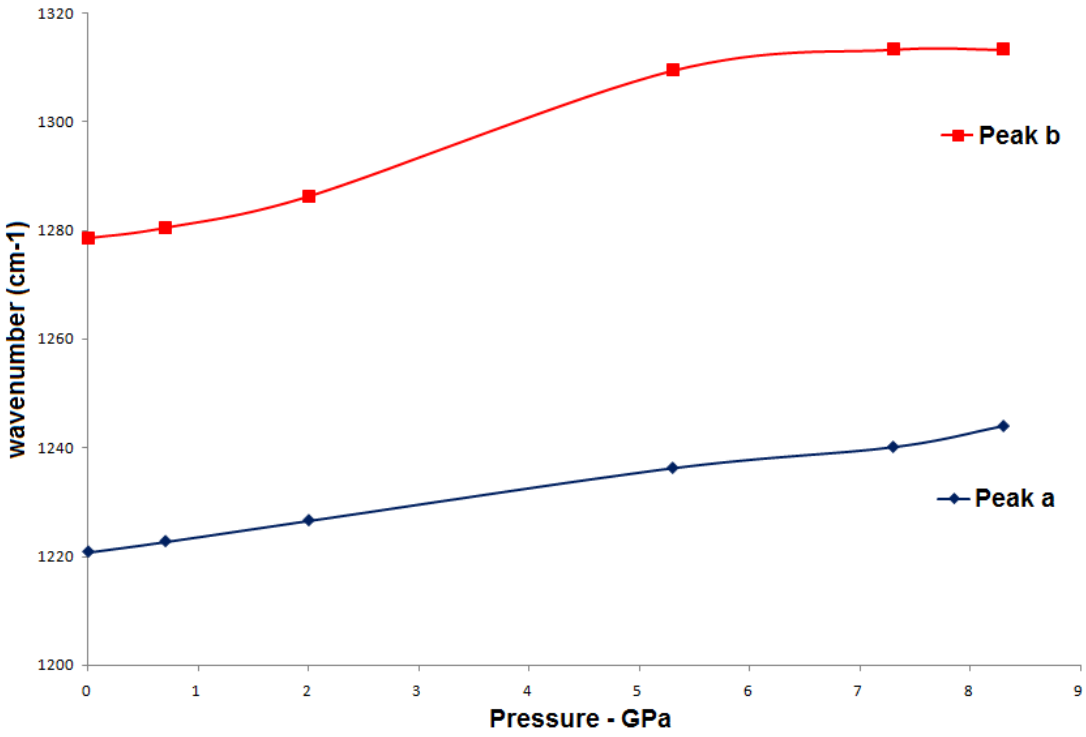

Figure 89. Plot of the change in wavenumber of easily identifiable peaks from the IR spectra as the pressure is increased in the $C_6N_9H_3{\cdot}HCl$ material.

Due to the poor quality of the high pressure spectra it is difficult to deduce useful information from the experiments. Therefore it is not possible to tell from these data if there are the beginnings of any changes to the sample over the pressure range of these experiments. Coupled with the fact that it was only possible to obtain spectra up to 8.3 GPa and it can be seen from the high pressure diffraction data that no distinct changes are observed in the material until much higher pressures are attained. More work needs to be conducted using diamonds with smaller culets so high pressures can be generated. It may also be possible to remove the peaks and unstable baseline caused by the interference fringes using a mathematical process involving manipulating the Fourier transform for each spectrum.

5.6 Conclusions

This chapter has focussed on the analysis of the synthesised $C_6N_9H_3.xHCl$ material by X-ray diffraction, both at ambient and very high pressures. The structure of the synthesised material has been shown to be an excellent match with the model structure proposed previously by Zhang e. al[8]. It is seen that the material is highly compressible at low pressures and structural definition is lost at about 35 GPa. Computational calculations undertaken in collaboration with fellow researchers at UCL have identified the likely binding sites for the protons and the location of chloride ions within the layers of the HCl containing form of the material. High pressure studies have been undertaken to assess the behaviour of the material under very high pressures. The structural modifications that the $C_6N_9H_3.xHCl$ (with x = 0 and 1) system undergoes under compression have been investigated experimentally and computationally. These layered carbon nitrides exhibit highly anisotropic behaviour and soft degrees of freedom associated with the bridging N-H groups that can bend to alleviate compressional strain in the remaining parts of the layer. Inter-layer bonding has been calculated to occur when reductions in the layer-layer separation can no longer be made. Atoms lying above and below each other become sp^3 hybridised and form dense one dimensional pillars of a new carbon nitride phase with three dimensional connectivity. Inter-layer bonding serves to satisfy the bonding requirements of the carbon and nitrogen atoms in the pillars. The presence of HCl in the layers retards the occurrence of inter-layer processes as a higher activation barrier needs to be overcome. The behaviour of $C_6N_9H_3.xHCl$ is sensitive to the amount and uniformity of HCl incorporated in the layers. The computational calculations indicate that an HCl free material would show pressure induced transformations at the lowest

pressure and that the phase with interlayer bonding would be most recoverable at ambient pressure for $C_6N_9H_3$ and this would be less likely for $C_6N_9H_3$.HCl.

The decompressional behaviour of the material has been investigated and it can be seen that the structure of the material is significantly different after compression and decompression to ambient than for the material before it is subjected to high pressure conditions and it does not return to the same structure upon decompression.

Finally the material has been studied using infra red spectroscopy at elevated pressures. However further work needs to be performed with smaller diamonds able to achieve higher pressures and the use of a mathematical correction to clean up the resulting spectra to deduce whether any changes to the bonding of the material as a function of pressure can be observed using this method.

Chapter 6 - General Conclusions and Future Work

During the work presented in this thesis the high pressure – high temperature synthesis of $C_6N_9H_3{\cdot}HCl$ has been achieved successfully and the material has been characterised by several different techniques. Overall the X-ray diffraction patterns and measured C:N:H ratio agree well with the proposed formula of $C_6N_9H_3{\cdot}HCl$. Therefore, it is fair to propose that the material fits the previously suggested structural model and that it is a good starting point for the investigation of the structure and composition of the material. The characterisation of the material has been continued and developed and further insights into the understanding the structure of the material have been made.

Collaborations with colleagues within the department at UCL who have computational expertise have resulted in simulations being carried out to help better interpret the structural characterisation of the $C_6N_9H_3HCl$ material. The initial structural model used to study the material was that proposed by Zhang et al and consists of $P6_3/m$ symmetry. When the material was studied computationally symmetry constraints were removed and the structure was optimised in the P1 space group. It was found that a much better fit between the calculated and experimentally observed x-ray patterns is seen if the symmetry is lowered from the hexagonal space group originally assigned to the material. This results in a small shift in the stacking of the layers in the 001 plane. It has been found that the actual layer stacking structure in the experimental material is likely to be more complex than was originally proposed.

In addition to the synthesis and characterisation of the $C_6N_9H_3HCl$ material it was also subjected to high pressure treatment in the diamond anvil

cell with pressures of up to 60 GPa. It was found that the material is highly compressible at lower pressures and all structural definition is lost and amorphisation is observed by the time a pressure of around 35 GPa is attained. Computational calculations have also been performed to model the high pressure behaviour of the material. Good agreement has been seen between the experimental and computational results. Interlayer bonding was calculated to occur in the material when the distance between the layers can get no smaller under compression. Some of the atoms in the layers re-hybridise to an sp^3 confirmation to form pillars of carbon nitride that extend across the layers to form a three dimensional connectivity. The calculations also suggested that the presence of HCl in the layers may retard the formation of interlayer bonds due the size of the Cl ions between the layers preventing them from getting as close together.

The decompressional behaviour of the material was studied and it can be seen that the structure of the material is significantly different after compression and decompression back to ambient pressure than for the material before it is subjected to high pressure treatment and the material does not return to the same structure upon decompression, the main feature being that the diffraction peak denoting the layer separation in the material is absent upon decompression suggesting that the material may in fact keep the inter layer bonding and/or disordered structure that is proposed to occur at high pressure on decompression.

The structure of the materials has also been investigated using Raman spectroscopy in several different experiments using lasers with different excitation energies. Due to the nature of the material it was not possible to use conventional visible Raman excitations as the strong fluorescence that results

completely obscures any Raman signal. So for the first time UV and FT Raman with near IR excitation were performed to successfully give a Raman spectrum of the material.

UV Raman spectra were then obtained which contained strong broad asymmetric features resembling those observed for amorphous carbon and heavily disordered graphitic carbon samples. Sharp peaks are observed at lower wavenumbers which correspond to the stretching vibrations of the triazine ring components of the structure. The UV Raman spectra are likely to be dominated by resonance Raman effects and the resulting spectra may represent only a small fraction of the structural species actually present within the sample.

FT-Raman spectra with near-IR excitation were also obtained for the material at ambient and low temperature. The main Raman band moved to a lower wavenumber but remained broad. The results indicated that disorder occurs within the carbon nitride graphitic layers which could be associated with disordering in the linkage formation between triazine units resulting in dispersion in the void sizes within the layers.

As a result of the experiments carried out and the observations made during this project it is possible to suggest some areas for future studies.

Following on from the diffraction studies of the high pressure behaviour of the material in the diamond anvil cell it would be useful to perform a heating experiment at high pressure to see if it is possible to perhaps induce a change in the material to a more dense form of carbon nitride. There have been several reports of materials changing their structure significantly or converting to another phase upon the application of extreme pressure and temperature conditions. A laser or resistive heating experiment within the diamond anvil cell

with *in-situ* X-ray diffraction would be a convenient way of investigating this. It may also be beneficial to re-run the ambient temperature high pressure experiments conducted during this work at a third generation synchrotron facility such as Diamond in Oxford, UK or the ESRF in Grenoble, France. This may give a much better resolution pattern and also it would be possible to take background measurements to further improve the quality of the results at these better equipped facilities.

It would also be interesting to conduct the high pressure infra red experiments with new suitable diamonds with a much smaller culet size e.g. 300-400 μm enabling much greater pressures to be attained so that the results may be compared to those obtained in the X-ray diffraction experiments. This would give a better insight into what happens to the bonding in the material as pressure is applied. These higher pressure experiments should also be treated with a mathematical correction to reduce the impact of the interference fringes on the quality of the spectra.

References

1. 1. J. Liebig, Ann. Pharm. 10 (1834) 10.
2. W. C. Kuryla and A. J. Papa, *Flame Retardancy of Polymeric Materials* (Dekker, New York, 1973-1979)
3. D. R. Miller, D. C. Swenson, E. G. Gillan *J. Am. Chem. Soc.*, 2004, **126** (17), 5372-5373
4. Meyer, R. *Explosives*, 3rd ed.; VCH Publishers: New York, 1987.
5. Q. Guo, Q. Yang, L. Zhu, et al., Solid State Communications **132**, 369 (2004).
6. X. Wang, K. Maeda, A. Thomas, K.Takanabe, G. Xin, J. M. Carlsson, K. Domen, M. Antonietti, *Nature Materials*, **8**, 2009, 76-80
7. G. Demazeau, H. Montigaud, B. Tanguy, et al., Rev. High Pressure Sci. Technol. **7**, 1345 (1998).
8. Z. H. Zhang, K. Leinenweber, M. Bauer, L. A. J. Garvie, P. F. McMillan, G. H. Wolf, *J. Am. Chem. Soc.* **123** (2001) 7788
9. E. Quirico, G. Montagnac, V. Lees, P. F. McMillan, C. Szopa. G. Cernogora, J-N. Rouzaud, P. Simon, J-M. Bernard, P. Coll, N. Fray, R. D. Minard, F. Rauliln, B. Reynard, B. Schmitt, *Icarus*, **198**, 1, 218-231 (2008)
10. B. V. Lotsch, M. Döblinger, J. Sehnert, L. Seyfarth, J. Senker, O. Oeckler, W. Schnick, Chem. Eur. J. 2007, **13**, 4969 – 4980
11. B. Jürgens, E. Irran, J. Senker, et al., Journal of the American Chemical Society **125**, 10288 (2003).
12. J. E. Lowther, Physical Review B **59**, 11683 (1999).
13. T. Komatsu, Journal of Materials Chemistry **11**, 802 (2001).
14. P. Kroll and R. Hoffmann, Journal of the American Chemical Society **121**, 4696 (1999).
15. D. T. Vodak, K. Kim, L. Iordanidis, et al., Chemistry: A European Journal **9**, 4197 (2003).
16. M.L. Cohen, *Phys. Rev. B* 32, 1985, 7988
17. A.Y. Liu, M. L. Cohen, *Science* 245, (1989), 841
18. D.M. Teter, R. J. Hemley, *Science*, 271, (1996), 53
19. J. Haines, J. M. Léger, and G. Bocquillon, Annual Reviews of Materials Research **31**, 1 (2001).
20. E. Horvath-Bordon, R. Riedel, A. Zerr, et al., Chemical Society Reviews **35**, 987 (2006).
21. S. Veprek, Journal of Vacuum Science and Technology A **17**, 2401 (1999).
22. I. Alves, G. Demazeau, B. Tanguy, et al., Solid State Communications **109**, 697 (1999).
23. J. Kouvetakis, A. Bandari, M. Todd, B. Wilson, N. Cave, *Chem. Mater.* **6**, 1994, 811
24. H. Montigaud, B. Tanguy, G. Demazeau, et al., Diamond and Related Materials **8**, 1707 (1999).
25. J. Ortega and O. F. Sankey, Physical Review B **51**, 2624 (1995).
26. M. Todd, J. Kouvetakis, T. L. Groy, et al., Chemistry of Materials **7**, 1422 (1995).

27. J. Martin-Gil, F. J. Martin-Gil, M. Sarikaya, M. Qian, M. Jose-Yacaman, A. Rubio, *J. Appl. Phys.* **81,** 1997, 2555
28. D. C. Nesting, J. Kouvetakis, J. V. Badding, *Beitrag zum Tagungsband in : The 5th NIRM International Symposium on Advanced Materials '98,* Tsukuba, Japan 1-5 March 1998.
29. T. Tomikawa, N. Fujita, Jpn. Patent JP 03240959A2, 1991, (Chem. Abstr. 116:163119)
30. J. Viehland, S. Lin, B.J. Feldman, K. Kilgore, M.T. Jones, *Solid State Commun.* **80**, 1991, 597
31. C. Niu, Y. Z. Lu, C. M. Lieber, *Science,* **261** (1993), 334
32. K. M. Yu, M. L. Cohen, E. E. Haller, W. L. Hansen, A. Y. Liu, I. C. Wu, *Phys. Rev. B* **49**, 1994, 5034
33. S. Matsumoto, E. Q. Xie, F. Izumi, *Diamond Related Mat.* **8**, 1999, 1175
34. E. Kroke, M. Schwarz, *Coordn Chem. Rev.* **248**, 2004, 493-532
35. Nieto-Sanz, D., Loubeyre, P., Crichton, W., Mezouar, M., *Phys. Rev. B.* **70**, 214108 (2004)
36. M.R. Wixom, *J. Am. Ceram. Soc.* **73**, 1990, 1973
37. T. Sekine, H. Kanda, Y. Bando, M. Yokahama, K. Hojou, *J. Mater. Sci. Lett.* **9**, 1990, 1376
38. Q. Lu, C. Cao, C. Li, J, Zhang, H. Zhu, X. Kong, X. Duang, *J. Mater. Chem.* **13**, 2003, 1241
39. Q. Lu, C. Cao, H. Zhu, *Chin. Sci. Bull.* **48**, 2003, 519
40. Q. Lu, C. Cao, C. Li, J, Zhang, H. Zhu, *Chem. Phys. Lett,.* **372**, 2003, 469
41. Y. Fahmy, T. D. Shen, D. A. Tucker, R. L. Spontak, C. C. Koch, *J. Mater. Res.*, **14**, 1999, 2488
42. L. W. Yin, M. S. Li, Y. X. Liu, J. L. Sui, J. M. Wang, *J. Phys. Cond. Matter.*, **15**, 2003, 309
43. V. N. Khabashesku, J. L. Zimmerman, J. L. Margrave, *Chem. Mater.* **12**, 2000, 3264
44. J. L. Zimmerman, R. Williams, V.N. Khabashesku, J. L. Margrave, *Nano Lett.* **1**, 2001, 731
45. G. H. Wolf, M. Bauer, K. Leinenweber, et al., in *Frontiers of High Pressure Research II: Application of High Pressure to Low-Dimensional Novel Electronic Materials*, edited by H. D. Hochheimer (Kluwer Academic, The Netherlands, 2001), p. 29
46. E. Quirico, C. Szopa. G. Cernogora, V. Lees, S. Derenne, P. F. McMillan, G. Montagnac, B. Reynard, J-N. Rouzaud, N. Fray, P. Coll, F. Raulin, B. Schmitt, B. Minard, *Organic Matter in Space* Proceedings IAU Symposium No. 251, (2008).
47. Depths of the Earth Company - http://www.depthsoftheearth.com/
48. Boyd, F.R. and Englund, J.L (1960) Apparatus for phase equilibrium measurements at pressures up to 50 kbars and temperatures up to 1750C J. Geophys. Res. 65, 741-748
49. J. R. Holloway, B. J. Wood, *Simulating the Earth*, 2nd Ed., 1991, Harper Collins Academic, pp 29-32.
50. High Pressure Techniques in Chemistry and Physics, Holzapfel, W. B., and Issacs, N. S., OUP, 1997
51. Walker, Am. Min., ***76***, 1092 (1991)
52. D. Walker, M. A. Carpenter, C. M. Hitch, Am. Min., ***75***, 1020 (1990)

53. K. Leinenweber, J. Parise, J. Solid State Chem., ***114***, 277 (1995)
54. C. E. Weir, E. R. Lippincott, A. Van Valkenburg, and E. N. Bunting, Infrared Studies in the 1- to 15-Micron Region to 30,000 Atmospheres, *J. Res. Natl. Bur. Stand.* **63A**, 55-62, 1959
55. Lawson, A.W., Tang, T-Y., *Phys. Rev.* **76**, 301 (1949)
56. R. A. Forman, G. J. Piermarini, J. D. Barnett, and S. Block, Pressure Measurement Made by the Utilization of Ruby Sharp-Line Luminescence, *Science* **176**, 284-285, 1972. 54b. A. Dadashev, M. P. Pasternak, G. K. Rozenberg, R. D. Taylor, *Rev. Sci. Instrum.*, **77**, 2633, (2001)
57. Diamonds and Diamond Grading, course material - Book 11, Grading Clarity, Gemological Institute of America, 2002
58. easyLab Technologies Ltd. - http://www.easylab.co.uk/
59. LeToullec, R., Pinceaux, J.P., Loubeyre, P. (1988). The membrane diamond anvil cell: a new device for generating continuous high pressure variations. *High Press. Res.*, **1**, 77-90.
60. Adams, D.M. and Sharma, S.K., Selection of diamonds for infrared and Raman spectroscopy. Journal of Physics E: Scientific Instruments, 1977. 10(7): p. 680-682.
61. Dunstan, D.J. and Spain, I.L., The technology of diamond anvil high-pressure cells: II. Operation and use. J. Phys. E: Sci. Instrum., 1989. 22: p. 923-933.
62. Soignard, E. and McMillan, P.F., An introduction to diamond anvil cells and loading techniques, in NATO Science Series, A. Katrusiak and P. McMillan, Editors. 2003, Kluwer Academic Publishers: Dordrecht/Boston/London.
63. Bassett, W.A. and Takakashi, T., Silver iodide polymorphs. The American Mineralogist, 1965. 50: p. 1576.
64. Hull, S. and Keen, D.A., Pressure-induced phase transitions in AgCl, AgBr and AgI. Physical Review B, 1999. 59(2).
65. Sahu, P.C., Thomaskutty, K.V., Shekar, N.V.C., Yousuf, M., and Rajan, K.G., Simple device for drilling holes in metal gaskets for diamond anvil cell experiments. Review of Scientific Instruments, 1993. 64(10): p. 3030-3031.
66. Lorenzana, H.E., Bennahmias, M., Radousky, H., and Kruger, M.B., Producing diamond anvil cell gaskets for ultrahigh-pressure applications using an inexpensive electric discharge machine. Review of Scientific Instruments, 1994. 65(11): p. 3540-3543.
67. Lorenzana, H.E., Bennahmias, M., Radousky, H., and Kruger, M.B., Producing diamond anvil cell gaskets for ultrahigh-pressure applications using an inexpensive electric discharge machine. Review of Scientific Instruments, 1994. 65(11): p. 3540-3543.
68. Pugh, E., Thompson, H.E., Balsod, R.B., and Brown, S.V., Automatic spark drill for high pressure experiments. Review of Scientific Instruments, 2006. 77.
69. Jayaraman, A., Diamond anvil cell and high-pressure physical investigations. Reviews of Modern Physics, 1983. 55(1): p. 65.
70. R. A. Forman, G. J. Piermarini, J. Dean Barnett, S. Block, Science, ***176***, 284 (1972)
71. H. K. Mao, P. M. Bell, Science, ***191***, 851 (1976)

72. H. K. Mao, J. Xu, P. M. Bell, J. Geophys. Res., ***91***, 4673 (1986)
73. Emerets, M. *High Pressure experimental Methods*, Oxford University Press, **1996.**
74. X-ray diffraction – A Practical Approach, Suryanarayana, C., Grant Norton, M., *Plenum Press*, **1998**.
75. G. N. Greaves, C. R. A. Catlow, G. E. Derbyshire, M. I. McMahon, R. J. Nelmes, G. van der Laan, *Nature Materials*, **7**, 827 - 830 (2008)
76. Lennie, A.R., Laundy, D., Roberts, M.A., and Bushnell-Wye, G., A novel facility using a Laue focusing monochromator for high-pressure diffraction at the SRS, Daresbury, UK. Journal of Synchrotron Radiation, 2007. 14: p. 433-438.
77. A. P. Hammersley, S. O. Svensson, M. Hanfland, A. N. Fitch, D. Häusermann, High Pressure Res., ***14***, 235 (1996)
78. C. V. Raman, K. S. Krishnan, *Nature* **121,** 501 (1928)
79. G. Landsberg, L. Mandelstam, *Naturwissenschaften*, **16,** 577 (1928)
80. P. F. McMillan, *Reviews in Mineralogy – Microscopic to Macroscopic*, Vol. 14, Ed S. W. Kieffer, A. Navrotsky, **1985**, 18
81. H. A. Szymanski, *Raman Spectroscopy – Theory and Practice*, **1967**, Plenium Press, p. 2
82. G. R. Loppnow, L. Shoute, K. J. Schmidt, et al., Philosophical Transactions of the Royal Society London A **362**, 2461 (2004).
83. V. I. Merkulov, J. S. Lannin, C. H. Munro, S. A. Asher, V. S. Veerasamy, W. I. Milne, Physical Review Letters **78**, 4869 (1997).
84. A. C. Ferrari and J. Robertson, Physical Review B **61**, 14095 (2000).
85. A. C. Ferrari and J. Robertson, Physical Review B **64**, 075414 (2001).
86. A. C. Ferrari and J. Robertson, Philosophical Transactions of the Royal Society London A **362**, 2477 (2004).
87. A. C. Ferrari, S. E. Rodil, and J. Robertson, Diamond and Related Materials **12**, 905 (2003).
88. A. C. Ferrari, S. E. Rodil, and J. Robertson, Physical Review B **67**, 155306 (2003).
89. D.F. Shriver, P.W. Atkins *Inorganic Chemistry,* 3rd Ed. pp.451
90. H. Montiguad, B. Tanguy, G. Demazeau, S. Courjault, M. Birot, J. Dunogues, *C. R. Acad. Sci., Ser. IIb* **1997**, 325, 229
91. M. Deifallah, V. Lees, P. F. McMillan, F. Cora, Physical Review B **in revision** (2008).
92. Katritzky, A. R., Ambler, A. P., *Physical Methods in Heterocyclic Chemistry,* Katritzky, A. R., Ed., Academic Press; New York and London, 1963; Vol II, p161
93. Marchewka, M. K., Materials Science and Engineering B **95** (2002) 214-221
94. Larkin, P. J., M. P. Makowski and N. B. Colthup 1999. The form of the normal modes of s-triazine: infrared and Raman spectral analysis and ab initio force field calculations. Spectrochimica Acta A, 55, 1011-1020
95. Wang, Y-L, A. M. Mebel, C-J Wu, Y-T Chen, C-E Lin and J-C Jiang 1997. IR spectroscopy and theoretical vibrational calculation of the melamine molecule. J. Chem. Soc. Faraday Trans. 93, 3445-345
96. Soignard, E., High pressure - high temperature synthesis and studies of nitride materials,in Chemistry. 2003, University College of London: London. p. 176.

97. R. Livneh, T. L. Haslett, and M. Moskovits, Physical Review B **66**, 195110 (2002).
98. C. Y. Panicker, H. T. Varghese, A. John, et al., Spectrochimica Acta A **58**, 1545 (2002).
99. H. Imanaka, B. N. Khare, J. E. Elsila, E. L. O. Bakes, C. P. McKay, D.P. Cruikshank, S. Sugita, T. Matsui, R. N. Zare, *Icarus* **168**, 344 (2004).
100. D. Lin-Vien, N. B. Colthup, W. G. Fateley, et al., *The Handbook of Infrared and Raman Characteristic Frequencies of Organic Molecules* (Academic Press, San Diego, 1991)
101. S. Liu, S. Gangopadhyay, G. Sreenivas, et al., Physical Review B **55**, 13020 (1997).
102. N. Mutsukura and K.-I. Akita, Thin Solid Films **349**, 115 (1999)
103. P. J. Larkin, M. P. Makowski, and N. B. Colthup, Spectrochimica Acta A **55**, 1011 (1999).
104. E. Duval, A. Mermet, and L. Saviot, Physical Review B **75**, 024201 (2007).
105. M. Hass, Solid State Communications **7**, 1069 (1969).
106. P. F. McMillan and B. Piriou, Journal of Non-Crystalline Solids **53**, 279 (1982).
107. R. Shuker and R. W. Gammon, Physical Review Letters **25**, 222 (1970).
108. Coll, P., Coscia, D., Gazeau, M-C, Guez, L., & Raulin, F. 1998 Origin of life and evolution of the biosphere, 28, 195-213
109. Mutsukura, N., & Akita, K-I. 1999 Thin Solid Films, 349, 115-119
110. M. Deifallah, P. F. McMillan and F. Corà, *J. Phys. Chem*. C. **112**, 5447 (2008).